Thermoelectric Materials: Ternary and Higher Oxides and Tellurides

by

Yanjie Cui

A thesis

presented to the University of Waterloo

in fulfillment of the

thesis requirement for the degree of

Doctor of Philosophy

in

Chemistry

Waterloo Ontario Canada 2009

Author's Declaration

I hereby declare that I am the sole author of this thesis. This is a true copy of the thesis, including any required final revisions, as accepted by my examiners.

I understand that my thesis may be made electronically available to the public.

Abstract

Thermoelectric power generators can convert a temperature gradient into electrical energy, serving as a new energy resource by utilizing solar energy or by utilizing more waste heat. Thermoelectric coolers have the advantage of no moving parts, are quiet and release no gases that are harmful to the atmosphere, in contrast to compression-based refrigeration.

While the low efficiency of "classical" thermoelectric devices limits their wide applications, the exploration of better thermoelectric materials is of great importance to improve the efficiency of thermoelectric devices. Good thermoelectric materials are usually narrow band gap semiconductors with a large Seebeck coefficient, reasonably high electrical conductivity and low thermal conductivity. This thesis deals with the exploration of new thermoelectric materials based on transition metal tellurides and the optimization of bulk materials based on oxides of low toxicity and high stability in air.

In the first project, seven new ternary or quaternary tellurides, crystallizing in three different structure types, were synthesized and characterized. Single crystal X-ray diffraction was used for crystal structure determination; powder X-ray diffraction and energy dispersive X-ray analysis (EDAX) were used for phase and composition analyses. Physical properties of these compounds were predicted by electronic structure calculations and confirmed by physical property measurements.

The ternary tellurides $Ba_7Au_2Te_{14}$ and $Ba_{6.76}Cu_{2.42}Te_{14}$ form ternary variants of the $NaBa_6Cu_3Te_{14}$ type, space group $P6_3/mcm$, with a = 14.2593(7) Å, c = 9.2726(8) Å, V = 1632.8(2) Å^3 (Z = 2) for $Ba_7Au_2Te_{14}$, and a = 14.1332(4) Å, c = 9.2108(6) Å, V =

1593.3(1) Å^3 (Z = 2) for $Ba_{6.76}Cu_{2.42}Te_{14}$. The Na site of the aristotype is filled with a Ba atom (deficient in case of the Cu telluride), and the Cu site with 66.5(3) % Au and 61.7(8) % Cu, respectively. An additional site is filled with 9.5(7) % Cu in the structure of $Ba_{6.76}Cu_{2.42}Te_{14}$. These structures are comprised of bent Te_3^{2-} units, and $AuTe_4$/$CuTe_4$ tetrahedra forming channels filled with Ba cations. $BaTe_9$ polyhedra are connecting the channels to a three-dimensional structure. According to the formulations $(Ba^{2+})_7(Au^+)_2(Te_3^{2-})_3(Te^{2-})_5$ and $(Ba^{2+})_{6.76}(Cu^+)_{2.42}(Te_3^{2-})_3(Te^{2-})_5$, the materials are electron-precise with 16 positive charges equalizing the 16 negative charges. LMTO calculation revealed band gaps of 0.7 eV and 1.0 eV, respectively.

Five quaternary tellurides, $Ba_4M_{4-x}A_2Te_9$ (M = Cu, Ag or Au and A = Si or Ge), were prepared in evacuated silica tubes at 750 °C. Three of them crystallize in space group *Pbam*, with lattice parameters of a = 8.6835(3) Å, b = 13.6421(4) Å, c = 10.2612(3) Å, V = 1215.55(7) Å^3 (Z = 2) for $Ba_4Ag_{3.95}Ge_2Te_9$, a = 8.6389(3) Å, b = 13.5883(4) Å, c = 10.2252(3) Å, V = 1200.32(7) Å^3 (Z = 2) for $Ba_4Ag_{3.97}Si_2Te_9$, and a = 8.6464(2) Å, b = 13.5305(4) Å, c = 10.0810(3) Å, V = 1179.38(6) Å^3 (Z = 2) for $Ba_4Cu_{3.71}Ge_2Te_9$. Two other compounds crystallize in a super cell thereof, space group *Pnma*, with lattice parameters of a = 13.5808(6) Å, b = 20.7033(9) Å, c = 8.6418(4) Å, V = 2429.8(2) Å^3 (Z = 4) for $Ba_4Au_{3.69}Ge_2Te_9$, and a = 13.4294(4) Å, b = 20.0980(7) Å, c = 8.5699(3) Å, V = 2313.0(1) Å^3 (Z = 4) for $Ba_4Cu_{3.76}Si_2Te_9$. All these structures are composed of Ag_4/Cu_4/Au_4 clusters and dimeric A_2Te_6 units, which are interconnected through Te atoms into a three-dimensional structure. The covalent M-Te/A-Te network surrounds a one-dimensional linear channel running along the c or b direction,

encompassing the Ba atoms. Electronic structure calculations and transport property measurements show that these compounds are *p*-type semiconductors with calculated band gaps of 1.0 eV for the copper germanium compound, 0.89 eV for the copper silicon compound, 0.24 eV for the silver germanium compound, 0.35 eV for the silver silicon compound, and 0.19 eV for gold germanium compound,.

In the second project, two series of *n*-type doped perovskite $SrTiO_3$ were prepared in a high temperature tube furnace under dynamic high vacuum of the order of 10^{-6} mbar, namely $SrTi_{1-x}(Nb,Ta)_xO_3$, and $Sr_{1-x}La_xTi_{1-x}(Nb,Ta)_xO_3$. The phase purity was characterized by means of powder X-ray diffraction and electron probe micro analysis (EPMA). Rietveld refinements were performed to check for purity and symmetry reduction. Electronic structure calculations indicate *n*-type conduction with steep and flat bands in the vicinity of the Fermi level for x = 0.125. The physical properties, such as Seebeck coefficient, electrical conductivity, and thermal conductivity, were measured at high temperatures for all the samples, in collaboration with scientists from Clemson University, Oak Ridge National Laboratory, and General Motors R & D Center.

Of the series of Nb/Ta-doped strontium titanates $SrTi_{1-x}(Nb,Ta)_xO_3$, $SrTi_{0.90}Ta_{0.10}O_3$ exhibits the highest *ZT* value, namely 0.17 for at 752 K. Of the double substituted series, $Sr_{0.99}La_{0.01}Ti_{0.99}Ta_{0.01}O_3$ was best with *ZT* = 0.13 at 660 K. The rapid increases imply that higher *ZT* values are likely to occur at higher temperatures.

Acknowledgements

First I would like to express my profound gratitude to my supervisor Prof. H. Kleinke for his invaluable guidance, advice and support. His truly scientific intuition, knowledge, passion and patience guided me through a lot of difficulties, and also inspired me to keep on working towards my dream becoming a real researcher like him.

Many thanks go in particular to our previous postdoctoral fellow and current department crystallographer, Dr. A. Assoud, who provided a lot of valuable advices, and help from the very early stages of this research. I also want to thank our past crystallographer, the late Dr. N. J. Taylor, who was the instructor of my first course X-Ray Crystallography. His kindness and knowledgable will be memorized forever.

It is my great pleasure to have worked with these wonderful colleagues. Many thanks go to Shahab, Navid, Jackie, Katja, Raj, Mayasree, Hong, Bryan, Savitree, Tingting, Christian, Mariya, Michael, and Wiqar. Especially Katja, I want to express my deepest appreciation for all her encouragement, understanding and friendship.

I really appreciate my advisory committee members, Prof. R. T. Oakley, Prof. L. F. Nazar, and Prof. K. Preuss for their comments and valuable suggestions during the course of my research. I am also grateful to my examiners, Prof. Mario Bieringer and Prof. Robert W. Hill.

I would like to extend my appreciation to all of our collaborators. First, Dr. Amow, thanks a lot for her valuable comments and discussions. As well, thanks to Dr. Salvador, Dr. Yang, Dr. Wang, and Dr. He, for their contributions and assistance.

I owe special gratitude to my great husband, Jian, whose love, support, and considerateness enabled me to complete my studies and made it an unforgettable time. I would like to thank my parents for all their love, understanding and support throughout my life. I am also grateful for all the friends for their friendship and encouragement which make my life more cheerful and memorable.

Dedication

Dedicated to Jian and Henry.

Table of Contents

List of Figures

List of Tables

Chapter 1 Introduction

With the expeditious development of the economy and society, the consumption of fossil fuel is reaching far beyond its availability. Therefore, the exploration of new energy sources and energy efficient materials is attracting more and more interest. Thermoelectric (TE) materials provide one solution that could serve as an alternative energy source by utilizing solar energy, or by using waste heat to produce electricity through TE generators. TE materials can also be used in the solid-state Peltier cooler to replace the compression-based refrigeration, which has the tendency to release gases that are harmful to the atmosphere. Currently, the low efficiency of "classical" TE devices limits their wide application. To explore new TE materials and to improve the TE performances of known materials are the major directions that researchers are working on.

1.1 Discovery of thermoelectric phenomena and their application

Thermoelectric phenomena generally refer to three separately identified effects: the Seebeck effect, the Peltier effect and the Thomson effect. The Seebeck effect describes the conversion of temperature gradients directly into electric voltage; the Peltier effect describes the generation of a temperature gradient by electric current, and is the reverse of the Seebeck effect. Finally, the Thomson effect describes the heat releasing or

absorption of a homogeneous current-carrying conductor which is subject to a temperature gradient.

1.1.1 **Seebeck effect**

In 1821, Thomas John Seebeck (1770-1831) discovered the existence of a magnetic field around a closed loop formed by two dissimilar metal conductors with a temperature difference between the junctions,[1] however, he did not immediately understand the electrical nature of this phenomenon. It was Hans Christian Ørsted (1771-1851), who first named this phenomenon "the thermoelectric effect" based on Seebeck's research, since he had already experimentally proved in 1820 that an electrical current can create a magnetic field. To honor the finding of Seebeck, this thermoelectric effect was named Seebeck effect. Seebeck had also observed that the magnitude of the magnetic field was proportional to the temperature difference and dependent on the type of conducting material, but did not depend on the temperature distribution along the conductors. This meant that the produced voltage difference (ΔV) was directly proportional to the temperature difference between the hot side and the cold side ($\Delta T = T_H - T_C$):

$$S = \frac{\Delta V}{\Delta T} \tag{1-1}$$

The proportionality is called the Seebeck coefficient (S), which is also known as thermopower. Figure 1.1. illustrates the generation of this effect, where an applied temperature difference causes charge carriers in a thermoelectric material to diffuse from the hot side to the cold side. Charge carriers at the hot end, such as electrons, gain higher kinetic energy and move relatively faster in the material. They accumulate at the cold

side and the oppositely charged nuclei are left behind at the hot side, as shown in Figure 1.1.. This charge separation results in a potential difference between the junctions, hence an electrical current flows when the two sides are connected. This current will be maintained as long as the temperature gradient exists.

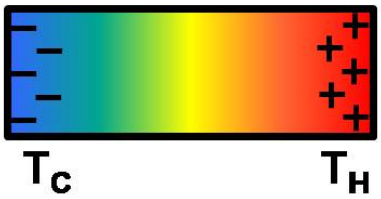

Figure 1.1. The electrical potential induced by the temperature gradient. (In this schematic the charge carriers are electrons.)

1.1.2 **Peltier effect**

In 1834, Jean Charles Athanase Peltier (1785-1845) noticed a temperature difference between the junctions of a circuit formed with two dissimilar conductors, when an electrical current passed through them.[2] Peltier did not realize the correlation between this phenomenon and the Seebeck effect. In 1838, Emil Lenz (1804-1865) showed that there was heat absorption or generation at the junctions of the two different conductors depending on the direction of the current. The ratio of heat flow rate (Q) to the current (I) for a particular material is known as the Peltier coefficient (Π):

$$\Pi = \frac{Q}{I} \tag{1-2}$$

The Peltier coefficient of a specific material expresses the amount of heat current carried by a unit charge.

1.1.3 **Thomson effect**

In 1851, William Thomson (1824-1907, later Lord Kelvin) observed that heat was absorbed or released in a homogeneous current-carrying conductor, resulting in the presence of a temperature gradient.[3] The heat production or absorption from this phenomenon is given by:

$$q = J^2\sigma^{-1} - \tau J\frac{dT}{dX} \quad \textbf{(1-3)}$$

Where σ is the conductivity, J is the current density, τ is the Thomson coefficient and dT/dX is the temperature gradient along the sample. In contrast to the Seebeck and Peltier coefficients, the determination of the Thomson coefficient involves only a single homogeneous conductor, hence τ can be determined independently for any conductor. In 1854, Thomson established two relationships between the coefficients, which are now known as the Thomson or Kelvin relationships. The first Kelvin relationship shows that the Thomson coefficient can be obtained through the Seebeck coefficient:

$$\tau = T\frac{dS}{dT} \quad \textbf{(1-4)}$$

The Seebeck and the Peltier effects are related by the second Kelvin relationship:

$$\Pi = TS \quad \textbf{(1-5)}$$

1.1.4 **Application of thermoelectric devices**

In 1885, Rayleigh considered the possibility of using the thermoelectric effect for power generation.[4] It was in the 1950s that Ioffe and his colleagues developed the thermoelectric conversion theory, which provided the basis for modern thermoelectric theory and led to the prospering of thermoelectric applications.[5] Since then, thermoelectric devices have been well investigated.

To convert thermal energy (like waste-heat) into electricity, the Seebeck effect is utilized, as shown in Figure 1.2.a Heat is being pumped from the hot *p-n* junction and rejected from the cold junction, thus producing an electrical current, which amounts to power generation. Conversely, the Peltier effect is utilized for solid-state refrigeration (Figure 1.2.b). If an electric current is applied to the *p-n* junction as shown, heat is pumped from the cold junction to the hot junction. A typical thermoelectric module consists of many pairs of p-type and n-type semiconducting thermoelements forming thermocouples, which are connected electrically in series and thermally in parallel.

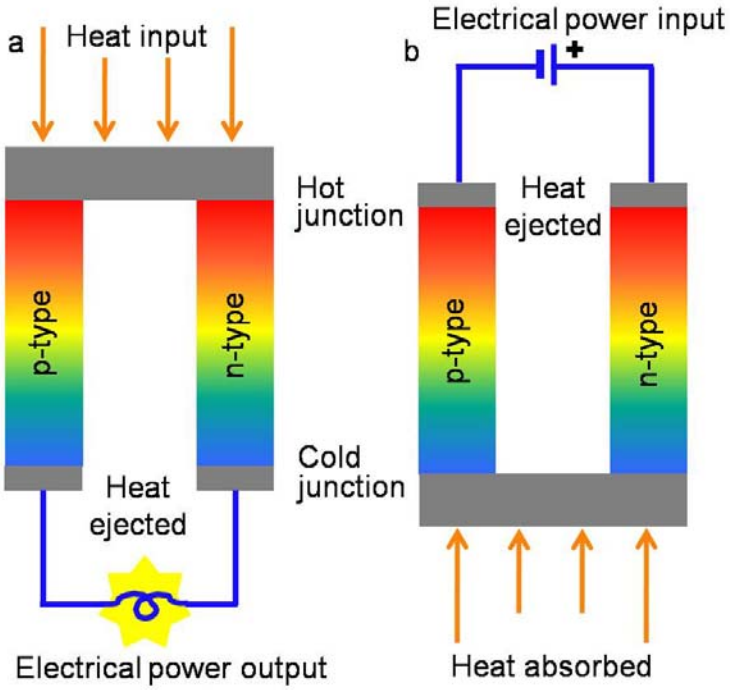

Figure 1.2. a. Power generator module; b. Refrigerator module.

Recently, there has been a rapid increase in the use of thermoelectric devices for power generation in remote telecommunication sites, space probes, and waste heat recovery for automobiles, portable refrigerators, electronic component coolers, and metal alloy sorting devices. Some examples are shown in Figure 1.3.

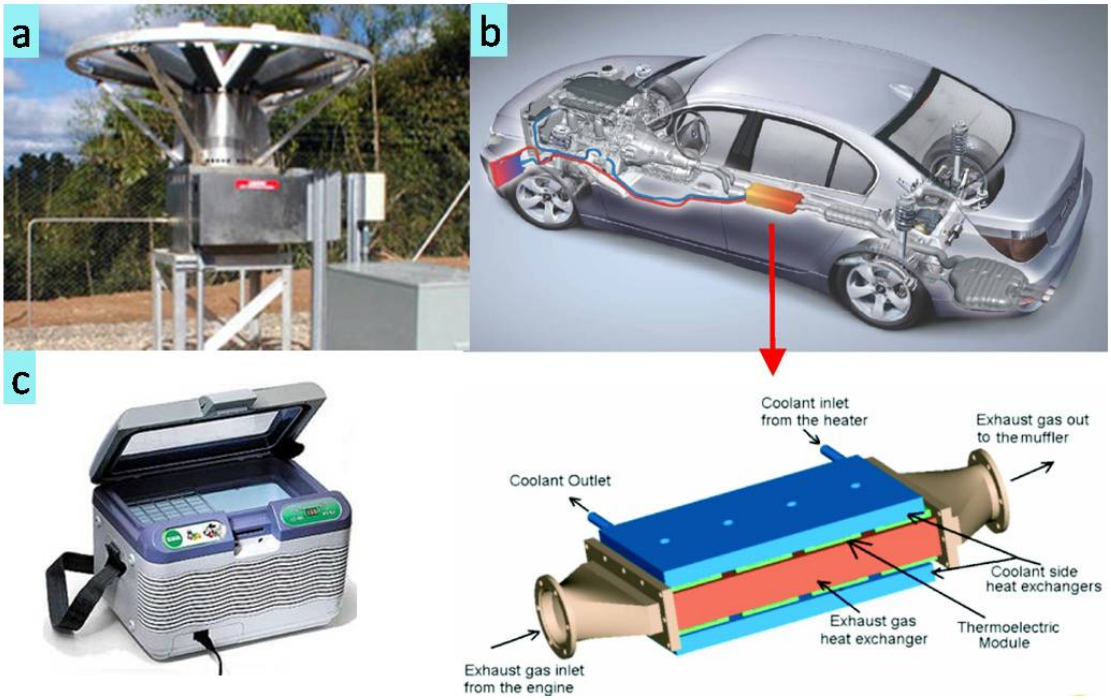

Figure 1.3. a. Global TEG on a natural gas line,[6] b. BMW TEG in the car exhaust system, c. Lunch box with TE technologies.[7]

Thermoelectric devices have many advantages compared with conventional cooling systems, such as high reliability, no moving parts, efficiency independent of size, no maintenance, acoustically silent, electrically "quiet", and environmentally friendly. However, thermoelectric devices have not been widely used in commercial applications because of their low efficiency.

1.2 Thermoelectric efficiency

The energy conversion efficiency (η) in thermoelectric power generation and the coefficient of performance (ϕ) in thermoelectric refrigeration devices are directly related to the dimensionless figure of merit of the thermocouple zT, as shown in the following equations. The efficiency of power generation is the ratio of the electrical power output

(W) over the thermal power supplied (Q_H), and the coefficient of performance corresponds to the ratio of cooling rate (Q_C) over the power supplied (W).[4, 8]

$$\eta = \frac{W}{Q_H} = \frac{T_H - T_C}{T_H} \times \frac{\sqrt{1+zT}-1}{\sqrt{1+zT}+\frac{T_C}{T_H}} \tag{1-6}$$

$$\phi = \frac{Q_C}{W} = (\frac{T}{T_H - T_C} \times \frac{\sqrt{1+zT}-1}{\sqrt{1+zT}+1}) - \frac{1}{2} \tag{1-7}$$

For both equations, T is the mean temperature of the hot-side temperature (T_H) and the cold-side temperature (T_C). A higher zT value will result in a higher efficiency, and when zT reaches infinity, the efficiency reaches that of an ideal thermodynamic machine. It is important to note that the thermocouple's figure of merit, z, is a function of the properties of both materials that form the thermocouple. For practical reasons, researchers attempting to find a good thermoelectric material (either p-type or n-type) define a figure of merit, Z, for a single material:

$$ZT = T\frac{S^2\sigma}{\kappa} \tag{1-8}$$

Where T is the mean temperature, S is the thermopower or Seebeck coefficient, σ is the electrical conductivity and κ is the total thermal conductivity. The material's figure of merit, Z, can only be accurately related to the true figure of merit, z, in special cases. Such as the p-type and n-type materials have exactly the same S, σ, and κ absolute values, or κ/σ of one type material is negligibly small compared with that of the other material, and the latter case is of more practical importance.[4] If any of these are true and temperature is assumed to be independent, then the maximum device efficiency is given by the above equation with $z = Z$.

It should be pointed out that the common practice of simply taking the averaged Z values of the two branches as the figure of merit of a thermocouple can lead to substantial errors. However, the quotation of the figure of merit to characterize the thermoelectric performance for a single material is obviously of conceptual value. Moreover, it seems that there is currently no better parameter for comparison in the thermoelectric material research. Since our objective is to investigate high efficiency thermoelectric materials, we will continue to use these concepts routinely applied in the literature to discuss how to optimize ZT values for a single material.

As shown in equation (1-8), we can easily conclude that high ZT values are achieved with a high Seebeck value and high electrical conductivity, but low thermal conductivity. Unfortunately, these thermoelectric parameters cannot be treated independently and the correlations between them are rather complicated.

Figure 1.4. shows the dependence of the Seebeck coefficient, the electrical conductivity, the thermal conductivity, and the material figure of merit on the charge carrier concentration.[8] Low carrier concentration materials like insulators are usually not considered proper materials for these applications due to their extremely low electrical conductivity, in spite of their high Seebeck coefficient. High carrier concentration materials like metals, usually with low Seebeck values and large thermal conductivities, are also regarded as unsuitable thermoelectric material candidates. Hence, only heavily doped semiconductors fall into the appropriate thermoelectric material category.

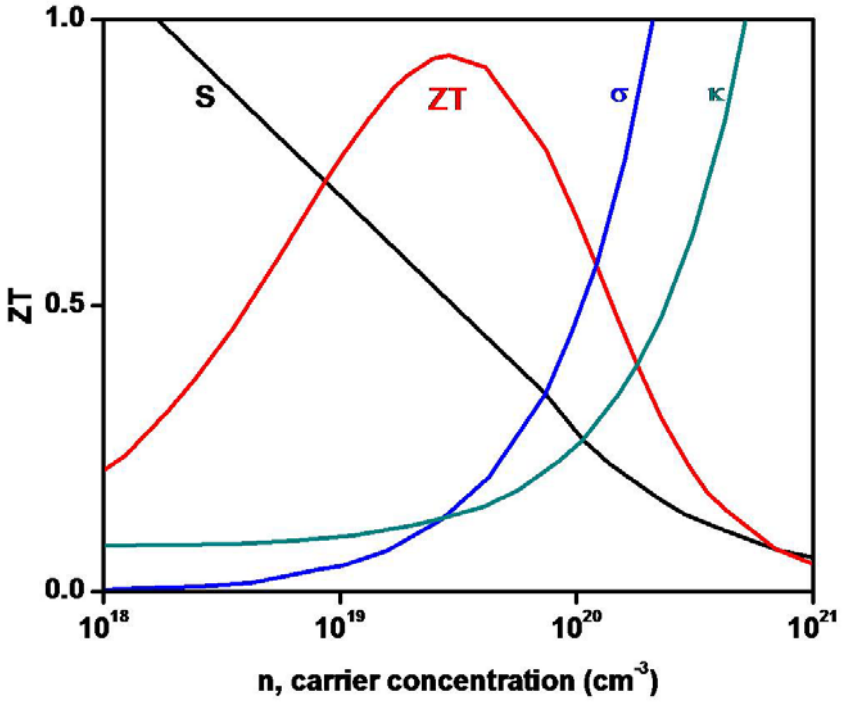

Figure 1.4. Dependence of *S*, σ, κ, and *ZT* on charge carrier concentration.

1.2.1 **Electrical conductivity**

The existence of a potential difference along a conducting material will force the charge carriers to move, creating an electrical current. The electrical conductivity (σ) is a measurement of a material's ability to accommodate the movement of an electric charge. For any conductive material, σ is determined by the charge carrier concentration (*n)*, the charge of the carrier (*e* for an electron which is 1.602×10^{-19} C), and the carrier mobility (μ):[9]

$$\sigma = ne\mu \qquad \textbf{(1-9)}$$

In metals, *n* is a constant since all the valence electrons are free to move at all temperatures, therefore, the temperature dependence of μ solely determines the temperature dependence of conductivity. The carrier mobility is a function of the carrier

scattering time (τ), the effective mass (m^*) in the direction of the current (I), and the carrier charge:

$$\mu = \frac{e\tau}{m^*} \quad \textbf{(1-10)}$$

The carrier scattering time is the time that the charge carrier takes to lose momentum. Materials containing elements with similar electronegativity are more likely to have longer scattering times, resulting in higher electrical conductivity.[10] Materials containing heavier scatterers and large m^* values, usually exhibit small mobility, which in turn leads to low electrical conductivity. The exact relation between effective mass and mobility is complex, and depends on electronic structure, scattering mechanisms and anisotropy. It will not be discussed here in detail, but generally the conductivity of metal will decrease with increasing temperature due to the decreasing mobility.

In semiconductors, however, *n,* may also change with temperature, and this change usually dominates the temperature dependence of electrical conductivity.[9] With the increasing temperature, the charge carrier concentration will first increase then remain constant and increase again for extrinsic semiconductors, while the charge carrier concentration will keep increasing exponentially for intrinsic semiconductors due to the thermal activation. Therefore, electrical conductivity will increase with an increasing temperature due to the increase in the charge carriers.

1.2.2 **Seebeck coefficient**

As shown in Figure 1.4., the low carrier concentration insulators or semiconductors have large Seebeck coefficients. The relation between carrier

concentration and the Seebeck coefficient for metals and degenerate semiconductors (parabolic bond, energy-independent scattering approximation[11]) is given by:[8]

$$S = \frac{8\pi^2 k_B^2}{3eh^2} m^* T \left(\frac{\pi}{3n} \right)^{2/3} \quad \textbf{(1-11)}$$

Where n is the charge carrier concentration, k_B is the Boltzmann constant and m^* is the effective mass of the carrier. From equation (1-11), it is concluded that a low carrier concentration gives a large Seebeck coefficient, while equation (1-9) shows that low carrier concentration also results in low electrical conductivity. Generally, the maximum ZT value occurs at carrier concentrations between 10^{19} and 10^{21} carriers per cm^3, which is a typical concentration found in heavily doped semiconductors.

1.2.3 **Thermal conductivity**

Thermal conductivity (κ) is the property of a material that reflects its ability to conduct heat, and contains two parts: the electronic part (κ_e), and the phonon part (or lattice vibrations, κ_{ph}). Near room temperature and above, κ_e and κ_{ph} contribute to κ independently, as shown in the following equation:[12]

$$\kappa = \kappa_e + \kappa_{ph} \quad \textbf{(1-12)}$$

In metals, the electronic term dominates and is responsible for the high thermal conductivity. It is directly related to the electrical conductivity at a given temperature according to the Wiedemann-Franz relation:[13]

$$\kappa_e = L\sigma T \quad \textbf{(1-13)}$$

Where L is the Lorenz factor, which is $2.45 \times 10^{-8}\ W\Omega K^{-2}$ for a free electron. The Lorenz factor can vary with carrier concentration, especially in low carrier concentration

materials where it can be reduced up to 20 % from the free electron value. In insulators and low carrier concentration semiconductors, κ_{ph} is usually much larger than κ_e.

Based on the Wiedemann-Franz law, the material figure of merit can be rewritten as:

$$ZT = \frac{S^2}{L \cdot (1 + \frac{\kappa_{ph}}{\kappa_e})} \quad \textbf{(1-14)}$$

This formula clearly shows that materials with a large S, a large κ_e and a low κ_{ph} are favorable to achieve high ZT values. In metals, the Seebeck coefficient is usually very small, though $\kappa_e >> \kappa_{ph}$. On the other hand, insulators and low carrier concentration semiconductors have large Seebeck values, while they are typically in the region where $\kappa_{ph} > \kappa_e$. The solution for a high ZT material is to find semiconductors with very low κ_{ph}.[12] Efforts have recently been made to find better thermoelectric materials by minimizing κ_{ph} without causing too much reduction of σ.[14]

There are several approaches to reducing phonon thermal conductivity. One approach is to synthesize compounds composed of heavy elements, for the atomic vibration frequencies are reduced by high atomic masses which in turn leads to a lowered thermal conductivity.[15] This is one of the reasons why heavy elements like antimony, bismuth, tellurium, and lead are often used in current thermoelectric research. The other proven way to reduce phonon thermal conductivity is by using solid solution.[16] This method is employed in commercial state-of-the-art thermoelectric cooling materials, wherein a solid solution of binary tellurides Bi_2Te_3 with Sb_2Te_3 forms the *p*-type leg and a solid solution of Bi_2Te_3 with Bi_2Se_3 forms the *n*-type leg in the module.

Another method used to reduce phonon thermal conductivity is based on the prominent concept of "phonon glass-electron crystal" (PGEC), which was proposed by Slack in 1995.[17] PGEC materials are compounds with glass-like thermal conductivity and crystalline-like electrical properties. These materials can be prepared by including loosely bonded heavy atoms in large pockets or cages in a crystalline compound. These heavy atoms can rattle in the pockets or cages to reduce the thermal conductivity and ideally retain the electronic properties of the original compound. The investigations of skutterudites[18] and clathrates[19] are based on this concept.

1.3 Developments of thermoelectric materials

By the 1950s, with thermoelectric applications booming, the field of thermoelectric materials experienced a rapid development and the thermoelectric material Bi_2Te_3 became commercialized.[20] During the following three decades (1960-1990) the only significant development was the alloying of Bi_2Te_3 with Sb_2Te_3 or Bi_2Se_3. In the early 1990s, the development of advanced thermoelectric materials reactivated the interest of researchers. With this renewed interests, two main categories of thermoelectric material research advanced rapidly: bulk thermoelectric materials and low-dimensional material systems. Along with the classical area of thermoelectric material research, a new type of material, complex oxides, became a potential candidate for thermoelectric application. Complex oxides had long been considered inappropriate for thermoelectric applications due to their strong ionic character, causing poor mobility of the charge carriers. Since 1997, however, oxides have become a new branch of thermoelectric research. This began with the discovery of an unexpected high thermoelectric performance of a single crystal of layered cobalt oxide ($NaCo_2O_4$).[21]

1.3.1 **Bulk materials**

The investigation into promising bulk thermoelectric materials has remained active for the last two decades. There are several material systems that attract the most attention due to their potential to achieve high thermoelectric figures of merit. The bulk thermoelectric materials of primary interest include: binary semiconductors like Bi_2Te_3, and PbTe; complex chalcogenides such as $CsBi_4Te_6$,[22] Tl_9BiTe_6,[23] Tl_2SnTe_5[24] and $Ag_nPb_mM_nTe_{m+2n}$ (M = Sb, Bi);[25] rattler compounds such as skutterudites[18, 26] and clathrates[19, 27]; as well as intermetallic, β-Zn_4Sb_3,[28] and Half-Heusler[29] phases.[30] The *ZT*-*T* values for some of these examples are listed in Figure 1.5.,[31] and some of their structures are discussed in the following section.

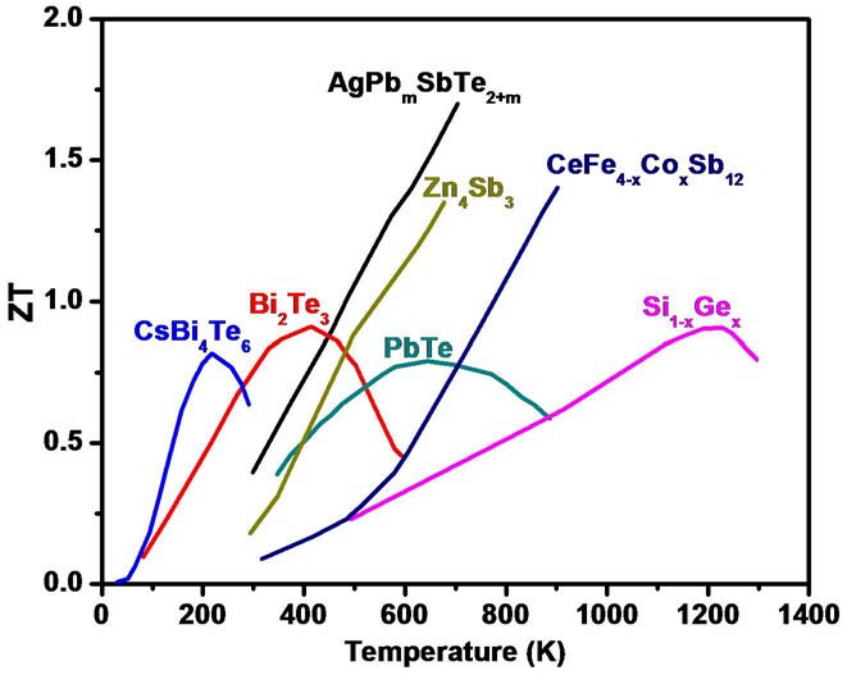

Figure 1.5. Figure of merit *ZT* shown as a function of temperature for several bulk thermoelectric materials.

The classical bulk material Bi_2Te_3, used in state-of-the-art thermoelectric devices, crystallizes in a layered structure (Figure 1.6.) with rhombohedral symmetry ($R\bar{3}m$) and cell parameters of a = 3.8 Å and c = 30.5 Å at room temperature.

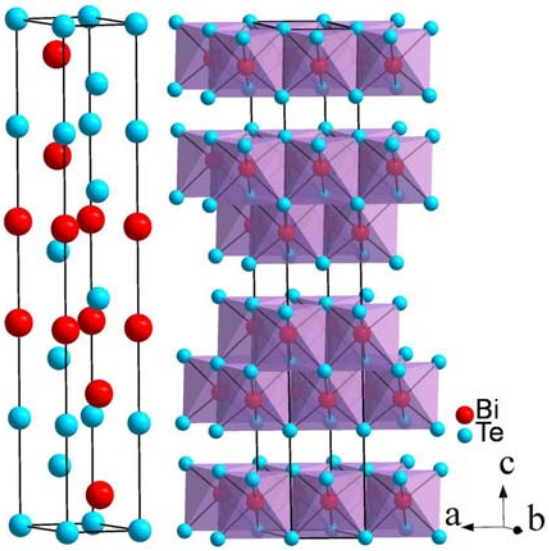

Figure 1.6. Crystal structure of the classical thermoelectric material, Bi_2Te_3.

The layered structure facilitates anisotropic thermal and electrical transport properties of Bi_2Te_3. The thermal conductivity in the plane perpendicular to the c-axis is 1.5 $Wm^{-1}K^{-1}$, which is almost twice that of the thermal conductivity across the plane along the c-axis direction (0.7 $Wm^{-1}K^{-1}$). As mentioned above, alloying could further reduce the lattice thermal conductivity of Bi_2Te_3 through the scattering of short-wavelength acoustic phonons. Currently, the optimal compositions for thermoelectric cooling devices are $Bi_2Te_{2.7}Se_{0.3}$ (n-type) and $Bi_{0.5}Sb_{1.5}Te_3$ (p-type) with $ZT \approx 1$ near room temperature.[31]

Based on Slack's PGEC concept, many rattler compounds have been investigated; for example, skutterudites and clathrates. These compounds are cage-like materials that have large empty cages or voids in which "rattler" atoms can be inserted to reduce the

phonon thermal conductivity. A schematic illustration of a skutterudite crystal is shown in Figure 1.7., where the rattler is inside a 12-coordinated "cage" (shown in light violet), surrounded by pnictogen atoms depicted in cyan. The metal sites are depicted in red.

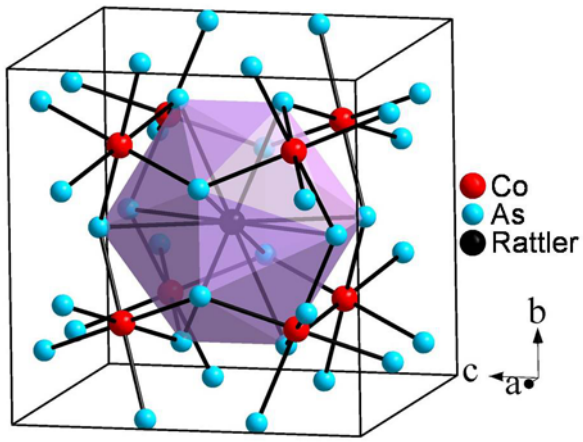

Figure 1.7. Schematic illustration of a skutterudite crystal.

Aside from the classical telluride Bi_2Te_3, heavy atom containing ternary or quaternary chalcogenides with low dimensional or isotropic complex structures are another focus of recent thermoelectric material research. This is due to the attractive properties for thermoelectric materials exhibited by most of these compounds, such as large effective carrier masses and low phonon thermal conductivity. $CsBi_4Te_6$ is one of the layered ternary tellurides with an anisotropic structure which shows the highest *ZT* values below room temperature (0.8 at 225 K) with appropriate doping. Figure 1.8. shows the anionic slabs $[Bi_4Te_6]^-$ alternating with Cs^+ layers.

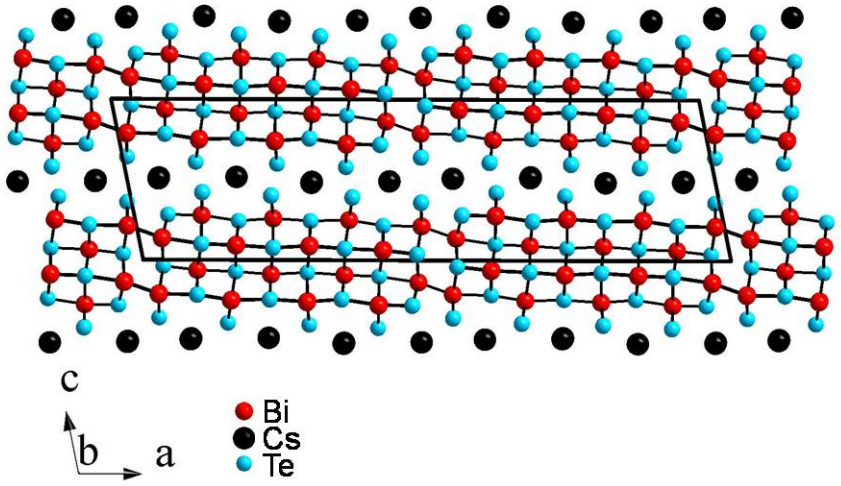

Figure 1.8. Layered crystal structure of $CsBi_4Te_6$.

In 2004, the Kanatzidis group reported a series of compounds with a complex formula $Ag_nPb_mM_nTe_{m+2n}$ (M = Sb, Bi), also known as LAST-m material, which crystallize in variants of the PbTe structure.[25] Properly doped LAST-m materials exhibit exceptionally high *ZT* values of 1.2 for LAST-10 to 1.7 for LAST-18, at 700 K. This is due to the very low total thermal conductivity, which according to the recent results, could be attributed to the nature of the microstructure of these materials at the nanoscopic level.[32]

1.3.2 **Low dimensional materials**

Two concepts have theoretically predicted and experimentally demonstrated that low-dimensional material research could enhance the properties of the original parent materials.[20] Firstly, the introduction of nanoscale constituents, like quantum dots, nanowires, and thin-film structures, would introduce quantum-confinement effects to enhance *S*, and to control *S* and σ somewhat independently.[20] Harman et al. reported the $PbTe/PbTe_{0.98}Se_{0.02}$ quantum dot superlattice (QDSL) structures, which were reported to

have *ZT* values around 1.3-1.6 at 300 K.[33]. The enhancement of *ZT* in this superlattice structure appears to come from an increase in power factor. The second concept emphasizes that the increased internal interfaces would scatter phonons more effectively than electrons, therefore, the thermal conductivity would be reduced more than the electrical conductivity, based on differences in their respective scattering lengths.[34] Researchers at the Research Triangle Institute (RTI) have demonstrated a significant enhancement in *ZT* through the construction of Bi_2Te_3/Sb_2Te_3 superlattices (SL), which exhibited a *ZT* of 2.4 at 330 K.[35] This improvement has demonstrated that the scattering of phonons by the interface reduces the thermal conductivity more than the electrical conductivity.[31]

1.3.3 **Complex oxides**

Oxides with strong ionic character were thought to be unsuitable for thermoelectric application due to their weak orbital overlap associated with low carrier mobility. This situation changed when $NaCo_2O_4$ was reported to exhibit an unexpectedly high *ZT* value of 0.8 at 1000 K, which is comparable to conventional thermoelectric materials. This compound exhibits a large Seebeck coefficient with rather low carrier mobility. After this discovery was made, the Co-based *p*-type layered oxides (such as Na_xCoO_2,[21] $Ca_3Co_4O_9$[36] and $Bi_2Sr_3Co_2O_y$[37, 38]) attracted the most interest in thermoelectric oxide research. Figure 1.10. shows the layered structure of the Co-based oxide Na_xCoO_2 with x = 0.5, in which the hexagonal CdI_2-type CoO_2 layer and the Na^+ layer alternately stack along the *c*-axis. In these oxides, the CoO_2 layers with a strongly correlated electron system facilitate the electronic transport to achieve high electrical

conductivity, while the Na^+ layer, or Ca_2CoO_3 and $Bi_2Sr_2O_4$ misfit layers serve as phonon scattering regions to attain low thermal conductivity.

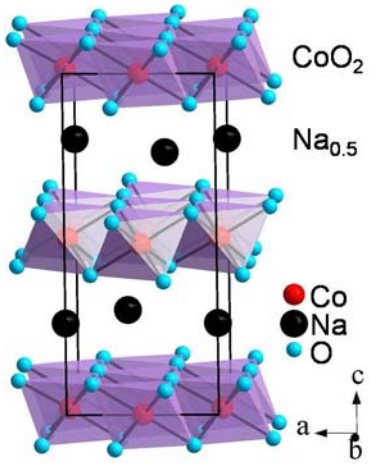

Figure 1.9. Crystal structure of $Na_{0.5}CoO_2$.

On the other hand, *n*-type oxide semiconductors have exhibited relatively low *ZT* values, for example about 0.3 for Al-doped ZnO at 1273 K and 0.37 for an Nb-doped perovskite $SrTiO_3$ epitaxial film at 1000 K which shows the best TE performance to date among *n*-type oxides.[39]

1.4 Research motivation and objective

As previously discussed, good thermoelectric materials are usually composed of heavy elements with complex structures, atomic disorders, or a rattling effect. Due to their attractive thermoelectric properties, there has been a significant amount of research on the binary and some of the ternary tellurides and antimonides. One of the motives for this thesis is to synthesize new complex structure compounds consisting of heavy elements like Te, and Ba. In addition, we will add one or two other elements, such as coinage metals (Cu, Ag, or Au) and group 14 elements (Si or Ge).

Although their thermoelectric performance is not yet stellar, the investigation of oxides is attracting great attention in current research, as did the discovery of the appealing thermoelectric properties of some complex oxides. It is well known that oxides serving as thermoelectric materials have special advantages, such as environmental friendliness, low cost, often low toxicity and high thermal and chemical stability. Due to the strong ionic nature of oxides, it appears that only certain oxide systems – such as the layer structure cobalt series compounds in the *p*-type thermoelectric materials research or the *n*-type doped perovskite – are suitable for thermoelectric applications. Based on the current situation where *n*-type thermoelectric oxides exhibit relatively low thermoelectric performance compared to *p*-type oxides, we decided to optimize the thermoelectric properties of $SrTiO_3$ perovskite with *n*-type doping.

In summary, the objective of this thesis is to synthesize new ternary or quaternary complex structures that may exhibit good thermoelectric properties, and to attempt to optimize the thermoelectric performance of $SrTiO_3$ perovskite with *n*-type doping. Therefore, synthesis, structure and composition characterization, as well as thermoelectric property measurements, will all be major components of this thesis.

1.5 Synthesis of solid state materials

The wide interests in the properties of solid-state compounds and the development of new materials have greatly advanced the techniques for solid-state synthesis. The method used in this thesis is the most widely used ceramic method: two or more non-volatile solids are heated together to form a solid phase product. Both in industry and in the laboratory the ceramic method is commonly used to synthesize a large range of

materials such as oxides, chalcogenides, nitrides, pnictides, intermetallics, aluminosilicates and many others.

1.5.1 Ceramic synthesis method

Solids are not usually ready to react with each other at room temperature, even when the products are thermodynamically favored. Hence, in order to have a proper rate of the reaction, high temperature (typically between 500 and 2000 °C) is essential for ceramic synthesis. The following is an example of a solid-state reaction: a reaction between two crystals of compounds A and B with a contact across one face (Figure 1.11.).[40] The first step in this type of reaction is the nucleation of product C at the interface of A and B. The reaction can only start at the contact points if there is no melting phase, which might be a difficult process if it requires some degree of structural reorganization. After nucleation, a product layer C is formed; therefore, there will be two interfaces available, one between A and C and the other between B and C. For further reaction to occur, ions or atoms of A or B must diffuse through the product C layer. [40]

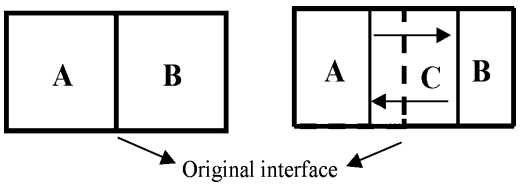

Figure 1.10. Reaction of two components A and B and product layer C after the reaction start.[40]

With the reaction proceeding, the product layer C becomes thicker, resulting in a longer diffusion length and a slower rate of reaction. For simple cases, where the rate of the reaction is controlled by lattice diffusion through a planar layer, the rate can be expressed by the equation $dx/dt = k/x$.[40] Where x is the thickness of the product layer, t

is the time and k is the rate constant. As a general rule, the temperature of solid-state reactions should be above two-thirds of one component's melting temperature to activate the diffusion, since ions or atoms are usually trapped on their appropriate lattice.

From the above example, we can conclude that the rate of a solid-state reaction is mainly determined by three factors:[40]

i. The contact area between the reacting compounds;

ii. The nucleation rate of the product;

iii. Diffusion rates of ions through different phases, especially the product phase.

1.5.2 **Sample preparation and equipment**

All the chalcogenide samples in this work were prepared in an argon-filled glove box with oxygen and water contents below 0.6 ppm, as shown in Figure 1.12.a. In the glove box, stoichiometrically mixed starting materials were loaded into sealed silica tubes, which were transferred to a vacuum line to avoid the presence of oxygen and moisture. An Edward's rotary oil pump (RV5) achieved a vacuum pressure in the order of 10^{-3} mbar measured by Edward's active gauge controller. The silica tubes were then sealed with an oxygen-hydrogen flame that can reach up to 3000 °C. The sealed tubes were finally put into a small manually controlled furnace (Figure 1.12.b) or a programmable box furnace (Figure 1.12.c) with a reaction profile. These resistance furnaces can only be heated up to 1100 °C.

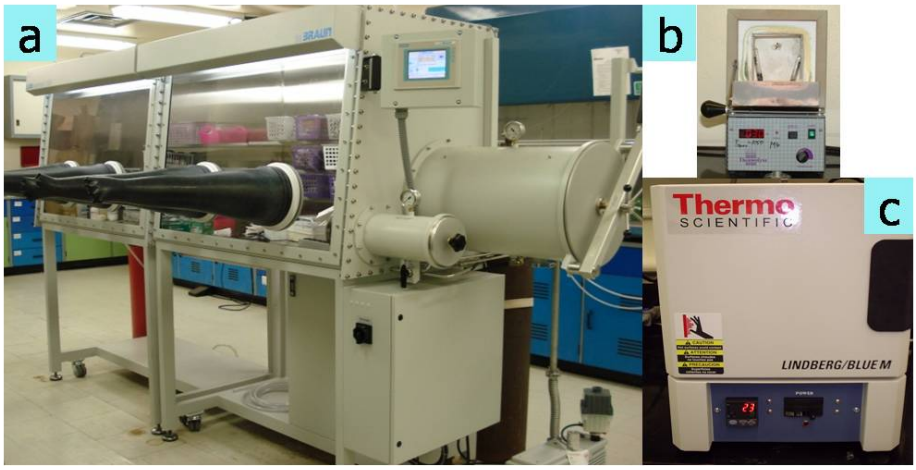

Figure 1.11. a. MBRAUN glove box, b. BL Barnsted 1300 furnace, and c. Lindberg/blue M box furnaces.

For the oxides synthesized in this work, all the starting materials were measured in the stoichiometric ratios and mixed together thoroughly with a mortar and pestle. The mixture was then transferred into an Al_2O_3-based crucible (Al-23 boat, 99.7 % Al_2O_3, Alfa Aesar), as shown in Figure 1.13.a, which was loaded into a tube furnace (Figure 1.13.b). The high temperature furnace can be heated up to 1500 °C under high dynamic vacuum below 10^{-6} mbar, which is achieved by the Diffstak Mk2 oil diffusion pump. To obtain homogeneous samples, the samples needed to be reground and reheated several times. Finally, the samples were pressed into pellets, loaded into a Mo crucible (Figure 1.13.c), then annealed in the induction furnace (Figure 1.13.d). The induction furnace consists of a water cooled copper coil, through which an electric current is passed, thus inducing temperatures up to 2000 °C in the Mo crucible under high dynamic vacuum below 10^{-6} mbar attained via an oil diffusion pump.

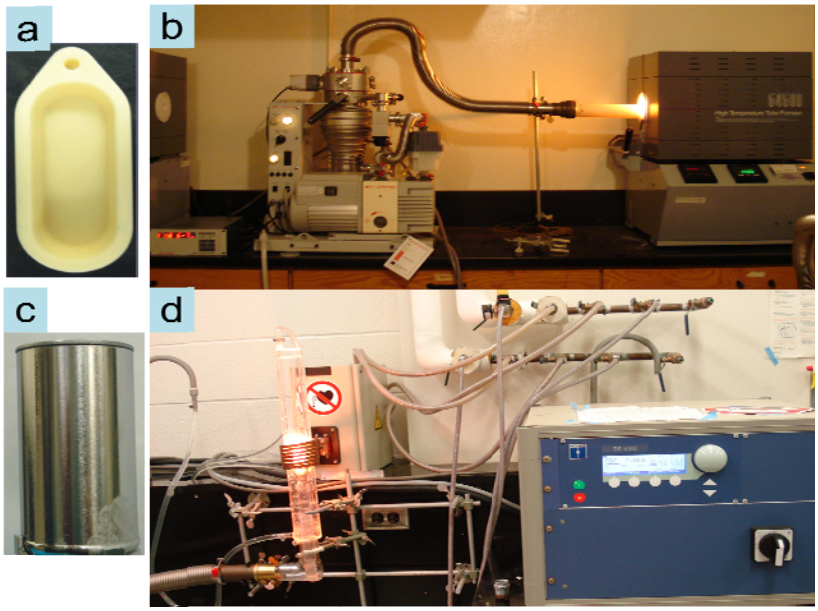

Figure 1.12. a. Al-boat, b. High temperature tube furnace with the Diffstak Mk2 diffusion oil pump, c. Mo crucible, and d. Induction furnace.

1.6 Experimental and theoretical analysis techniques

Sample preparation is the first step of a research project. After that, the experimental and theoretical analyses are more important and time consuming, which might also direct us to refine the sample preparation. Techniques used for the phase purity, composition, structure, as well as theoretical model analyses are introduced below.

1.6.1 X-ray diffraction

X-rays were first discovered by the German physicist Wilhelm C. Röntgen. This discovery earned him the first Nobel Prize in Physics in 1901. However, the nature of X-rays, i.e. wave or particle, was still unsolved. In 1912, Max von Laue discovered the diffraction of X-rays by crystals and thereby proving the wave character of X-rays.

Based on this observation, William Lawrence Bragg noticed the similarity of diffraction to ordinary reflection and deduced a simple equation treating diffraction as "reflection" from planes in the lattice.[41]

$$n\lambda = 2d_{hkl} \cdot \sin\theta_{hkl} \quad \textbf{(1-15)}$$

Where d_{hkl} is the spacing between a set of crystal planes *hkl* (Miller indices) in a crystal, θ_{hkl} is the incident angle to the *hkl* planes, *n* is any integer, and λ is the wavelength of the beam. This formula is known as the Bragg equation (or Bragg's law), which relates the spacing between the crystal planes (d_{hkl}) to the particular Bragg angle (θ_{hkl}) at which reflections from these planes are observed. This law is the basis of powder diffraction instrumentation. [42]

When X-rays strike a crystal, each atom within the crystal will scatter the X-rays; the more electrons an atom possesses, the more strongly it will scatter the X-rays. The scattering amplitude of X-rays of an atom is called scattering factor (or form factor), and is given the symbol f_0. The atomic scattering factor has a strong dependence on the Bragg angle: as the Bragg angle increases, the scattering power drops off, which also depends on the atomic number and the wavelength of the X-ray.[43]

The resultant waves scattered by all the atoms in the unit cell of a crystal, in the direction of the *hkl* reflection, is called the structure factor (F_{hkl}) which is determined by the position of each atom and its scattering factor, as shown in the equation for a unit cell with *j* atoms:[43]

$$F_{hkl} = \sum_j f_j e^{2\pi i(hx_j + ky_j + lz_j)} \quad \textbf{(1-16)}$$

Where f_j is the scattering factor of the *j*th atom and (x_j, y_j, z_j) are its fractional coordinates.

The electron density in a crystal can be calculated with:[43]

$$\rho(x, y, z) = \frac{1}{V}\sum_{h}\sum_{k}\sum_{l} F_{hkl} e^{-2\pi i(hx+ky+lz)} \quad \textbf{(1-17)}$$

Where $\rho(x, y, z)$ is the electron density at a position (x, y, z) in the unit cell and V is the volume for the unit cell. Note the mathematical similarity between equation (1-16) and (1-17). Equation (1-16) transforms the electron density (in the form of atomic scattering factors, f_j) to the structure factors, while equation (1-17) transforms the structure factor back to the electron density. This is known as Fourier transform; one equation performing the inverse transform of the other. Therefore, once the structure factor is known, the electron density distribution in the unit cell, and thus the atomic position, can be calculated.

Since the intensity of a reflection is proportional to the square of the structure factor,[43]

$$I_{hkl} \propto {F_{hkl}}^2 \quad \textbf{(1-18)}$$

The magnitude of the structure factor can be calculated by taking the square root of the intensity:[43]

$$\left|F_{hkl}\right| \propto \sqrt{I_{hkl}} \quad \textbf{(1-19)}$$

The intensity of the *hkl* reflection (I_{hkl}) could be measured by a powder or single crystal X-ray diffractometer, and recorded by the detector for a sample.

1.6.2 **Powder X-ray diffraction**

A powder sample consists of crystalline particles, with sizes ranging from 0.1 to 10 μm, known as crystallites with random orientation. When a powder sample is placed in the path of a monochromatic X-ray beam, the beam will be scattered in all directions

from the planes, which fulfill the Bragg condition, in the crystallites. The resultant reflections lie on the surface of several cones, which may emerge in all directions due to the crystallites oriented randomly to each other. (Figure 1.14.).[44] The sample usually is rotated to bring as many planes as possible into the diffracting situation.

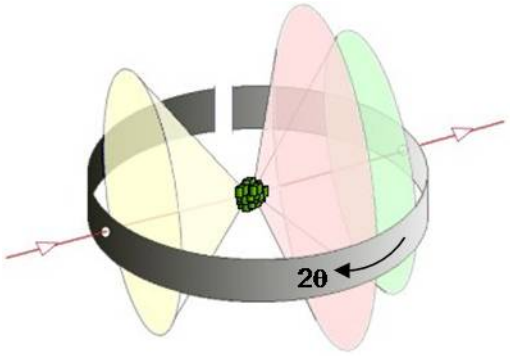

Figure 1.13. Powder diffraction cones produced by a powder sample.[44]

In the past, the cones were recorded as arcs on film by using the Debye-Scherrer photographic method. Currently, the collection of powder diffraction patterns is almost always performed by automatic diffractometers with a scintillation or CCD detector to record the angle and the density of the diffracted beams.[43] The results are generally plotted as intensity, I_{hkl}, against 2θ. From the diffraction pattern, one can obtain information about positions, intensities and shapes of Bragg's reflections, which are determined by the crystal properties. For example, unit cell parameters (dimensions and angles between the axis, $a, b, c, \alpha, \beta, \gamma$) affect peak positions; coordinates of atoms and their scattering factors (x, y, z, f_0) affect intensities and crystallinity, disorders and defects can change the peak shapes.

Powder X-ray diffraction is commonly used to identify unknown substances by comparing diffraction data against a database such as the Inorganic Crystal Structure

Database (ICSD), or the International Center for Diffraction Data (ICDD). When coupled with lattice refinement techniques, such as Rietveld refinement method, powder X-ray diffraction can provide structural information on unknown materials. It can also give an approximation check of the purity of a sample; however, it should be noted that powder diffraction does not detect amorphous products or impurities of less than approximately 5 %.[43] In addition, powder X-ray diffraction can also serve to determine crystallite size or to follow the progress of a solid-state reaction and to determine its reaction mechanisms.

All powder X-ray measurements in this thesis were performed on the INEL powder diffractometer with position-sensitive detector and Cu $K\alpha$ radiation as shown in Figure 1.15.

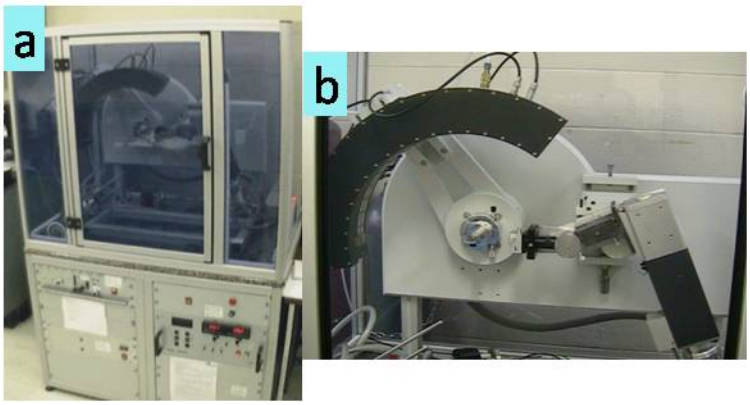

Figure 1.14. a. INEL powder diffractometer, and b. Curved position sensitive detector.

For general qualitative phase analysis, a rapid data collection (10 to 20 minutes) was carried out, but a longer scan (usually 8 hours or more) was sometimes needed to obtain more accurate data required for Rietveld refinements.

In the late 1960s, Dr. Hugo Rietveld[45] proposed a method that could be used to refine a crystal structure from its powder diffraction profile. The Rietveld method was initially only applied to neutron data since they have simple Gaussian peak shapes. In 1977, Malmros and Thomas[46] applied this method to powder X-ray diffraction profile refinement through the utilization of different peak-shape functions (such as Lorentzian and pseudo-Voigt) instead of only Gaussian functions.

The Rietveld method starts with a trial structure, from which a powder diffraction profile is calculated. This profile is then compared to the measured profile. Thereafter the trial structure is refined via the least-square refinement method that minimizes the difference between the observed and calculated profiles, as shown in equation (1-20).[47]

$$S_y = \sum_i w_i (y_i - y_{ci})^2 \qquad \textbf{(1-20)}$$

The sum is over all data points; where S_y is the residual, y_i is the observed intensity at the i^{th} step, y_{ci} is the calculated intensity at the i^{th} step and the weighing factor is $w_i = 1/y_i$. The particular "best fit" obtained will depend on the adequacy of the model and on whether a global minimum rather than a local ("false") minimum has been reached. The model should have approximations on unit cell dimensions and atomic coordinates, as well as the same space group. To judge whether the "best fit" is achieved, several *R*-values have been developed and are now commonly used. For example; R_F : *R*-structure factor, R_p : *R*-pattern and R_{wp} : *R*-weighted pattern.[47]

$$R_F = \frac{\sum \left| \left(I_K(obs)\right)^{1/2} - \left(I_K(calc)\right)^{1/2} \right|}{\sum \left(I_K(obs)\right)^{1/2}} \qquad \textbf{(1-21)}$$

$$R_p = \frac{\sum \left| y_i(obs) - y_i(calc) \right|}{\sum y_i(obs)} \qquad \textbf{(1-22)}$$

$$R_{wp} = \left\{ \frac{\sum w_i \left(y_i(obs) - y_i(calc) \right)^2}{\sum w_i \left(y_i(obs) \right)^2} \right\}^{1/2} \quad \textbf{(1-23)}$$

In these equations, I_K is the intensity assigned to the K^{th} Bragg reflection at the end of the refinement cycles; w_i is the weighting factor for each observed point and is equal to $1/y_i$; $y_i(obs)$ and $y_i(calc)$ are observed and model calculated intensities at the i^{th} step. From a purely mathematical point of view, R_{wp} is the most meaningful of these R's because the numerator is the residual being minimized. For the same reason, it is also the one that best reflects the progress of the refinement.[47]

It should be noted that the success of a structural analysis by the Rietveld method is also directly related to the quality of the powder diffraction data. The X-ray diffractometer must be well aligned, and in addition, an actual calibration file should be used. Rietveld refinements in this thesis were performed on patterns of phase-pure materials using the General Structure Analysis System (GSAS)[48, 49] via the graphical interface EXPGUI.[50]

1.6.3 **Single crystal X-ray diffraction**

It is difficult to use powder X-ray diffraction to determine a crystal structure except for simple high symmetry crystals, though it can be used to identify unknown phases. Provided that sufficiently large crystals of good quality can be obtained, determining the crystal structure by a single crystal X-ray diffraction is the most convenient way. A single crystal X-ray diffractometer can accurately measure the position and intensity of the *hkl* reflections, from which the unit cell dimensions, space group, and the precise atomic positions can be derived. Single crystal X-ray diffraction is currently the most powerful technique used to solve crystal structures.

Nowadays, single crystal data are usually collected using a diffractometer with an area detector. All the single crystal measurements in this thesis were carried out on a Bruker Smart Apex CCD with graphite-monochromatic Mo $K\alpha$ (λ=0.71073 Å) radiation (Figure 1.16.).

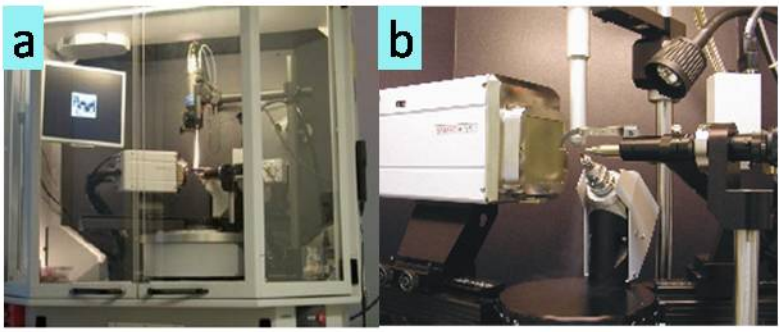

Figure 1.15. a. Bruker Smart APEX CCD, and b. Magnified area detector and the four-circle system.

The SMART[51] software, which is integrated into the APEX2 package, is used for data collection. After collection, the data must undergo some corrections; this is called data reduction. This process includes Lorentz correction (L), related to the geometry of the collection mode; and polarization correction (p), which allows for the fact that the nonpolarized X-ray beam may become partly polarized on reflection.[43] The program SAINT[52] integrated in the APEX2 is used for cell refinement and data reduction. It is also necessary to apply an absorption correction to the collected data, particularly for inorganic structures, since heavier atoms absorb rather than just scatter some of the X-ray beams. The program SADABS[52] is used for absorption correction. After the data reduction is completed, it is time to start solving the crystal structure.

The square roots of the corrected data are taken to give a set of observed structure factors (F_o).

$$|F_o| = \sqrt{\frac{KI_{hkl}}{Lp}} \quad \textbf{(1-24)}$$

Where K is a scaling factor. The quality of collected data can be evaluated by the internal residual value (R_{int}):

$$R_{int} = \frac{\sum \left| F_o^2 - F_{o(\text{mean})}^2 \right|}{\sum F_o^2} \quad \textbf{(1-25)}$$

Only the amplitude of the structure factors, but not their phases could be obtained from the measured X-ray data (equation (1-24)). Both the amplitude and the phase of the resultant waves are needed to calculate the atomic position; this is the so-called phase problem. The calculation of the electron density cannot be performed directly from experimental measurements and the phase must be obtained by other methods, e.g. the Patterson and direct method.[53] The Patterson method is used in systems where the unit cell contains at least one (but not many) heavy atoms, making it very useful for solving molecular inorganic structures. The direct method is commonly used for structures composed of atoms with similar scattering properties. Since our system usually contained several heavy atoms, the chosen method for solving crystal structures was the direct method within the SHELXTL package.[54]

Either the Patterson or the direct method can give the phase values, hence the electron density map of a unit cell. This means that the location of atoms in the structure can be obtained by calculation, therefore, a calculated set of structure factors (F_c) can be determined for comparison with the magnitudes of F_o. The positions of the atoms can then be refined using least-square methods, for which standard computer programs are available in SHELXTL. The quality of the refinement is evaluated by the difference

between the observed and the calculated structure factors, which is called residual index, or *R* factor (R_1) and weighted *R* factor (wR_2) defined as:,

$$R_1 = \frac{\sum \left| |F_o| - |F_c| \right|}{\sum |F_o|} \quad \textbf{(1-26)}$$

$$wR_2 = \sqrt{\frac{\sum w(F_o^2 - F_c^2)^2}{\sum w(F_o^2)}} \quad \textbf{(1-27)}$$

F_o is the observed structure factor and F_c is the calculated structure factor and w is the weighting parameter. *R* factors are commonly used as guides to judge the correctness and precision of a structure determination, but they must be used with caution. In general, the lower the *R* value, the better the structure determination. Actually, a more reliable criterion for judging a good structure determination is to check if low standard deviations on the atomic positions and the bond lengths are obtained together with a low R factor.[43]

1.6.4 **EDX and EPMA analysis**

Energy Dispersive X-ray analysis (EDX) is an analytical technique used for both qualitative and quantitative analysis of the elements present in an irradiated sample. EDX commonly comes with Scanning Electron Microscopy (SEM), which is equipped with a cathode and magnetic lenses to create and focus a beam of electrons. When a high-energy electron beam (usually 10-20 kV) hits an atom of the sample, inner shell electrons of the atom within the sample could be ejected, as shown in Figure 1.17. The formed electron holes are then filled with outer shell electrons of the same atom. The energy difference between the respective shells is emitted as X-rays, which have wavelengths specific to each element. This is the so-called characteristic X-ray.

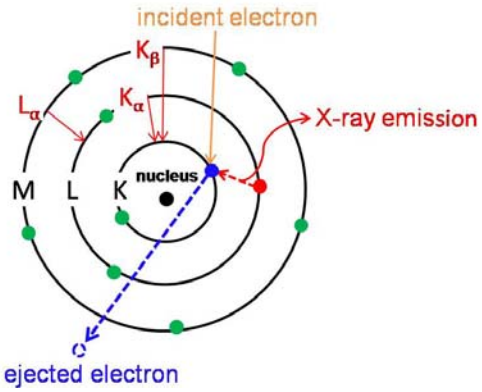

Figure 1.16. Illustration of EDX principle.

The energy of the emitted X-rays is measured in an X-ray detector allowing the identification of the element. The intensities of the peaks in the EDX spectrum represent the concentration of the related element in the tested sample. By calculating the area under the peaks of each identified element (while considering the accelerating voltage of the beam), quantitative analysis can be performed. In addition, EDX mapping can be performed on single spots, lines or on a whole area of a specimen. The EDX analyses in this thesis were performed using a SEM (LEO 1530) with integrated EDX Pegasus 1200.

Electron probe micro analysis (EPMA) is a type of electron microscope technique, which is also based on the measurement of characteristic X-rays of various elements. The characteristic X-rays are detected at particular wavelengths, and their intensities are measured to determine the concentrations. Any element that emits characteristic X-rays can be detected by this method, except for hydrogen, helium, and lithium. In an EPMA measurement, the electron beam current ranges from 10 to 200 nanoamps which is about 1000 times greater than that in a SEM. These high beam currents could stimulate more characteristic X-rays from the atoms of the sample; hence the detection limits and accuracy of the resulting analysis are improved. In addition, a

transmitted-light optical microscope is used to accurately (about 1 micrometer) select analysis locations, which is not available on an SEM. Additionally, the electron microprobe can obtain highly magnified images of a sample like a SEM.

The EPMA measurements described in this thesis were carried out for Nb and Ta substituted perovskites, using the Camera Instrument, Inc. Model SX100 Electron Probe Microanalyzer at Oak Ridge National Laboratory.

1.6.5 **Electronic structure calculation**

Electronic structure calculation is of great importance to material science; it provides the chance to better understand our material and thus predict the properties of new materials or to modify structures to adapt to the requirement of certain applications. To gain insight into the electronic structure of a compound, the Schrödinger equation for many-body wave functions must be solved. In principle, it is possible to solve the many-body Schrödinger equation, but it is too complicated. Density functional theory (DFT) simplifies the problem into a single-particle scheme by appropriate approximations, and has been widely used in condensed matter physics.[55]

The band theory of solids is related to that of the Molecular Orbital (MO) theory. The MO theory is based on the linear combination of atomic orbitals (LCAO), which is derived from the assumptions that molecular orbitals are formed from the overlap of atomic orbitals, which only interact significantly when they have approximately the same energy, and the interaction will result in bonding, antibonding or nonbonding molecular orbitals.

To extend the MO theory to solids, a chain of equally spaced hydrogen atoms is considered first (Figure 1.18.).

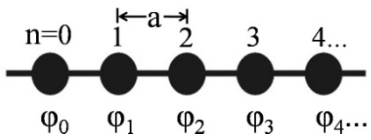

Figure 1.17. Chain of H atoms.

For every lattice point, labeled by index *n* (*n*=0, 1, 2, …), there is a basis function (a H 1*s* orbital): φ_1, φ_2, φ_3, …, with "*a*" as lattice spacing. Considering the periodic nature of a crystal lattice using the symmetry operations, the Schrödinger equation can be solved for the crystal:

$$\psi_k = \sum_n e^{ikna}\varphi_n \qquad \textbf{(1-28)}$$

The symmetry-adapted function ψ_k is called a Bloch function:[56] Here *k* is called the wavevector, and is related to the direction of motion of the electron in the crystal. It has unique values within the first Brillouin zone (BZ), $-\pi/a \le k \le \pi/a$, which is different for different Bravais lattices. Depending on the *k* values, different combinations of orbitals are possible. Figure 1.19. exhibits the two combinations for $k = 0$ and $k = \pi/a$ resulting in the bonding and antibonding scenario, respectively.

$$k = 0 \quad \psi_0 = \sum_n e^0\varphi_n = \sum_n \varphi_n$$

$$= \varphi_0 + \varphi_1 + \varphi_2 + \varphi_3 + \varphi_4 + \ldots$$

$$k = \frac{\pi}{a} \quad \psi_{\pi/a} = \sum_n e^{\pi i n}\varphi_n = \sum_n (-1)^n \varphi_n$$

$$= \varphi_0 - \varphi_1 + \varphi_2 - \varphi_3 + \varphi_4 - \ldots$$

Figure 1.18. Orbital combination at point *k* = 0 (top) and *k* = *π/a* (bottom).

Applying Bloch's theorem in all three crystallographic directions, band structure calculations for a three-dimensional lattice are possible by letting k vary through the three-dimensional Brillouin zone. A larger number of k points will result in more accurate calculations of the total crystal energy.

There is an degenerate energy level $E(k)$ for each pair of k and $-k$, due to $E(k) = E(-k)$, so $E(|k|)$ is plotted and labelled as $E(k)$ in most representations. Graphs of $E(k)$ vs. k are called band structures (Figure 1.20.).

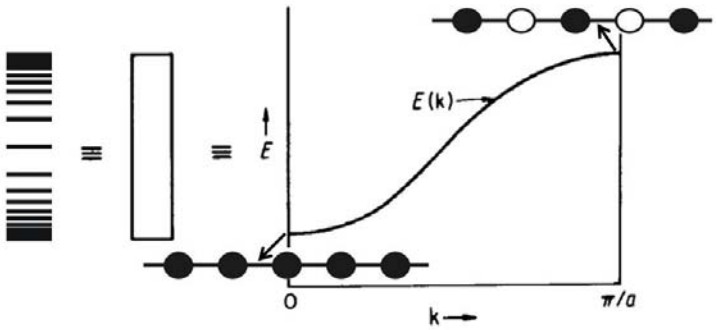

Figure 1.19. Plot of $E(k)$ vs. k (band structure) of a chain of equally spaced H atoms.

One very important feature of a band is its band width, which is the difference in energy between the highest and lowest levels in the band, which depends on the overlap between the interacting orbitals. Another feature of a band is the way the bands are running, either "uphill" or "downhill", which is determined by the topology of the overlap.

Any given solid has a very large number of energy levels or states. This is not like the frontier or valence orbitals in a molecule, which can direct the geometry or reactivity – a single orbital or just a small group of orbitals in a solid rarely have the power to do that. This problem can be solved by considering not just one level but all the

levels in a given energy interval. The density of states (DOS) is defined as DOS(E) dE = number of energy levels between E and $E+dE$.[57] Since the energy levels are equally spaced along the k axis, the DOS can be related to the band structure. In general, DOS(E) is inversely proportional to the slope of $E(k)$ (Figure 1.21.). This implies that the flatter the bands, the greater the DOS at that energy level in a 1-D system.

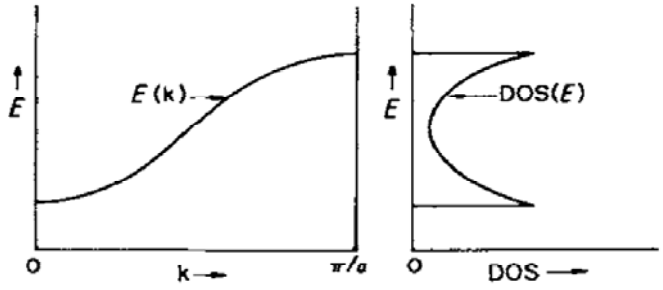

Figure 1.20. Relationship between DOS and band structure for a hypothetical chain of H atoms.[57]

The DOS curve counts the total number of levels at a given energy. The integral of the DOS up to the Fermi level corresponds to the total number of occupied states. The total number of occupied states doubled, is the total number of electrons, so the DOS curve plots the distribution of electrons at different energy levels.

In the MO theory, bonding characteristics depend on orbital interactions. The distribution of an electron in a simple two-centre molecular orbital ($\psi = c_1\varphi_1 + c_2\varphi_2$) is given by Ψ^2:

$$\int \Psi^2 d\tau = 1 = \int \left| c_1\varphi_1 + c_2\varphi_2 \right|^2 d\tau = c_1^2 + c_2^2 + 2c_1c_2S_{12} \qquad (1\text{-}29)$$

$2c_1c_2S_{12}$ is the quantity associated with the interaction and it is called the overlap population suggested by Mulliken.[58] The sum, $2c_ic_jS_{ij}$, over all orbitals on a given pair of atoms, is called "Mulliken overlap population" (MOP).[59] Where a solid is concerned,

the integration of the MOP of all states in a given energy interval is the Crystal Orbital Overlap Population (COOP).[60] When the overlap that is integral for a specific bond possesses a positive value, the interaction is bonding; thus a negative value results in antibonding. Figure 1.22. presents the relationship between the band structure, DOS and COOP curves of a simple chain of H atoms. The interaction between the nearest hydrogen atoms (1 and 2): the bottom of the band is bonding, the middle is nonbonding and the top is antibonding. For a different interaction, for example the interaction between atoms 1 and 3 (the bottom and the top of the band are bonding, and the middle is antibonding), the COOP curve (dashed line) is different.

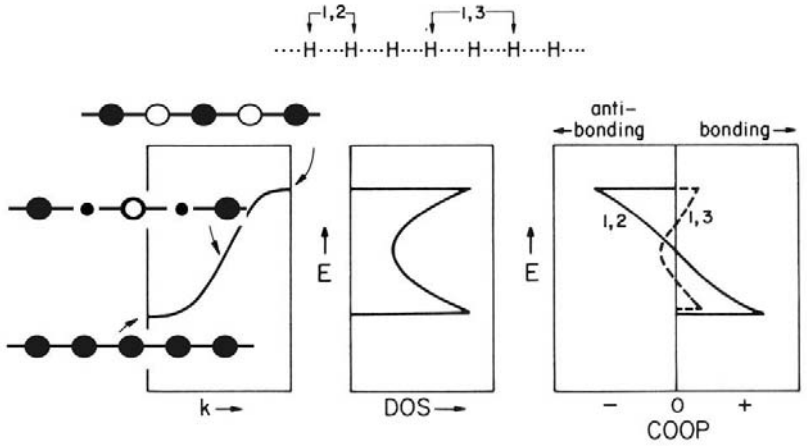

Figure 1.21. Band structure, density of states and COOP curves for a chain of H atoms.

The intensity of the COOP curves is determined by the number of states in a given energy range, the magnitude of the overlap and the size of the coefficients in the MOs.[57] In DFT calculations, the Crystal Orbital Hamilton Population (COHP)[61], and the integrated COHP values (ICOHPs)[62] can be used for the investigation of different bonding interactions and their strengths in the compounds. A COHP curve also indicates bonding, nonbonding and antibonding energy contributions in a specific energy range;

the integration over all filled states will result in ICOHP values, which are analogous to the MOP obtained from COOP curves. Since COHP partitions the band structure energy instead of the electron number in COOP, the signs of the ICOHP values are different from MOP. Negative ICOHP values show the bonding character of an interaction; moreover, ICOHP values have the units of eV per bond, while the unit of MOP values is electrons per bond.

The density of states and the band structures are the most important pieces of information that can be deduced from the electronic structure of a compound. This information is of great importance to thermoelectric material research, for the band shape (flat or steep bands) affects the conduction process. In a free-electron gas model, the energy (E) is proportional to the square of the wave vector k:[63]

$$E = \frac{h^2 k^2}{8\pi^2 m^*} \quad \textbf{(1-30)}$$

Where h is Planck's constant and m^* is the effective mass of the charge carriers. Charge carriers (electrons or holes) in a crystal are analogous to free particles in a vacuum in response to electric and magnetic fields, with the exception of a different mass, which is the effective mass (depending on the direction it travels), usually in the range of 0.01 or 10 electron m_e. The first derivative of E versus k is the measurement of the band dispersion and the second derivative is inversely proportional to the effective mass, m^*:

$$\frac{dE}{dk} = \frac{h^2 k}{4\pi^2 m^*} \quad \textbf{(1-31)}$$

$$m^* = \frac{h^2}{4\pi^2}\left(\frac{1}{d^2E/dk^2}\right) \quad \textbf{(1-32)}$$

The carrier mobility and the energy can also be directly related to the first derivative of E versus k through band velocity $v=p/m^*$ and the de Broglie equation, $p=hk/2\pi$ (p is the momentum):

$$v = \frac{2\pi}{h} \cdot (\frac{dE}{dk}) \quad \textbf{(1-33)}$$

Large band dispersions or band widths (steep bands) will result in high carrier mobility and large conductivity, while small band dispersions (flat bands) result in a large effective mass and a high Seebeck coefficient. Coexistence of both flat bands and steep bands around the Fermi level will be the ideal condition to have the optimum conductivity and Seebeck coefficient in one compound.

The DOS provides similar information. According to Mahan et al.,[64] the Seebeck coefficient is proportional to the first derivative of the density of states (DOS) with respect to energy (E) above and below the Fermi level :

$$S \propto \frac{1}{DOS(E)} \cdot \frac{d\ DOS(E)}{dE}\bigg|_{E=E_F} \quad \textbf{(1-34)}$$

$$\sigma \propto DOS(E)\big|_{E=E_F} \quad \textbf{(1-35)}$$

The electrical conductivity (σ) increases with DOS(E), therefore, increasing DOS (E) will increase σ and decrease S.

For electronic structure calculations in this research, the Tight-Binding Linear Muffin-Tin Orbital method (TB LMTO) with the Atomic Spheres Approximation (ASA)[65, 66] was used. Therein, the density functional theory was employed utilizing the local density approximation (LDA) for the exchange and correlation energies.[67] Since it uses the linear method for calculations, it is much faster than the augmented plane wave approach (APW).[56] The LMTO method is particularly good for close packed structures.

The integrations in k space are performed by an improved tetrahedron method [68] on k points evenly spread throughout the first Brillouin zone.

1.7 Measurements of physical properties

As discussed above, a thermoelectric material is usually characterized by the dimensionless figure of merit ZT, which depends on the electrical conductivity, Seebeck coefficient and thermal conductivity. Physical property measurements, therefore, are vital for thermoelectric material research. Electrical conductivity is usually calculated from the electrical resistivity measurement, the Seebeck coefficient is measured directly and thermal conductivity is calculated from the thermal diffusivity measurement. Physical properties for the oxides that were developed during this thesis have been determined at four different institutions, the University of Waterloo, Clemson University, General Motors Research & Development Center in Warren, and Oak Ridge National Laboratory. The properties of the chalcogenides were all determined at the University of Waterloo.

1.7.1 Seebeck coefficient measurement

The Seebeck measurements for all the tellurides in this thesis were carried out with the MMR Programmable Seebeck Measurement System which includes the SB-100 Programmable Seebeck controller, the K-20 Temperature Controller, the Seebeck Thermal Stage and accessories, cold stage, an Edward's rotary oil pump (RV5), a computer, and MMR supplied software,[69] as shown in Figure 1.23.a. The Seebeck Thermal Stage includes two pairs of thermocouples; one pair was formed with junctions of silver and a reference material (Constantan: Cu : Ni = 55:45 wt %) of known Seebeck

coefficient. The other pair was formed with junctions of silver and a sample pellet whose Seebeck coefficient was to be determined. The pressed rectangular (6×1×1 or 5×1×1 mm^3) sample was mounted on the thermal stage (Figure 1.23.b) with silver paint (Leitsilber 200 silver paint, TED PELLA INC.).

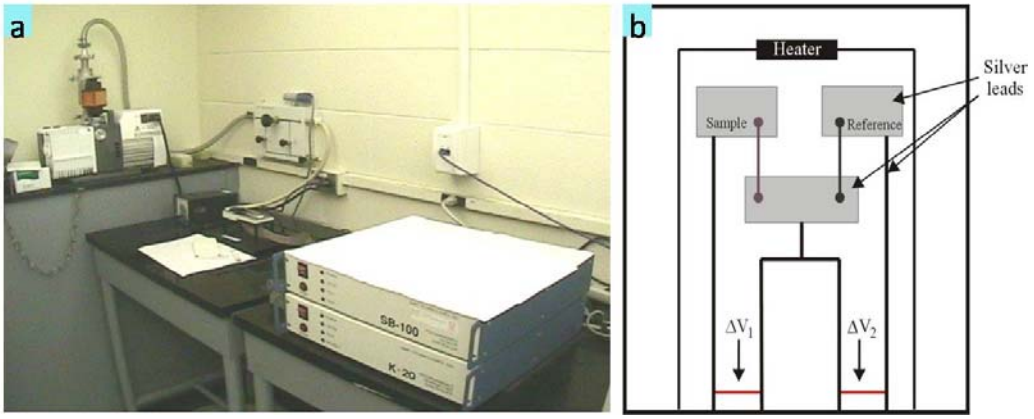

Figure 1.22. a. MMR Seebeck measurement system, b. Seebeck thermal stage.

The Seebeck stage was attached to the cold stage of the MMR K20 temperature controller. The programmable Seebeck controller was used to control the heater to produce the temperature difference between the two ends of the sample as well as the reference. The generated temperature difference is a function of the power applied to the heater. When the power (P) is applied to the heater, the voltage can be measured for the sample and reference, ΔV_1 and ΔV_2, respectively.

$$\Delta V_1 = S_1 \times \Delta T(P) \quad \textbf{(1-36)}$$

$$\Delta V_2 = S_2 \times \Delta T(P) \quad \textbf{(1-37)}$$

$$S_1 = S_2 \times \frac{\Delta V_1}{\Delta V_2} \quad \textbf{(1-38)}$$

In a measurement, a small applied temperature difference (though that will result in low ΔV_1 and ΔV_2 values, hence low accuracy) is preferred; since the length of the pellet and reference is very small, a high temperature difference could not be accurately achieved. In addition, the instrumental errors and thermo-voltage effects of wires and connectors should also be considered to prevent substantial offset voltages ($\Delta V_1^\circ, \Delta V_2^\circ$). Measuring the sample and the reference at two different temperatures with two different powers, P_1 and P_2, then using the difference signal, could eliminate these errors:

$$\Delta V_1(P_1) = S_1 \times \Delta T(P_1) + \Delta V_1^\circ \quad \textbf{(1-39)}$$

$$\Delta V_2(P_1) = S_2 \times \Delta T(P_1) + \Delta V_2^\circ \quad \textbf{(1-40)}$$

$$\Delta V_1(P_2) = S_1 \times \Delta T(P_2) + \Delta V_1^\circ \quad \textbf{(1-41)}$$

$$\Delta V_2(P_2) = S_2 \times \Delta T(P_2) + \Delta V_2^\circ \quad \textbf{(1-42)}$$

Therefore S could be calculated as:

$$S_1 = S_2 \times \frac{\Delta V_1(P_1) - \Delta V_1(P_2)}{\Delta V_2(P_1) - \Delta V_2(P_2)} \quad \textbf{(1-43)}$$

Utilizing the Seebeck system, all of these processes were finished automatically. The MMR Seebeck system allows the temperature of the MMR cold stage and the attached Seebeck stage to be controlled over a wide temperature range (from 300 K to 550 K).

1.7.2 **Electrical conductivity measurement**

The electrical resistivity measurement was performed on a homemade four-point measurement system, as shown in Figure 1.24.

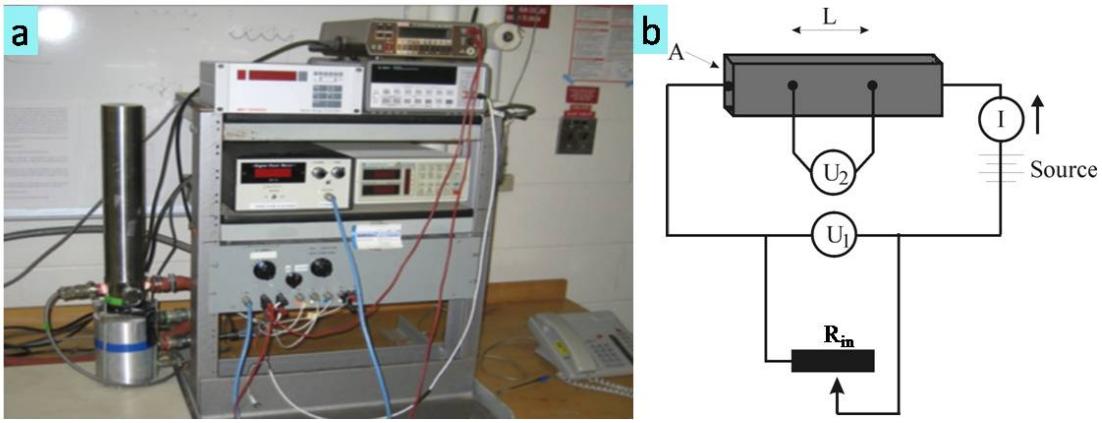

Figure 1.23. a. Homemade electrical conductivity measurement system, b. Illustration of 4-point method.

Usually the same pellet used for Seebeck measurements was used for electrical resistivity measurements as well. The bar-shaped pellet was connected to the measurement system by four silver wires with silver paint (Leitsilber 200 silver paint, TED PELLA INC.). The pellet chamber was then evacuated by an Edward's rotary oil pump (RV5) and cooled by a helium compressor to obtain temperature dependent resistance values for the sample. A variable internal resistance (R_{in}) was used to adjust the magnitude of an electrical current (I, $I = U_1/R_{in}$) passing through the sample. The voltage drop (U_2) read between two middle contacts in the sample, together with the electrical current (I), was used to calculate the electrical resistance ($R = U_2/I$) between the two middle contacts, hence the specific resistivity ($\rho = R \times A/L$) could be calculated. Since $\sigma = 1/\rho$, the temperature dependant electrical conductivity could be obtained.

1.7.3 **Thermal conductivity determination**

Another property that determines thermoelectric material performance is thermal conductivity, which is defined as the ability of a material to conduct heat. Direct thermal

conductivity measurements are not only difficult, but also time consuming, since steady-state conditions are invariably required. Therefore, thermal conductivity is usually determined by the measurement of thermal diffusivity (α), specific heat (C_p) and density (d) through equation (1-44):

$$\kappa = \alpha \times d \times C_p \qquad \textbf{(1-44)}$$

One of the widely used methods to measure thermal diffusivity is the flash method, as illustrated in Figure 1.25., which could also be used to measure C_p. In 1961, Parker et al. developed the flash method in the US radiological defense laboratory.[70] In this technique, the front face of the sample is irradiated by a short laser pulse or Xenon flash lamp. An IR detector, which is located in front of the rear face of the sample and cooled by liquid nitrogen, records the temperature changes of the rear face as a function of time. The time required for the rear face to reach the maximum temperature is related to the thermal conductivity of a given material.

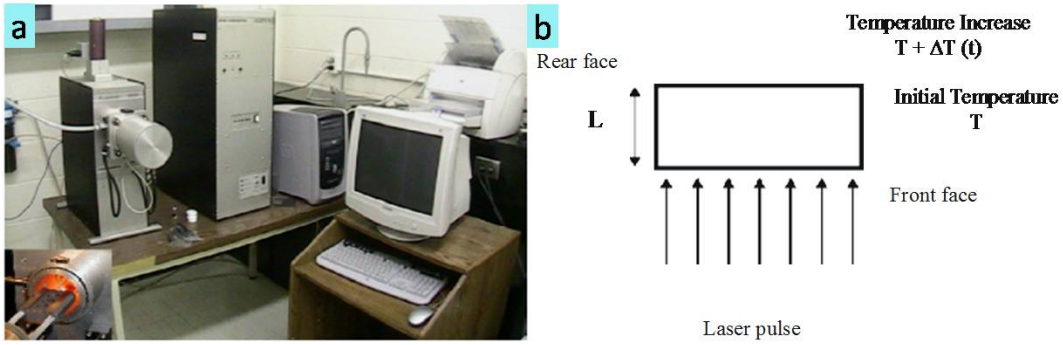

Figure 1.24. a. Flash Line 3000 thermal diffusivity system, b. Illustration of flash method.[71]

In practice, most researchers use the equation (1-45) to calculate the thermal diffusivity (α):

$$\alpha = 0.1388 \times \frac{L^2}{t_{1/2}} \quad \textbf{(1-45)}$$

where L is the thickness of the sample and $t_{1/2}$ is the time required for the rear face to reach half of the maximum temperature rise.

By definition, the amount of energy required for increasing the temperature by one degree of one gram or one mole of a material at a constant pressure is the specific heat, as shown in equation (1-46).[72]

$$C_p = \frac{dH(T)}{dT} \cdot \frac{1}{m} \quad \textbf{(1-46)}$$

Where dH is the change in enthalpy, dT is the change in temperature and m is the mass of the material. There are two ways to determine the specific heat; one is to measure it, and the other is to calculate it from the Dulong-Petit law. Experimentally, specific heat can be measured by the ratio method using a standard material with a known C_p value. The differential scanning calorimeter (DSC) measurements for a standard material and the sample are carried out, and then the specific heat is calculated by:[73]

$$C_{p,sample} = \frac{m_{standard}}{m_{sample}} \cdot \frac{DSC_{sample} - DSC_{baseline}}{DSC_{standard} - DSC_{baseline}} \cdot C_{p,standard} \quad \textbf{(1-47)}$$

In addition, due to the fact that the molar specific heat of most solids is almost constant at high temperature, the specific heat of solids at high temperature is usually calculated by the Dulong-Petit law.[74]

$$C_p = \frac{3R}{M_M} \quad \textbf{(1-48)}$$

Where R is the gas constant and M_M is the average molar mass ($gmol^{-1}$) of the compound. The thermal diffusivity measurements in the Kleinke laboratories were carried out on the

Flash Line 3000 thermal diffusivity system from ANTER Corp., and the specific heat was usually calculated using the Dulong-Petit law.

Chapter 2 Two Isostructural Ternary Polytellurides: $Ba_7Au_2Te_{14}$ and $Ba_{6.76}Cu_{2.42}Te_{14}$

Thermoelectric materials are now receiving renewed attention, as evident from groundbreaking discoveries made in the last 20 years, for the most part centered on antimonides and tellurides.[22, 25, 35, 75-77] This is because of a well known fact that materials consisting of heavy elements generally have low lattice thermal conductivity, which is important to achieve a high *ZT* thermoelectric material. Due to their high electrical conductivity, investigations of heavier coin metal chalcogenides are a vital part of thermoelectric material research. Several binary, ternary and quaternary copper and silver chalcogenides were examined, including $Cu_{2-\delta}Te$,[78] α- and β-Ag_2Te,[79] $BaCu_2Te_2$,[80] $Ba_3Cu_{14}Te_{12}$,[81] and $A_2BaCu_8Te_{10}$ (A = K, Rb, Cs),[82] $BaCu_2SnSe_4$,[83] $BaAg_2SnSe_4$,[83] and $Ba_3Cu_2Sn_3Se_{10}$,[83] Ag_8GeTe_6,[84] AgTlTe,[85] $AgSbTe_2$,[86] $Ag_{3-\delta}Sb_{1+\delta}Te_4$,[87] $(AgBiTe_2)_{1-\delta}(Ag_2Te)_\delta$,[88] $(AgSbTe_2)_{1-\delta}(GeTe)_\delta$ (TAGS)[89, 90] and $AgPb_mSbTe_{2+m}$,[25] to name a few recent studies. Gold chalcogenides are appealing, as they should have similar electrical transport properties, but lower thermal conductivity because of their higher molar masses. Only a few gold tellurides are known; e.g. only one binary gold telluride exists, the calaverite $Au^{III}Te_2$,[91] which forms an incommensurate super cell.[92] The ternaries $CuAuSe_2$[93] and Ag_3AuTe_2[92] are also narrow gap semiconductors with trivalent gold, Au^{III}, but Cu^I and Ag^I. This chapter deals

with the first ternary barium gold telluride, which is isostructural with a (new) copper telluride, while the known binary gold and copper tellurides are quite different.[94]

2.1 Synthesis and analysis

All reactions were commenced from the elements, which were obtained in purities of at least 99%, and stored in an argon filled glove box. $Ba_7Au_2Te_{14}$ was first obtained in an attempt to prepare the hypothetical "$BaAuTe_2$", after starting from 1 mmol Ba, 1 mmol Au, and 2 mmol Te. This mixture was loaded into a fused silica tube, heated to 800 °C within 48 hours, kept at that temperature for two hours, and then cooled to 200 °C with a ramp of 3 °C per hour, followed by switching off the furnace. This reaction yielded at least one unknown material, besides unreacted gold, as evident from the powder X-ray patterns obtained from the ground sample. After solving this structure via single crystal structure determination, described below, all peaks of the powder diagram could be assigned to this new material, namely $Ba_7Au_2Te_{14}$, and elemental gold. Subsequently, phase pure $Ba_7Au_2Te_{14}$ was synthesized via the same method, including the same temperature profile, starting from the stoichiometric 7 : 2 : 14 ratio, as shown in Figure 2.1.

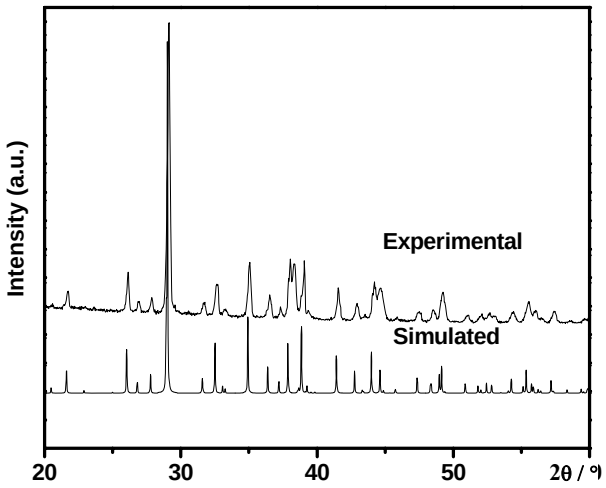

Figure 2.1. Experimental and simulated powder XRD patterns for $Ba_7Au_2Te_{14}$.

Attempts to synthesize analogous copper and silver tellurides were successful only in the case of copper, and no isostructural selenide was found. The copper analog was prepared using the same temperature profile, but a subsequent single crystal structure study revealed a significant deviation from the 7 : 2 : 14 ratio of the elements, which was observed for $Ba_7Au_2Te_{14}$, namely $Ba_{6.76}Cu_{2.42}Te_{14}$. Attempts to prepare phase-pure stoichiometric "$Ba_7Cu_2Te_{14}$" failed, but a reaction starting from the elements in the refined ratio of 6.76 : 2.42 : 14 yielded a pure sample without noticeable side products.

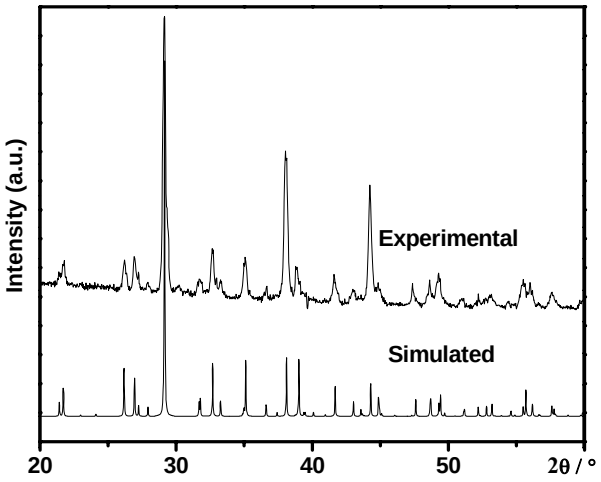

Figure 2.2. Experimental and simulated powder XRD patterns for $Ba_{6.76}Cu_{2.42}Te_{14}$.

Energy dispersive X-ray analysis (EDAX) did not reveal any heteroelements, such as silicon that might have come from the silica tube. The distribution of the elements Ba, Cu/Au, and Te was homogenous throughout the sample. Averaged over five crystals, the Ba : Au : Te ratio was 29.5 : 8.4 : 62.0 in atomic percentage, which compares well with the refined 7 : 2 : 14 ratio (≡ 30.4 : 8.7 : 60.9). For the Cu sample, we calculated the Ba : Cu : Te ratio to 28.6 : 9.0 : 62.3 in atomic percentage, which is in reasonable agreement with the refined ratio of 6.76 : 2.42 : 14 (≡ 29.2 : 10.4 : 60.4).

2.2 Crystal structure

2.2.1 Crystal structure determinations

In both cases, 606 frames were measured with exposure times of 60 seconds each. The data were corrected for Lorentz and polarization effects. Absorption corrections were based on fitting a function to the empirical transmission surface as sampled by multiple equivalent measurements of numerous reflections.[95]

The unit cell dimensions indicated the adoption of the $NaBa_6Cu_3Te_{14}$ type, hexagonal space group $P6_3/mcm$.[96] Therefore, the refinements using the SHELXTL package[54] commenced from that structure model, with Ba on the Na site (Ba2). In the case of the gold compound, Au was assumed to sit on the Cu position. That refinement converged to residual factors of $R1 = 0.0794$ and $wR2 = 0.2130$ (observed data). Because of the conspicuously high displacement factor of the Au site (0.0415(6) $Å^2$), its occupancy was refined, resulting in 66.5(3) %, an inconspicuous displacement factor of 0.0241(2) $Å^2$, and lower R values, namely $R1 = 0.0369$ and $wR2 = 0.0702$. On the other hand, while the displacement factor of Ba2 was significantly higher than that of Ba1, refining the occupancy of Ba2 revealed full occupancy within one standard deviation, without a change in the residual values.

In case of the copper compound, the refinements yielded clear deficiencies of both sites in question, with refined occupancies of 61.7(8) % for Cu1 and 76(1) % for Ba2. This led to lowered R values, e.g. R1 decreased from 0.0550 to 0.0428. The difference Fourier map comprised an additional peak of 6 e/$Å^3$, surrounded by three Te atoms with distances of 2.5 Å and 2×2.8 Å. This position was subsequently refined as a

deficient Cu site, Cu2, with an occupancy of 9.5(7) %, a procedure that further decreased R1 to 0.0369.

In the end, the refined formulas of the two compounds were $Ba_7Au_{1.995(9)}Te_{14}$ and $Ba_{6.76(1)}Cu_{2.42(7)}Te_{14}$. Crystallographic details are given in Table A.2.1., and atomic positions, displacement and occupancy factors in Table A.2.2.

2.2.2 Crystal structure of $Ba_7M_2Te_{14}$

The two new ternary tellurides, $Ba_7Au_{1.995(9)}Te_{14}$ and $Ba_{6.76(1)}Cu_{2.42(7)}Te_{14}$, for simplicity called $Ba_7M_2Te_{14}$, crystallize in substitution variants of the $NaBa_6Cu_3Te_{14}$ structure, briefly described in a communication,[96] where the Na site is filled with Ba2. A second Cu site, Cu2, is partly filled in case of the ternary Cu telluride, which may be seen as a split position of Cu1. The crystal structure of $Ba_7M_2Te_{14}$ is comprised of MTe_4 tetrahedra, which are interconnected through corners to form planar M_3Te_3 rings, which in turn are connected to Te_3 units. The rings are stacked along [001], surrounding the Ba2 atoms. Nine-fold Te-coordinated Ba1 atoms connect the rings in the *ab* plane, and additional Te atoms, Te4, are located between six Ba1 atoms. Figure 2.3. shows a projection of the $Ba_7M_2Te_{14}$ structure along the *c* axis, highlighting the covalent M–Te and Te–Te interactions.

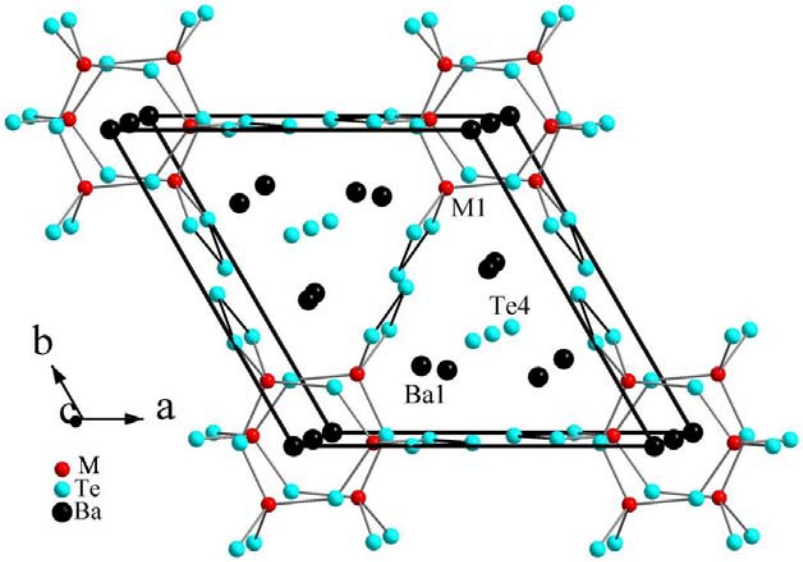

Figure 2.3. Crystal structure of $Ba_7M_2Te_{14}$ (excluding the Cu2 site).

The Ba1–Te bonds (Table A.2.3.) are inconspicuous, ranging from 3.50 Å to 3.66 Å ($Ba_7Au_2Te_{14}$) and 3.51 Å to 3.64 Å ($Ba_{6.76}Cu_{2.42}Te_{14}$). The nine-fold coordination of Ba1 compares well with the nine Ba–Te bonds per Ba atom in $BaSbTe_3$ (3.41 Å – 3.89 Å)[97], Ba_2SnTe_5 (3.44 Å – 3.84 Å),[98] and $Ba_3Cu_{14}Te_{12}$ (3.47 Å – 3.84 Å).[81] Similarly, the Ba2–Te bonds of the $Ba2Te_6$ octahedron (3.50 Å in $Ba_7Au_2Te_{14}$, 3.39 Å in $Ba_{6.76}Cu_{2.42}Te_{14}$) are reminiscent of the bonds in BaTe (3.42 Å, NaCl type).[99]

In $Ba_7Au_2Te_{14}$, the four Au1–Te bonds of 2× 2.70 Å and 2× 2.87 Å, averaged to 2.78 Å, are longer than expected for Au^{III}, as found in the sylvanite $AgAuTe_4$ (four bonds between 2.67 Å and 2.69 Å),[100] and $CrAuTe_4$ (4× 2.68 Å).[101] Moreover, the tetrahedral Cu1 coordination sphere with distances of 2.63 Å – 2.76 Å of $Ba_{6.76}Cu_{2.42}Te_{14}$ is typical for Cu^I: for example, the Cu^I–Te bonds of $BaCu_2Te_2$ range from 2.59 Å to 2.81 Å,[80] and in $Ba_3Cu_{14}Te_{12}$ from 2.50 Å to 2.85 Å.[81] The coordination of the Cu2 site is highly irregular, with distances to Te atoms of 2.49 Å, 2× 2.78 Å, and 3.14 Å. It is noted that

the shortness of the Cu1–Cu2 distance (1.59 Å) necessitates that the two positions are never filled at the same location within the crystal. This concurs well with the combined occupancies being below 100 % (62 % for Cu1 and 10 % for Cu2). Such a scenario is common in copper chalcogenides, e.g. in $LnCu_{0.3\text{-}0.4}Te_2$,[102] $CuGd_3Cu_2Te_7$,[103] $Cu_{2-\delta}Se$,[104] $CuSm_3Se_6$,[105] and in $Cu_4Bi_4Se_9$,[106] but not in gold chalcogenides.

The shortness of the Cu2–Ba2 distance of 2.33 Å requires that these two positions are also never occupied at the same location within a crystal. Because of the low occupancies of 10 % for Cu2 and 76 % for Ba2, this can be realized in the whole crystal. As a consequence of this scenario, the Cu atoms cannot migrate from one ring to the other along the *c* axis, as the Ba2 site, where filled, would prevent this (Figure 2.4.). Since the rings are well separated in the *ab* plane, any Cu ion movement is restricted to occur only locally within a Cu_3Te_3 ring.

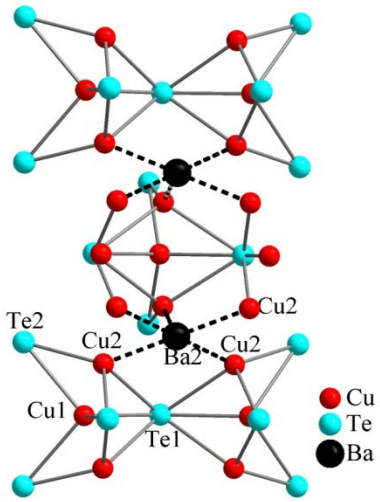

Figure 2.4. Three Cu_3Te_3 rings stacked along [001] showing both the Cu1 and Cu2 atoms, dashed lines between Ba2 and Cu2 are not real bonds.

Figure 2.5. compares the planar $Cu1_3Te_3$ and puckered $Cu2_3Te_3$ rings, including the attached V-shaped Te_3 units. These rings are staggered along the *c* axis (6_3 screw

axis running through their center), thereby surrounding the Ba2 cation with six Te atoms in octahedral coordination.

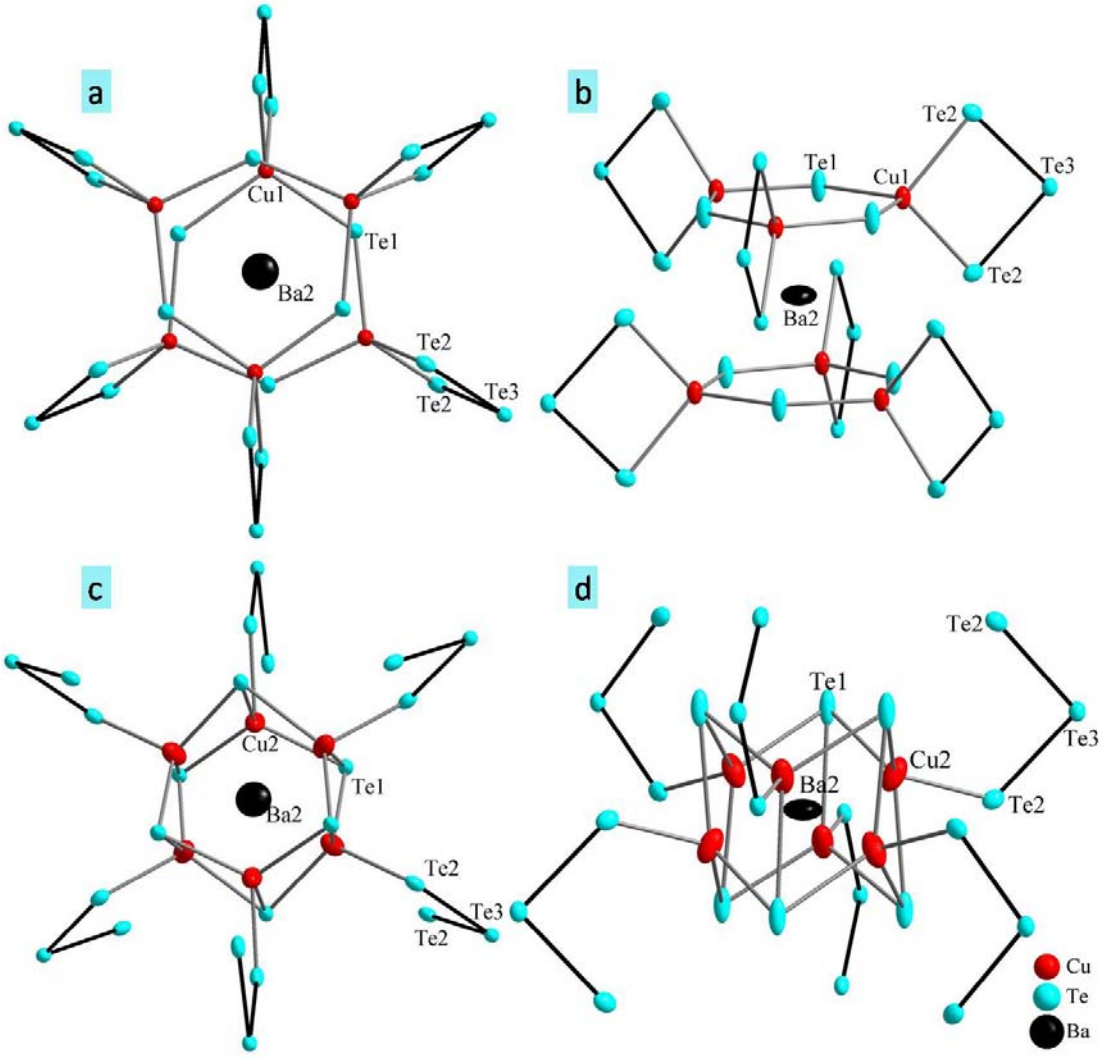

Figure 2.5. Top: two $Cu1_3Te_3$ rings including the attached Te_3 units surrounding the Ba2 atom(ellipsoid presentation). a: viewed along the *c* axis; b: projected onto the *ac* plane. Bottom: two $Cu2_3Te_3$ rings including the attached Te_3 units surrounding the Ba2 atom. c: viewed along the *c* axis; d: projected onto the *ac* plane.

The presence of the Cu2 site seems to have an impact onto the Te1 site, which is part of the Cu_3Te_3 ring, as the Te1 site exhibits strong anisotropies in the displacement factors, reflected in a U_{33}/U_{11} ratio of 4.8 : 1, with $U_{11} \approx U_{22}$. The corresponding Te1 of

$Ba_7Au_2Te_{14}$ exhibits a smaller, more regular, $U_{33} : U_{11}$ ratio of 2.7 : 1, also with $U_{11} \approx U_{22}$. Similar $U_{33} : U_{11}$ ratios were observed for the Au1 and Cu1 sites, indicating a tendency to deviate from the planarity of the M_3Te_3 ring. It is noted that none of these sites could be refined as a split site. Moreover, lowering the symmetry to allow for nonplanarity by selecting the space group $P6_3cm$ did not lead to any improvements or a significant nonplanarity of this ring.

The Te_3 units, formed by the Te2 and Te3 atoms, exhibit rather small Te-Te-Te angles: 92.2° in the gold and 90.7° in the copper telluride. The Te–Te bonds are somewhat longer than single bonds (2.89 Å each in both cases). Treating this unit as a Te_3^{2-} unit, and the Te1 and Te4 atoms as Te^{2-}, one obtains 16 negative charges for the 14 Te atoms per formula unit. However, there is an additional Te–Te contact (Te1–Te2) of 3.32 Å between the Cu_3Te_3 rings, which stands against a full octet on Te1. A partial electron transfer from the $Te1^{2-}$ to the Te_3^{2-} group might be the cause for the elongated Te2–Te3, resulting in a $Te1^{(2-x)-}$ and a $Te_3^{(2+x)-}$ unit,[107] which ultimately does not change the overall electron balance, and allows for the Te1–Te2 contact.

The valence of Cu in $Na^I(Ba^{II})_6(Cu^I)_3Te_{14}$ was identified as +I, giving 16 positive (and 16 negative) charges per formula unit.[96] Assuming the same for Au in $Ba_7Au_2Te_{14}$, i.e. Au^I, in accord with the Au–Te distances, one obtains 16 positive charges as well. Again postulating Cu^I, the positive charges of $Ba_{6.76}Cu_{2.42}Te_{14}$ sum up to $6.76 \times 2 + 2.42 = 15.94$. This formalism supports the refined occupancies, yielding 2.42 Cu atoms per formula unit, hence the existence of Cu2, since both ternary tellurides exhibit 16 positive charges per formula unit, like $Na^I(Ba^{II})_6(Cu^I)_3Te_{14}$. Similarly, the K analog was reported

with K/Ba mixed occupancies combined with Cu deficiencies (but no Cu2 site) and a refined formula of $(K_{0.60}Ba_{0.40})_6Cu_{2.58}Te_{14}$, i.e. 15.98 positive charges.[96]

2.3 Electronic structure

2.3.1 Calculation method

In the LMTO approach, the following wavefunctions were used: for Ba *6s*, *5d*, *4f*, and *6p* included via the downfolding technique;[108] for Au *6s*, 6*p*, *5d* and *5f* (downfolded); for Cu *4s*, *4p*, and *3d*; and for Te *5s*, *5p*, and *5d* and *4f* (the latter two downfolded). The 252 independent *k* points of the first Brillouin zone were chosen via an improved tetrahedron method.[68] To model the electron-precise formula $Ba_7M_2Te_{14}$, all Ba sites were treated as fully occupied, the Cu2 site was ignored, and four of the six Au/Cu1 sites per unit cell were filled, resulting in the right formula, and a symmetry reduction reflected in the orthorhombic space group *Cmcm*.

The molecular orbital diagram of the V-shaped Te_3^{2-} unit of $Ba_7Au_2Te_{14}$, point group C_{2v}, was calculated using Gaussian[109] via the B3LYP method with the 3-21G basis set.[110]

2.3.2 Electronic structure calculation results

The calculated densities of states (DOS) of the models $Ba_7M_2Te_{14}$ are depicted in Figure 2.6. In both cases, a forbidden gap separates the valence band from the conduction band, with the Au telluride exhibiting the smaller gap (E_{gap} = 0.7 eV vs. 1.0 eV). Again in both cases, the top of the valence band and the bottom of the conduction band are dominated by Te *p* states. The Au *d* states predominate the area

below -4 eV at the bottom of the valence band, while the Cu *d* states mostly occur between -2 eV and -4 eV.

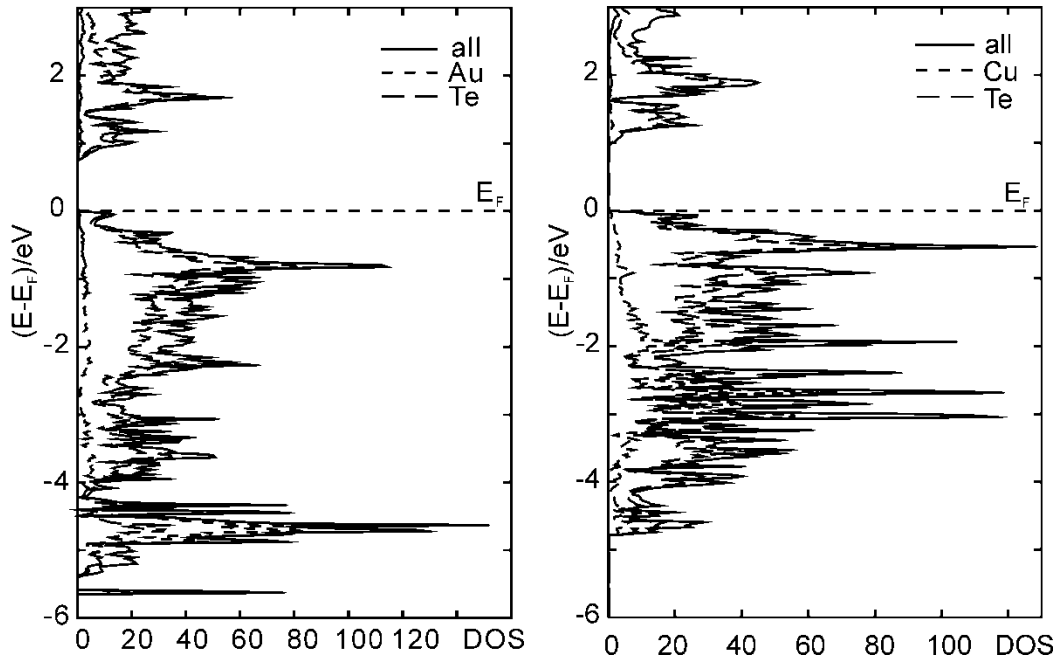

Figure 2.6. Densities of states of $Ba_7Au_2Te_{14}$ (left) and $Ba_7Cu_2Te_{14}$ (right). The Fermi level, E_F, was arbitrarily placed at 0 eV.

To gain insight into the character of the two different Te–Te contacts, the crystal orbital Hamilton population curves[61, 111] of both interactions in both structure models are compared in Figure 2.7. The curves of the two tellurides are quite similar. It is evident that the shorter bond within each compound, i.e. the one within the Te_3^{2-} group, is much stronger, for the longer ones exhibit filled antibonding states above -1 eV, where the short ones are nonbonding. Moreover, the former are anti- to nonbonding between -3.2 eV and -2 eV, and the latter bonding. The rest of the curves are comparable. The integration up to the Fermi level reveals that all four shown interactions have net bonding character, reflected in negative ICOHPs.[62] For the Au compound, these are -1.54 eV (2.89 Å) and

-0.17 eV (3.32 Å), and for the Cu compound -1.61 eV (2.88 Å) and -0.12 eV (3.32 Å). Thus, the shorter bonds appear to be stronger by factors of 9 and 13, respectively.

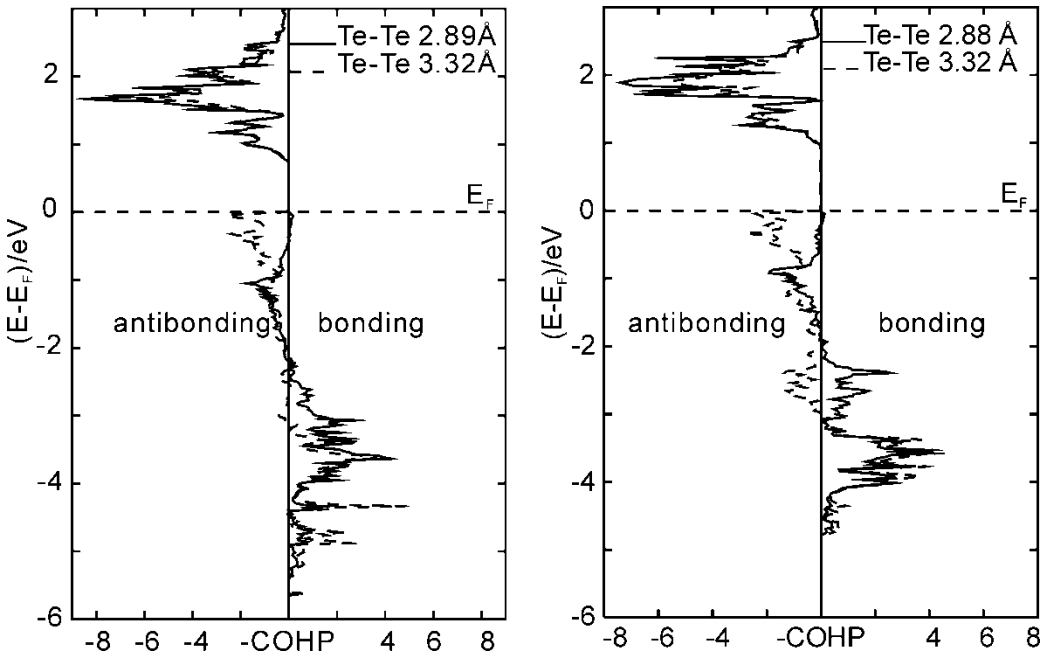

Figure 2.7. Selected crystal orbital Hamilton population curves of $Ba_7Au_2Te_{14}$ (left) and $Ba_7Cu_2Te_{14}$ (right). The Fermi level, E_F, was arbitrarily placed at 0 eV.

The molecular orbital diagram of an isolated Te_3^{2-} unit is shown in Figure 2.8., again with the *s* orbitals situated below the chosen energy window. The energies are given in hartree, E_h = 2 Ry = 27.2 eV. Therein, the bonding and antibonding π molecular orbitals are filled, yielding an only σ-bonded ion. Two σ bonds are present, reflected in filled molecular orbitals of a_1 and b_2 symmetry. Therefore, it is justified to treat this ion as a classical σ-bonded Te_3^{2-} unit. A large gap separates the HOMO from the LUMO, which is also present in the COHP curve of this Te–Te interaction in the three-dimensional crystal structure.

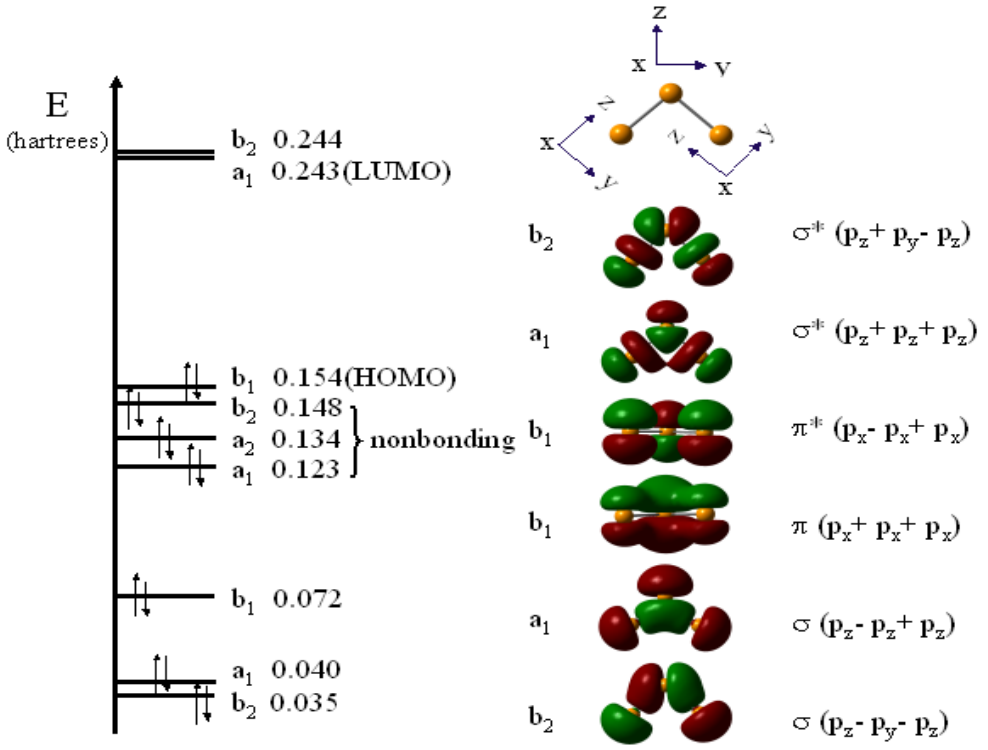

Figure 2. 8. MO diagram of the V-shaped Te_3^{2-} unit.[94]

2.4 Physical properties

The phase-pure samples were pressed into bar-shaped pellets of the dimensions 6×1×1 [in mm] for physical transport measurements, since no single crystals of sufficient dimensions were available. Seebeck coefficient (*S*) was measured under dynamic vacuum in the temperature range between 300 K and 550 K, using constantan as an internal standard to determine the temperature difference. The specific electrical conductivity, σ, was determined using a four-point-method: a homemade device was used to determine the voltage drops ΔV over distances (*L*) of approximately 2 mm at currents below 5 mA under dynamic vacuum between 320 K and 160 K. The achieved densities were between 81 % and 84 % of the theoretical maximum as determined via the

single crystal structure studies. The resistances (R) were calculated from the voltage drops using Ohm's law, i.e. $R = \Delta V/I$, with I = current. We calculated $\sigma(T)$ after measuring the lengths between the contacts, L, according to $\sigma = L/(AR)$, with the area A = 1 mm × 1 mm.

The electronic structure calculations predicted semiconducting behavior. This was confirmed by our experiments: the exponential increase of the electrical conductivity with increasing temperature, as observed for both tellurides (left part of Figure 2.9.), is typical for semiconductors. The electrical conductivity is higher in case of $Ba_7Au_2Te_{14}$, with a room temperature value of 1.6 $m\Omega^{-1}cm^{-1}$, compared to 70 $\mu\Omega^{-1}cm^{-1}$ for $Ba_{6.76}Cu_{2.42}Te_{14}$. Because of the strong temperature dependence combined with the low conductivity at room temperature, the current and hence the conductivity of the Cu sample could not be determined below 255 K. The lower values of $Ba_{6.76}Cu_{2.42}Te_{14}$ were expected based on the smaller band gap of the Au material. For comparison, the room temperature values of $Na^{I}(Ba^{II})_6(Cu^{I})_3Te_{14}$ and $(K_{0.60}Ba_{0.40})_6Cu_{2.58}Te_{14}$ were reported to be 100 $m\Omega^{-1}cm^{-1}$ and 10 $\mu\Omega^{-1}cm^{-1}$, respectively, measured on single crystals. Advanced thermoelectrics typically exhibit an electrical conductivity above 1000 $\Omega^{-1}cm^{-1}$.[25]

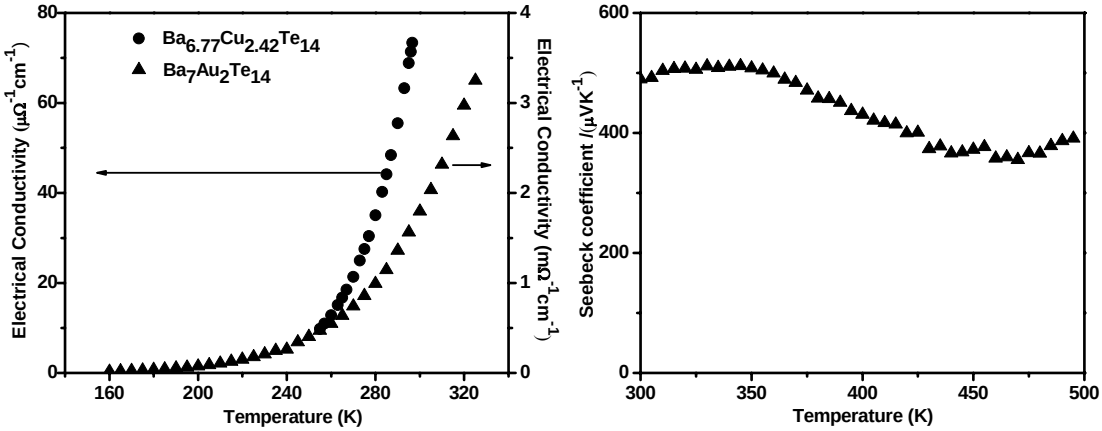

Figure 2.9. Electrical conductivity (left) of $Ba_7Au_2Te_{14}$ and $Ba_{6.76}Cu_{2.42}Te_{14}$ and Seebeck coefficient measurements of $Ba_7Au_2Te_{14}$ (right).

For intrinsic semiconductors, Arrhenius' law for thermally activated conduction applies: $\ln\sigma/\sigma_0 = \exp(-\Delta_A/k_BT)$, with Δ_A = activation energy = ½ E_{gap}.[112] Then, plotting $\ln\sigma$ vs. $1/T$ results in a linear curve with a slope of $-½\ E_{gap}/k_B$. In case of the Cu sample, such a linear curve was obtained over the whole temperature range, i.e. above 255 K, with a regression coefficient of $R^2 = 0.9999$, and $E_{gap} = 0.6$ eV. In case of the Au sample, where the conductivity was measured down to 160 K, a significant deviation from linearity was noticed, expressed in the low $R^2 = 0.982$. This is likely a consequence of extrinsic charge carriers that cause a smaller slope at low temperatures.[9] Linearity was observed above 255 K, comparable to the slope of the Cu conductivity, with $R^2 = 0.9988$, and E_{gap} = 0.4 eV, which is evidently smaller than the 0.6 eV of the Cu compound. These results qualitatively confirm the trend of the gaps as calculated with the LMTO approach, i.e. that the gap is smaller in case of the Au compound (calculated to be 0.7 eV, compared to 1.0 eV for the Cu compound).

Because of the small electrical conductivity of $Ba_{6.76}Cu_{2.42}Te_{14}$, its Seebeck coefficient could not be determined. The Seebeck coefficient for $Ba_7Au_2Te_{14}$ at 300 K is

around +490 μV/K, and decreases to +355 μV/K at 470 K (right part of Figure 2.9.). The charge carriers of $Na^{I}(Ba^{II})_6(Cu^{I})_3Te_{14}$ were predominantly *p*-type as well, with a Seebeck coefficient of +100 μV/K.

2.5 Conclusion

Two new tellurides, $Ba_7Au_2Te_{14}$ and $Ba_{6.76}Cu_{2.42}Te_{14}$, were synthesized and structurally characterized. Both are variants of the $NaBa_6Cu_3Te_{14}$ type, where an additional site is occupied by Cu2 in case of $Ba_{6.76}Cu_{2.42}Te_{14}$. The Cu delocalization is restricted to occur within the Cu_3Te_3 rings only, i.e. no Cu ion conductivity may be observed. Since the monovalent Na cation is replaced by the divalent Ba cation, the Au/Cu position exhibits deficiencies in both ternary compounds, with occupancies of 66.5(3) % Au and 61.7(8) % Cu on Cu1 and 9.5(7) % Cu on Cu2. In accord with the Cu content being higher than the Au content, there are deficiencies on one Ba site (Ba2) in case of the ternary copper compound, which are also required because of the short Ba2–Cu2 distance. Assuming Na, Cu, and Au in the +I state, there are 16 positive charges in all cases, within the standard deviations ($Ba_7Au_{1.995(9)}Te_{14}$: 15.995(9); $Ba_{6.76(1)}Cu_{2.42(7)}Te_{14}$: 15.9(1)), equalizing the 16 negative charges of the 14 Te sites, considered as five Te^{2-} and three Te_3^{2-} units.

Both materials are semiconductors, with calculated gaps of 0.7 eV and 1.0 eV. These gaps are larger than ideal for the thermoelectric energy conversion, which is reflected in a low electrical conductivity of both materials.

Chapter 3 Two Different Structures within the Quaternary Tellurides $Ba_4M_{4-x}A_2Te_9$ (M=Cu, Ag or Au and A= Si or Ge) and Their Transport Properties

Transition metal chalcogenides have been investigated for a long time due to their structural diversity and various technical applications. Examples include: layered compounds R_6ZTe_2 (R = Y, Z = Rh, Pd, Y, Ag or R = Lu, and Z = Ag, Cu),[113] $Ni_3Cr_2P_2Q_9$ (Q = S, Se)[114]; and three-dimensional $Ag_2Nb[P_2S_6][S_2]$, $KAg_2[PS_4]$,[115] $AgPb_mSbTe_{2+m}$[25] and spinel-type ACr_2X_4 (A = Mn, Fe, Co, Cu, Zn, Cd; X = O, S, Se).[116] These compounds may exhibit interesting magnetic, optical or thermoelectric properties.

We have been exploring the structures and properties of a number of ternary and quaternary Cu/Ag/Au chalcogenides, for example: $Ba_3Cu_{14}Te_{12}$,[81] $Ba_7M_2Te_{14}$,[117] BaM_2Te_2 [118] (M = Cu, Ag, Au), BaM_2SnSe_4 (M = Cu, Ag) and $Ba_3Cu_2Sn_3Se_{10}$,[83] with various bonding M–M interactions and band gaps ranging from 0.1 eV to 1.2 eV. Recently we reported our first barium copper/silver germanium tellurides $Ba_4M_4Ge_2Te_9$ (M = Cu, Ag).[119] These are the first members of the barium coinage metal germanium tellurides system, while a few Ba-Cu/Ag-Ge sulfides and selenides were reported, such as the sulfides $BaCu_2GeS_4$,[120] $BaAg_2GeS_4$,[121] and $BaCu_6Ge_2S_8$[122] as well as the selenides $BaCu_2GeSe_4$ and $BaAg_2GeSe_4$.[123] In contrast to the common oxidation states occurring in the sulfides and selenides, namely Ba^{2+}, Cu^{+}, Ag^{+}, Ge^{IV}, S^{2-} and Se^{2-}, and the almost

exclusively tetrahedral coordination of the cations, the new tellurides exhibit four- and five-fold coordinated M atoms as well as low-valence Ge. Then further work was extended in this system, with Au and Si involved. We obtained a new, more complex structure type to the telluride system that may be viewed as a super cell variant, adopted by $Ba_4Cu_{3.76}Si_2Te_9$ and $Ba_4Au_{3.69}Ge_2Te_9$, as well as a new member of the $Ba_4Ag_{3.95}Ge_2Te_9$ type, namely $Ba_4Ag_{3.97}Si_2Te_9$.[124]

3.1 Synthesis and analysis

All these tellurides were prepared by heating the elements obtained with purities of at least 99 %: barium granules, 99 %, Aldrich; gold powder, spherical -200 mesh, 99.9 %, Alfa Aesar; silver powder -22 mesh, 99.9995 %, Alfa Aesar; copper powder -625 mesh, 99.9 %, Alfa Aesar; germanium powder -100 mesh, 99.99 %, Aldrich; silicon powder crystalline -100 mesh, 99.9 %, Alfa Aesar , and tellurium powder, -200 mesh, 99.9 %, Alfa Aesar; and stored in an argon filled glove box. In the glove box, the starting materials, Ba, Ag, Ge and Te, were loaded in the molar ratio of 4 : 4 : 2 : 9 into a fused silica tube then sealed. The reaction mixture was heated to 750 °C within 48 hours in a resistance furnace, kept at that temperature for two hours, and then cooled to 200 °C at a rate of 3 °C per hour, followed by switching off the furnace. An X-ray powder diffractogram obtained from the ground sample showed that no known materials were present, indicating the formation of at least one new material. Single crystal structure determination gives the formula of $Ba_4Ag_{3.95}Ge_2Te_9$.

The other tellurides were prepared using the same temperature profile, but a subsequent single crystal structure study revealed a significant deviation from the

4 : 4 : 2 : 9 ratio of the elements, namely a Cu, Ag or Au deficiency, with the refined formula being $Ba_4Cu_{3.71}Ge_2Te_9$, $Ba_4Cu_{3.75}Si_2Te_9$, $Ba_4Ag_{3.97}Si_2Te_9$ and $Ba_4Au_{3.69}Ge_2Te_9$.

The bulk samples for transport property measurements were prepared according to the refined single crystal composition using the same temperature profile. The crystal compositions were supported by the Energy dispersive X-ray analysis (EDAX) on selected crystals, using the electron microscope LEO 1530 with an additional EDAX device, EDAX Pegasus 1200.

To check for possible phase transitions, temperature dependent combined differential scanning calorimetry (DSC) and thermogravimetry (TG) measurements were performed on the bulk samples of $Ba_4Ag_{3.95}Ge_2Te_9$ and $Ba_4Au_{3.69}Ge_2Te_9$ with the computer controlled NETZSCH STA 409PC Luxx. The measurements were carried out with a heating rate of 10 K/min under a constant flow of Argon (40 ml/min), which also protected the balance (flow of 30 ml/min). One prominent peak in the DSC of $Ba_4Ag_{3.95}Ge_2Te_9$ indicates its melting point to be at 1000 K, while the DSC of $Ba_4Au_{3.69}Ge_2Te_9$ exhibits two peaks, one at 690 K, and the other at 870 K. The 690 K peak is most likely caused by a (solid-solid) phase transition, and the 870 K peak corresponds to the melting point.

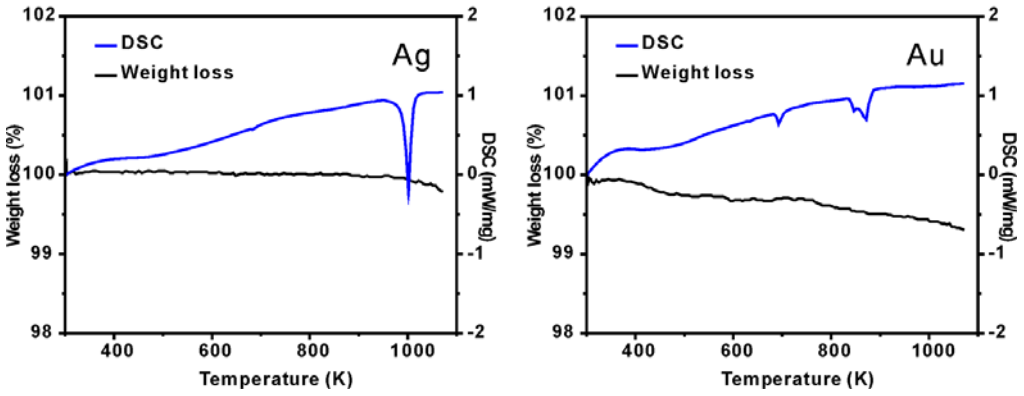

Figure 3.1. DSC/TG curves of $Ba_4Ag_{3.95}Ge_2Te_9$ (left) and $Ba_4Au_{3.69}Ge_2Te_9$ (right).

3.2 Crystal structure

3.2.1 Crystal structure determinations

Single crystal data collections were carried out on a Smart Apex CCD (BRUKER) equipped with an area detector utilizing graphite-monochromatic Mo-$K\alpha$. Data were collected by scans of 0.3 ° in ω at different φ angles, for an overall of 2 × 606 frames with exposure times of 30 seconds each. The data were corrected for Lorentz and polarization effects. Absorption corrections were based on fitting a function to the empirical transmission surface as sampled by multiple measurements of numerous symmetry equivalent reflections.[95] Structure solution and refinements were performed with the SHELXTL package.[54]

The structure solution via direct methods led to the identification of eight sites for the Ag-Ge case, occupied by one Ba, two Ag, one Ge and four Te atoms. The refinements of this model resulted in $R1 = 0.0166$ and $wR2 = 0.0349$ (observed data) with every site fully occupied. Since the displacement factor of Ag1 was 8 % higher than that of Ag2, the occupancy of Ag1 was refined, revealing a small though significant deficiency of 2.7(2) %. This occurred with significantly[125] improved residual values, $R1 = 0.0154$ and $wR2 = 0.0327$. To further investigate the Ag1 deficiency, a second crystal was selected from another sample starting from 4Ba : 4Ag : 2Ge : 9Te. The refinement results are highly consistent, with an Ag1 deficiency of 2.3(2) % and residual values of $R1 = 0.0217$ and $wR2 = 0.0298$. Finally, the atomic positions were standardized with the TIDY program within the PLATON package.[126]

To check for the phase range, another crystal was analyzed from a new Ag deficient sample of nominal formula "$Ba_4Ag_{3.1}Ge_2Te_9$", resulting in a slightly higher Ag

deficiency as expressed in the refined formula $Ba_4Ag_{3.902(6)}Ge_2Te_9$. Hence a small phase range may be formulated for $Ba_4Ag_{4-x}Ge_2Te_9$ with $0.05 < x < 0.10$.

The structure solution of the Cu-Ge compound initially yielded an isostructural model. For ease of comparison, the Ag-Ge solution with all positions fully occupied was used in the subsequent refinement steps. This resulted in rather high *R* values: *R*1 = 0.0701 and *wR*2 = 0.1639 (observed reflections). Due to the conspicuously high displacement factors, U_{eq}, of Cu1 : 0.54(3) Å^2, Cu2 : 0.0494(11) Å^2, Te3 : 0.0303(4) Å^2, and Te4 : 0.0448(9) Å^2 combined with large anisotropies, these atoms were refined as split sites (e.g., Cu1 and Cu1A) one by one. More uniform U_{eq} values and gradually improving *R* values were obtained, and the occupancies of the Cu1 atoms were refined as well, giving *R*1 = 0.0299 and *wR*2 = 0.0706. Thereby Te4 moved from the 2*a* site to 4*g*, i.e. from point group 2/*m* to *m*. Because the resulting Fourier map contained an additional electron density peak close to Cu1A, another split site, Cu1B, was introduced. This led to a featureless electron density map and significantly lower residual values of *R*1 = 0.0218 and *wR*2 = 0.0466. These improvements were all significant on the 0.005 confidence level of the Hamilton test.[125] The occupancies of Cu1, Cu1A and Cu1B were refined to 45 %, 22 % and 25 %, respectively, and the occupancies of Cu2 and Cu2A to 89 % and 12 %, and of Te3 and Te3A to 87 % and 13 %, respectively. The refined formula is thus $Ba_4Cu_{3.71(2)}Ge_2Te_9$.

To find the lower limit of the Cu occupancy, a second crystal was analyzed from a more Cu deficient starting composition, namely 4Ba : 3.1Cu : 2Ge : 9Te. The refinement yielded the same split sites and formula within standard deviation, namely

$Ba_4Cu_{3.70(1)}Ge_2Te_9$ with $R1$ = 0.0294 and $wR2$ = 0.0564, so that the phase range was concluded to be minimal.

No super cell reflections were observed in case of the Ag-Si telluride. Taking the solution of the Ag-Ge telluride in *Pbam*, the refinement yields the final formula of $Ba_4Ag_{3.968(4)}Si_2Te_9$ with observed reflections R values of $R1$ = 0.0166 and $wR2$ = 0.0332. Like in the case of the Ag-Ge telluride, no split sites were evident. Detailed crystal structure information is listed in Appendix A: Table A.3.1. and Table A.3.2.

In case of the Au-Ge telluride, the occurrence of super cell reflections caused a doubling of the c axis of $Ba_4Ag_{3.95}Ge_2Te_9$. The systematic absences pointed to space group *Pnma*. The direct methods yielded twelve atomic positions that were successfully identified as two Ba, three Au, one Ge and six Te atoms. The refinements of this model resulted in $R1$ = 0.0477 and $wR2$ = 0.1164 (observed data) with every site fully occupied. Because the Fourier map contained two additional electron density peaks with the density of 10.04 e/Å^3 (in a distance of 0.82 Å to Au2) and 7.48 e/Å^3 (2.07 Å to Au1), in addition to the high displacement factors, U_{eq}, of Au1: 0.0301(2) Å^2, Au2: 0.0370(2) Å^2, and Au3: 0.0347(2) Å^2, respectively; two split sites, Au2A and Au1A, were introduced one by one. The occupancies were also refined: Au1 and Au1A to 86 %, and 3.8 %, Au2 and Au2A to 87 % and 8.1 %, and Au3 to 89%, respectively. This led to a featureless electron density map and lower displacement factors, U_{eq}, of Au1: 0.0250(2) Å^2, Au2: 0.0315(2) Å^2, and Au3: 0.0308(2) Å^2. The refined formula is then $Ba_4Au_{3.69(1)}Ge_2Te_9$ with the $R1$ = 0.0294 and $wR2$ = 0.0673 for observed data.

The unit cell parameters and the systematic absences in case of the Cu-Si telluride indicated that this telluride is isostructural with $Ba_4Au_{3.69}Ge_2Te_9$. Correspondingly, the

direct methods yielded an equivalent model. To ease comparison, we then used the refined positional parameters of the gold compound as the starting model for refinements, excluding the split sites. The resulting residual values were $R1 = 0.0305$ and $wR2 = 0.0622$. Due to the enlarged displacement factors, U_{eq}, of Cu1: 0.0394(4) Å^2, Cu2: 0.0307(2) Å^2, and Cu3: 0.0656(4) Å^2, we allowed the occupancy factors of the Cu sites to be freely refined. This resulted in occupancy factors of 90 %, 97 % and 91 %, for Cu1, Cu2, and Cu3, which lowered U_{eq} of Cu1, Cu2 and Cu3 to 0.0331(5) Å^2, 0.0291(3) Å^2, and 0.0581(8) Å^2, respectively, and gave lower R values as well, namely $R1 = 0.0294$ and $wR2 = 0.0583$. The refined formula is then $Ba_4Cu_{3.75(2)}Si_2Te_9$.

These two structures may be viewed as a super cell of the previously reported *Pbam* structure. To justify the structure refinements, the structures were refined both in the *Pbam* and *Pnma* space group. For example, in case of the new telluride $Ba_4Cu_{3.75}Si_2Te_9$, the Cu1 site had to be refined as a split site and Cu2 exhibited large U_{eq} values in the *Pbam* model (sub cell), while they occur as Cu1, Cu2 and Cu3 in the *Pnma* model (super cell) without evident split sites.

In contrast to $Ba_4Cu_{3.75(2)}Si_2Te_9$, the split sites of the previously reported $Ba_4Cu_{3.71(2)}Ge_2Te_9$ (*Pbam*) did not disappear when refining the structure in *Pnma*. Moreover, no super cell reflections were visible. Therefore, it is concluded that $Ba_4Cu_{3.71(2)}Ge_2Te_9$ does indeed crystallize in the *Pbam* space group.

So far, five tellurides were found to adopt one of the two variants, *Pbam* or *Pnma*: the Cu-Ge, Ag-Si, and Ag-Ge tellurides crystallize in the *Pbam* space group, and the Cu-Si and Au-Ge tellurides occur in the *Pnma* space group. The efforts to synthesize the analogous Au-Si telluride failed. Since the previous study on $Ba_4Cu_{4-x}Ge_2Te_9$ on Ba_4Ag_{4-}

$_x$$Ge_2Te_9$ pointed to the existence of only a very small, likely negligible phase range, we forwent such an investigation for the new members. Crystallographic data of the two super cells are listed in Appendix A: Table A.3.4. and Table A.3.5.

Further details of the crystal structure investigations can be obtained from the Fachinformationszentrum Karlsruhe, 76344 Eggenstein-Leopoldshafen, Germany (fax: (49) 7247-808-666; e-mail: crysdata@fiz-karlsruhe.de) on quoting the depository nos. CSD-421080 ($Ba_4Cu_{3.75}Si_2Te_9$), 421078 ($Ba_4Ag_{3.97}Si_2Te_9$), and 421079 ($Ba_4Au_{3.69}Ge_2Te_9$).

3.2.2 **Crystal structure of $Ba_4M_4A_2Te_9$ sub cell**

These three new quaternary tellurides, $Ba_4Ag_{3.95}Ge_2Te_9$, $Ba_4Cu_{3.71}Ge_2Te_9$ and $Ba_4Ag_{3.97}Si_2Te_9$, crystallize in their own new three-dimensional structure type, as shown in Figure 3.2. for $Ba_4Ag_{3.95}Ge_2Te_9$, wherein the Ba–Te bonds are omitted for clarity. The Ba atoms are surrounded by eight Te atoms in a bi-capped trigonal prism, with distances in the range of 3.49 Å – 3.77 Å for $Ba_4Ag_{3.95}Ge_2Te_9$ and $Ba_4Ag_{3.97}Si_2Te_9$, and 3.42 Å – 3.69 Å for $Ba_4Cu_{3.71}Ge_2Te_9$. These distances are comparable to the Ba–Te bonds of the ninefold coordinated Ba atoms in $BaSbTe_3$ (3.41 Å – 3.89 Å)[97], Ba_2SnTe_5 (3.44 Å – 3.84 Å),[98] and $Ba_3Cu_{14}Te_{12}$ (3.47 Å – 3.84 Å).[81]

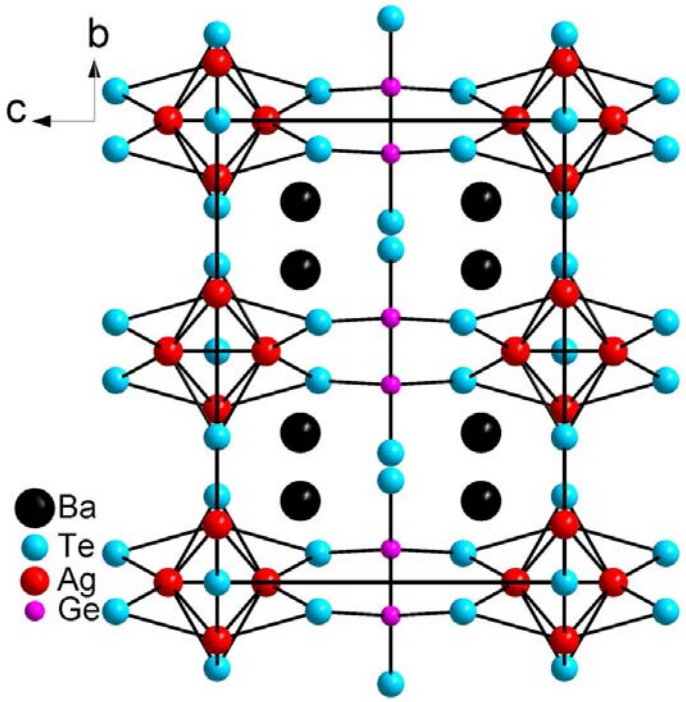

Figure 3.2. Crystal structure of $Ba_4Ag_4Ge_2Te_9$.

The structure motifs include $BaTe_8$ bi-capped trigonal prisms, $AgTe_4$ tetrahedra, $AgTe_5$ square pyramids and dimeric Ge_2Te_6 units. The Ag1 atoms are surrounded by five Te atoms to form a square pyramid with the Ag–Te distances ranging from 2.84 Å to 3.11 Å for $Ba_4Ag_{3.95}Ge_2Te_9$ (Figure 3.3.) and 2.82 Å to 3.16 Å for $Ba_4Ag_{3.97}Si_2Te_9$. The corresponding Cu atom splits into three sites Cu1, Cu1A and Cu1B with occupancies of 44.7 %, 21.9 % and 24.7 %, respectively. The short distances (0.60 Å – 2.16 Å) between these three atoms necessitate that they are never occupied at the same location within a given crystal; this concurs well with the combined occupancies being below 100 % (overall occupancy 91.3 %). Such a scenario is common in copper chalcogenides, e.g. in $LnCu_{0.3\text{-}0.4}Te_2$,[102] $Gd_3Cu_2Te_7$,[103] $Cu_{2-\delta}Se$,[104] $CuSm_3Se_6$,[105] and $Cu_4Bi_4Se_9$.[106]

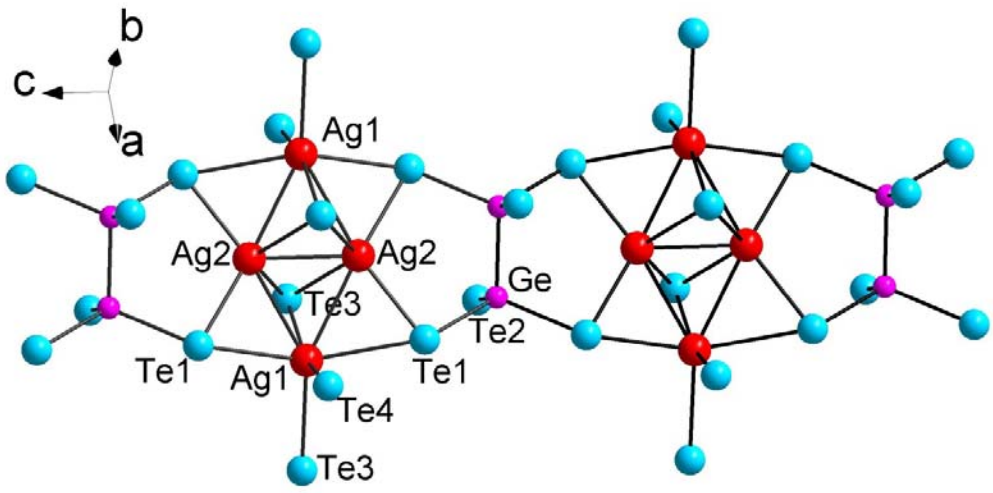

Figure 3.3. Fragment of the covalent framework of $Ba_4Ag_4Ge_2Te_9$ comprising Ag_4 clusters and Ge_2Te_6 units.

The tetrahedrally coordinated Ag2/Cu2 atoms connect with two Te1 and two Te3 atoms at distances of 2.80 Å and 3.00 Å for Ag2, and 2.66 Å and 2.82 Å for Cu2. Two $Ag1Te_5$ square pyramids and two $Ag2Te_4$ tetrahedra are interconnected to each other by edge-sharing, forming a planar Ag_4 cluster with Ag–Ag distances of 2.89 Å (Ag2–Ag2) and 3.04 Å (Ag1–Ag2). The Ag_4Te_{10} units are connected through dimeric Ge_2Te_6 units to a complex one-dimensional chain running along the *c* axis.

It is noted that the Ag1–Ag2 bond is longer than Ag2–Ag2, while the Cu1–Cu2 bond of $Ba_4Cu_{3.71}Ge_2Te_9$ (2.47 Å) is shorter than Cu2–Cu2 (2.76 Å). Another important difference between the Cu and Ag tellurides is the long Cu1–Te3 distance > 4 Å compared to the Ag1–Te3 distance of 3.03 Å. Therefore, both Cu sites, Cu1 and Cu2, are coordinated by four Te atoms (left part of Figure 3.4.).

Furthermore, the Cu split sites cause the occurrence of other Cu clusters as well. For example, one Cu2A atom replaces two Cu2 atoms, for it is located in the center of the original Cu2 dumbbell, thus forming a linear Cu_3 unit in lieu of the Cu_4 cluster (center

part of Figure 3.4.). Thus, the Cu telluride formally forms a structure type different to that of the Ag telluride because of the additional Wyckoff position, 2*c*, being filled by Cu2A (and because of the Te4 site as discussed below). Cu2A can only be surrounded by Cu1A, because the distance to Cu1 (2.04 Å) and Cu1B (2.29 Å) are both too short. Moreover, the Cu2A atom moves one Te3 atom into its Te3A split site, as the Cu2A–Te3 distance of 2.46 Å is also too short. This observation is validated by the approximately equal occupancies of 12 % – 13 % for Cu2A and Te3A. Another variant of the Cu_4 cluster is represented in the right part of Figure 3.4., consisting of two Cu1B and two Cu2 atoms with Cu1B–Cu2 distances of 2.68 Å. Despite the deficiencies and split sites, the Cu ions may not move through the crystals, for the clusters are surrounded by the Ge_2Te_6 units that block the path for the Cu ions. This constitutes a strong contrast to the Cu ion conducting selenide-telluride, $Ba_3Cu_{17-x}(Se,Te)_{11}$.[127]

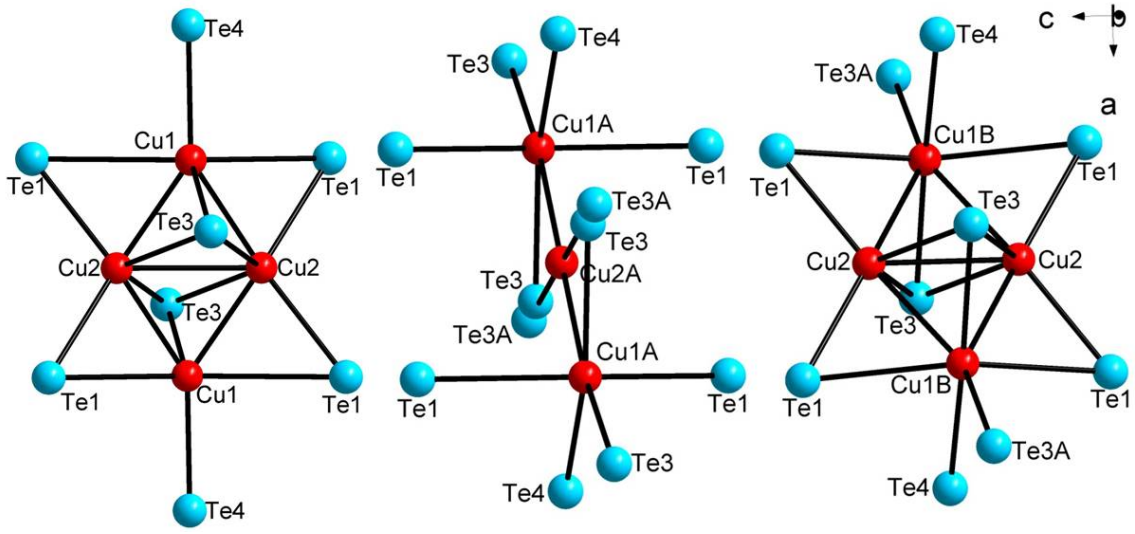

Figure 3.4. Split site variants of the Cu clusters with surrounding Te atoms of $Ba_4Cu_{3.71}Ge_2Te_9$.

A detailed examination of the interatomic distances (Table A.3.3.) also reveals different Te coordination for the various split sites of the main atoms Cu1 and Cu2,

which are both fourfold coordinated by Te atoms. Cu1A is fivefold coordinated, like Ag1, namely by two Te1 atoms at a distance of 3.04 Å, by one Te3 (2.94 Å), and either by a second Te3 (2.77 Å) or Te3A (3.24 Å), and by one Te4 at either 2.76 Å or 3.18 Å. The case of Cu1B is similar, but two of these five distances may be quite long with 3.26 Å and 3.53 Å, depending on whether the Te3 or the Te3A site is filled. Cu2A stands out, because it is coordinated by two Te3 atoms at a distance of 3.14 Å, and even longer distances of 3.61 Å to four Te1 atoms complete its coordination sphere.

One Ge–Ge or Si-Si bond occurs in the A_2Te_6 unit, indicating tri-valent Ge/Si, as reported in, e.g., $K_6(Ge^{III})_2Te_6$[128] and $Na_6Si_2Te_6$[129]. The Ge–Ge bond distances in Ag and Cu compound are 2.43 Å and 2.41 Å, respectively, comparable with 2.45 Å and 2.46 Å in $Tl_6(Ge^{III})_2Te_6$,[130] 2.49 Å in $K_6(Ge^{III})_2Te_6$, and 2.47 Å in $Ba_2(Ge^{III})_2Te_5$.[98] The Si–Si bond distance is 2.33 Å for the Ag-Si telluride, which is typical single bond, as found in $Na_6Si_2Te_6$ (2.35 Å)[129] and $Na_4Si_2Te_5$ (2.37 Å),[131]. The Ge/Si–Te bonds between 2.55 Å and 2.59 Å for the Ag-Ge compound, 2.48 Å and 2.51 Å for the Ag-Si compound, and 2.57 Å and 2.59 Å for the Cu-Ge compound are inconspicuous as well. The linear chains that are composed of Ag_4Te_{10} and Ge_2Te_6 units are further connected by Te3 and Te4 atoms in the *ab* plane to a three-dimensional network, which incorporates the eight-coordinated Ba atoms (Figure 3.5.).

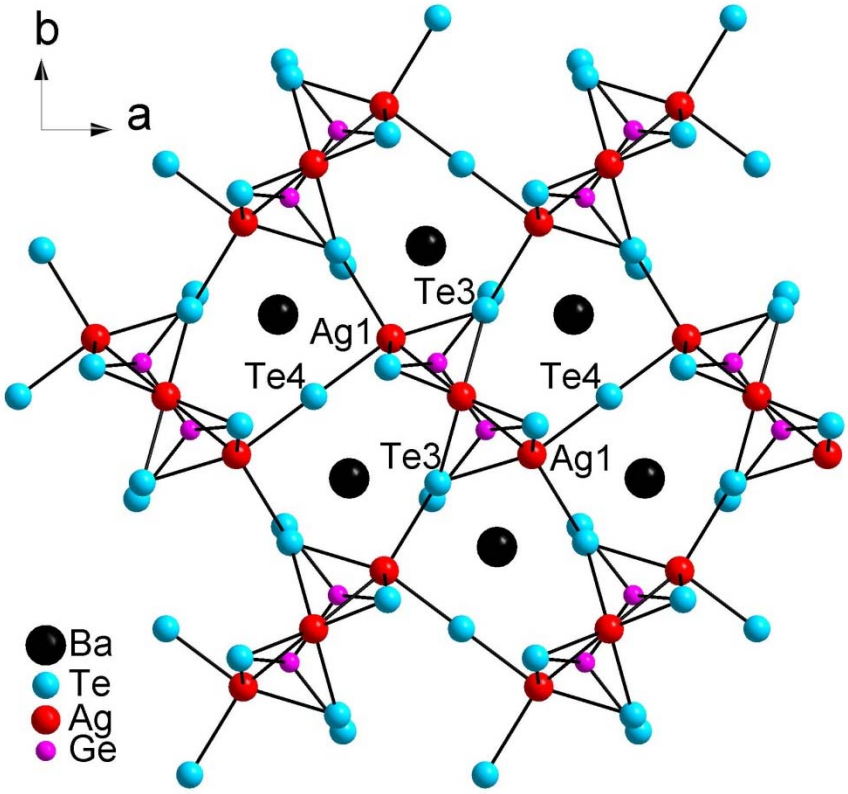

Figure 3.5. A larger view of the covalent framework of $Ba_4Ag_4Ge_2Te_9$ encompassing the Ba atoms.

The assignment of formal charges is straightforward: since there are no Te–Te contacts < 3.57 Å, the Te atoms are viewed as Te^{2-}, and with Ge/Si ^{III} as discussed, the other elements are in their most common oxidation states, namely Ba^{2+} and Ag^{+}/Cu^{+}, according to $(Ba^{2+})_4(Ag^{+})_4(Ge^{III})_2(Te^{2-})_9$. The observation of Ag^{+} and Cu^{+} is typical in such chalcogenides, as is the occurrence of the Ag–Ag/Cu–Cu bonds.[81, 83, 117, 118, 127, 132, 133] These possibly closed-shell (d^{10}–d^{10}) interactions, depending on the exact electron count, may be understood based on the hybridization of the filled *d* states with the nominally empty, energetically higher lying *s* and *p* orbitals.[134-136]

3.2.3 **Crystal structure of $Ba_4M_4A_2Te_9$ super cell**

$Ba_4Cu_{3.75}Si_2Te_9$ and $Ba_4Au_{3.69}Ge_2Te_9$ (*Pnma*) crystallizes in a super cell variant of $Ba_4Cu_{3.71}Ge_2Te_9$ (*Pbam*). To keep the standard setting of the respective space groups, the axes had to be relabeled: $a_{super} = b_{sub}$; $b_{super} = 2 \times c_{sub}$; $c_{super} = a_{sub}$. The super cell for $Ba_4Cu_{3.75}Si_2Te_9$ is shown in Figure 3.6., wherein Ba–Te bonds are omitted for clarity. The phase transformation of $Ba_4Au_{3.69}Ge_2Te_9$ upon heating to 690 K detected via DSC is most likely the transformation from the super cell to the sub cell. In these two cases, the Ba atoms are also surrounded by eight Te atoms, with distances in the range of 3.50 Å – 3.68 Å for $Ba_4Cu_{3.75}Si_2Te_9$, and 3.50 Å – 3.81 Å for $Ba_4Au_{3.69}Ge_2Te_9$ (Table A.3.6.). These distances are also comparable to the Ba–Te bonds in other Ba tellurides, as we mentioned before.

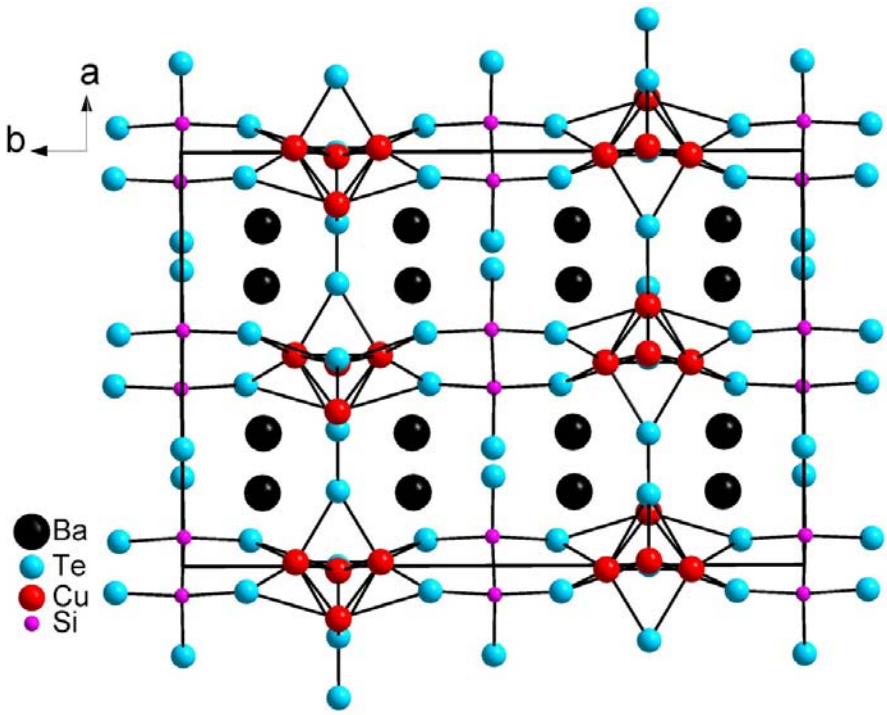

Figure 3.6. Crystal structure of $Ba_4Cu_4Si_2Te_9$.

The most apparent difference between these two structures is the orientation of the M_4 clusters, while the Te atom sublattice remains topologically equivalent. In the $Ba_4Ag_{3.97}Si_2Te_9$ (*Pbam*) structure, the M1 atoms are surrounded by five Te atoms to form a square pyramid. In the *Pnma* structure adopted by $Ba_4Cu_{3.75}Si_2Te_9$ and $Ba_4Au_{3.69}Ge_2Te_9$, the corresponding M1 site orders into two independent sites, M1 and M3, bonded to four and five Te atoms, respectively: the apparent shift of the M1 atom occurs with a significant elongation of the Cu1–Te3 distance to 3.71 Å and the Au1–Te3 distance to 4.21 Å, while M3 remains fivefold coordinated with Cu3–Te distances between 2.66 Å and 3.10 Å and Au3–Te distances between 2.77 Å and 3.22 Å (Figure 3.7.). Furthermore, the four equivalent M1–M2 distances per M_4 cluster in *Pbam* split into two short and two long contacts (M1–M2 and M3–M2), e.g. 2× 2.55 Å and 2× 2.97 Å in $Ba_4Cu_{3.75}Si_2Te_9$ (*Pnma*), compared to 4× 3.03 Å in $Ba_4Ag_{3.97}Si_2Te_9$ (*Pbam*).

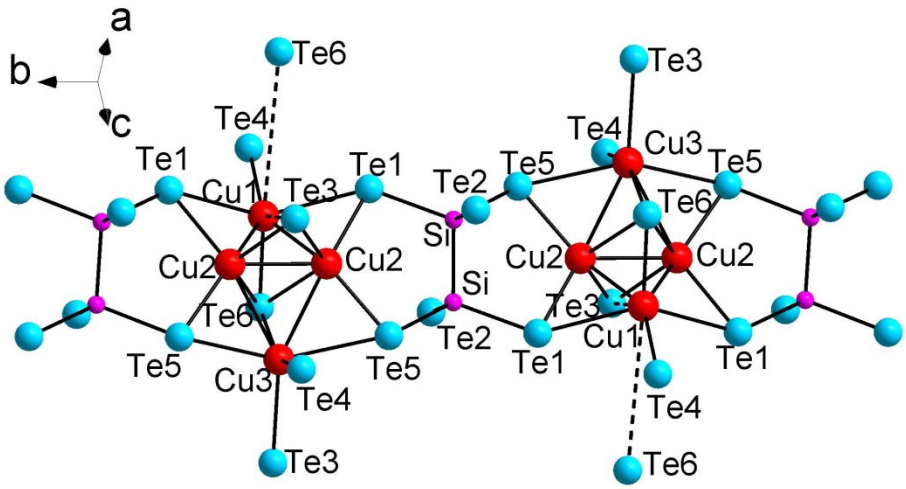

Figure 3.7. Fragment of the covalent framework of $Ba_4Cu_4Si_2Te_9$ comprising Cu_4 clusters and Si_2Te_6 units, dashed lines are not real bonds.

Moreover, the Te3 sites of $Ba_4Ag_{3.95}Ge_2Te_9$, capping triangular faces of the Ag_4 cluster, split into a Te3 and Te6 site in $Ba_4Cu_{3.75}Si_2Te_9$. Te6 then bonds to all four M

atoms of one M_4 cluster (2.57 Å – 2.87 Å in the Cu-Si telluride and 2.67 Å – 3.46 Å in the Au-Ge telluride) in contrast to the threefold coordinated Te3 atoms. (The Te6 atom at the bottom of the Cu_4 unit exhibits a long distance of 4.93 Å to the Cu1 atom and 4.79 Å to the Au1 atom of the M_4 cluster, while its four bond to the next Cu_4 cluster are not within the section shown in Figure 3.7.)

In both structure types, the M2 atoms are tetrahedrally coordinated, noting that the Au telluride stands out with its split sites and [3+1] coordination for the major Au2 site (89% occupancy). This Au2 site has three short bonds of 2.78 Å – 2.89 Å and a longer distance of 3.46 Å to Te6. The Au1 and Au2 atoms are each split into two sites, named Au1, Au1A, Au2 and Au2A, with occupancies of 86%, 4%, 89%, and 9%, respectively. Due to the short distances between Au1 and Au1A (2.09 Å) and between Au2 and Au2A (0.60 Å), these split sites are never present at the same location within a given crystal; moreover, the Au1–Au2A distance of 2.57 Å is somewhat short as well, considering Pauling's single bond radius of r_{Au} = 1.34 Å.[137] The above concurs well with the combined occupancies being below 100% (overall occupancy 90% for the Au1 site and 97% for the Au2 site). As the Au1A atom is reminiscent of the Ag1 position in $Ba_4Ag_{3.95}Ge_2Te_9$, one may postulate that its presence is a result of an incomplete *Pbam* to *Pnma* transition upon cooling in the furnace.

Another motif in these structures is the Si_2Te_6/Ge_2Te_6 unit, wherein a single bond between two Si/Ge atoms points towards trivalent Si/Ge. The Si–Si bond distances are 2.31 Å for the Cu-Si telluride, and the Ge–Ge bond distance is 2.43 Å for the Au-Ge telluride. The Si–Te bonds of 2.49 Å to 2.52 Å and the Ge–Te bonds of 2.57 Å to 2.59 Å are also comparable to literature values. With the assumption of A^{III}, the assignment of

the valence-electrons is self-evident: $(Ba^{2+})_4(M^{+})_4(A^{III})_2(Te^{2-})_9$, as in the sub cell silver and copper germanium tellurides.[119]

The Cu_4Te_9 units, composed of two $M2Te_4$, one $M1Te_4$, and one $M3Te_5$ motifs, are connected through dimeric A_2Te_6 units into a complex one-dimensional chain running along the *b* axis. These chains are further connected by the Te3 (but not Te6) and Te4 atoms forming a one dimensional channel running along the *b* axis with Ba atoms situated in, as shown in Figure 3.8.

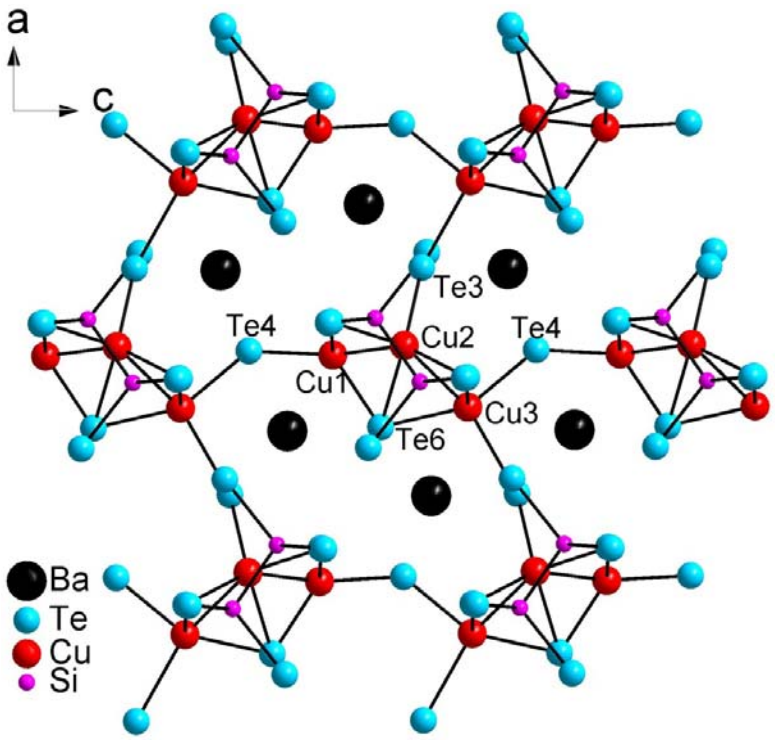

Figure 3.8. A larger view of the covalent framework of $Ba_4Cu_4Si_2Te_9$ encompassing the Ba atoms

3.3 Electronic structure

3.3.1 Calculation method

We utilized the self-consistent tight-binding *first principles* LMTO method (LMTO = linear muffin tin orbitals), with the atomic spheres approximation (ASA)[65, 66] for the electronic structures calculation. In the LMTO approach, the density functional theory is employed utilizing the local density approximation (LDA) for the exchange and correlation energies.[67] The following wavefunctions were used: for Ba *6s*, and *5d, 6p* and *4f* via the downfolding technique;[108] for Cu 4*s*, 4*p*, and 3*d*; for Ag 5*s*, 5*p*, 4*d* and 4*f* (downfolded); for Au *6s*, 6*p*, *5d* and *5f* (downfolded); for Si 3*s*, 3*p*, and 3*d* (downfolded); for Ge 4*s*, 4*p*, and 4*d* (downfolded); and for Te *5s*, *5p*, and *5d* and *4f* (the latter two downfolded). The integrations in *k* space were performed by an on a grid of 2080 (for sub cell compounds) or 960 (for super cell compounds) independent *k* points of the first Brillouin zone via an improved tetrahedron method.[68] To model the electron-precise formula $Ba_4M_4A_2Te_9$, we treated all coinage metal sites as fully occupied with the split sites omitted. In the Cu-Ge case, we calculated three models; two thereof with the Cu1, Cu2 and Te3 sites fully occupied, while in the first model Te4 was located on the 4g site (formally 50 %, necessitating symmetry reduction to $Pb2_1m$) and in the second Te4 was placed on the high symmetry 2a site, like in the Ag case. These two models of the formula $Ba_4Cu_4Ge_2Te_9$ have almost identical band structures. The third model was based on the Cu2A and Cu1A sites, having a Cu-deficient formula of $Ba_4Cu_3Ge_2Te_9$ and a linear Cu_3 unit instead of the Cu_4 cluster of $Ba_4Cu_4Ge_2Te_9$.

3.3.2 **Electronic structure calculation results**

The electronic structure calculation was based on the models $Ba_4M_4A_2Te_9$. In five cases, a forbidden gap separates the valence band from the conduction band, with the gap sizes of 0.24 eV for Ag-Ge, the 1.0 eV for Cu-Ge, 0.35 eV for the Ag-Si, 0.89 eV for the Cu-Si, and 0.19 eV for Au-Ge telluride. The DOS curves exhibit comparable slopes around E_F, but the *d* states occur at different regions: the Cu *d* states mostly appear between -2 eV and -4 eV, Ag *d* states dominate the area between -4 eV and -5.5 eV, and Au *d* states are around -4 eV to -6 eV. The states between E_F and the *d* states are dominated by Te *5p* states. The half filled *s* states of Si and Ge appear below the energy range chosen (Figure 3.9.). The model calculation with the Cu_3 cluster, formula $Ba_4Cu_3Ge_2Te_9$, indicates a much smaller gap of 0.3 eV, and the Fermi level is located 0.2 eV below the gap, indicative of a *p*-doped semiconductor. The model of $Ba_4Cu_3Ge_2Te_9$ is less important for the properties however, because it is based on the Cu2A atom with its 12 % occupancy.

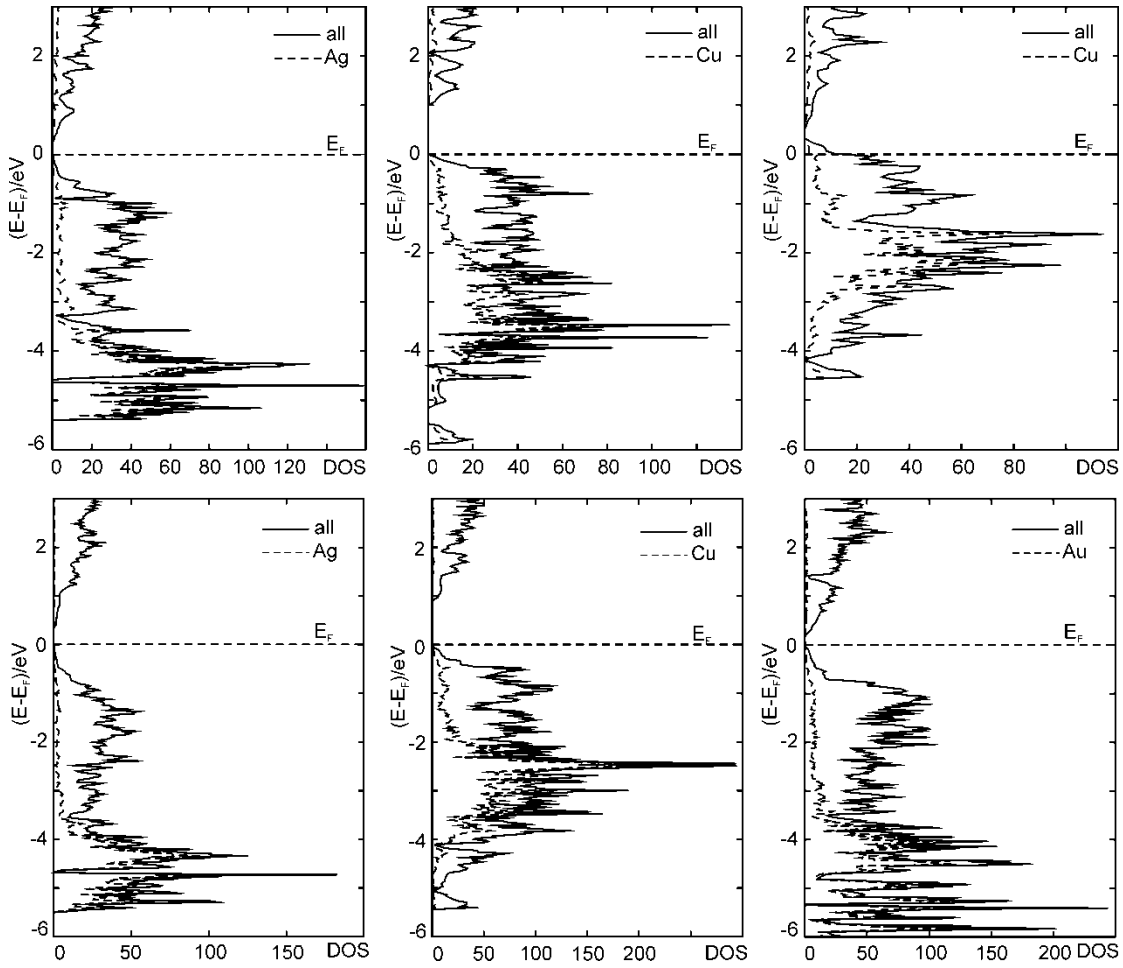

Figure 3.9. Densities of states. Top: $Ba_4Ag_4Ge_2Te_9$ (left), $Ba_4Cu_4Ge_2Te_9$ (center), and $Ba_4Cu_3Ge_2Te_9$ (right); bottom: $Ba_4Ag_4Si_2Te_9$ (left), $Ba_4Cu_4Si_2Te_9$ (center), and $Ba_4Au_4Ge_2Te_9$.

To gain insight into the character of the M–M contacts in the cluster, the crystal orbital Hamilton population curves[61, 111] of all the compounds are compared in Figure 3.10. The major contributions come from the respective *d* orbitals, and are thus mostly well below the Fermi level. Therefore, small decreases of the valence-electron numbers caused by the Ag/Cu/Au deficiencies will have only a minor impact on the strength of these interactions. The integration up to the Fermi level reveals that all shown interactions have net bonding character, reflected in negative ICOHPs.[62] For the Ag-Ge compound, these are -0.39 eV (2.89 Å for Ag2–Ag2) and -0.33 eV (3.04 Å for Ag1–

Ag2), for the Cu-Ge compound -0.82 eV (2.46 Å for Cu1–Cu2) and -0.42 eV (2.76 Å for Cu2–Cu2), for the Ag-Si -0.37 eV (2.89 Å for Ag2–Ag2) and -0.32 eV (3.03 Å for Ag1–Ag2), for the Cu-Si compound -0.68 eV (2.55 Å for Cu1–Cu2) -0.50 eV (2.74 Å for Cu2–Cu2) and -0.26 eV (2.97 Å for Cu2–Cu3), for the Au-Ge compound -1.01 eV (2.85 Å for Au1–Au2) -0.78 eV (2.85 Å for Au2–Au2) and -0.71 eV (2.99 Å for Au2–Au3). Hence within a given compound, the strength of the M–M interactions decreases with increasing bond length. In the $Ba_4Cu_3Ge_2Te_9$ model, only one (longer) Cu–Cu contact of 2.83 Å exists with a smaller ICOHP of -0.23 eV. Again, slight decreases of the valence electron concentration caused by the coinage metal deficiencies can only have a minor impact on the bond strengths, because the states directly below the Fermi level are basically nonbonding.

To analyze the bonding character of the long Au2–Te6 contact of 3.46 Å, we also calculated the Au2–Te ICOHPs. The small ICOHP value of -0.09 eV for the Au2–Te6 contact, compared with the other, shorter bonds with ICOHP values of -1.83 eV for Au2–Te1 (2.78 Å), -1.33 eV for Au2–Te3 (2.89 Å) and -2.11 eV for Au2–Te3 (2.71 Å), is indicative of a very weakly bonding interaction.

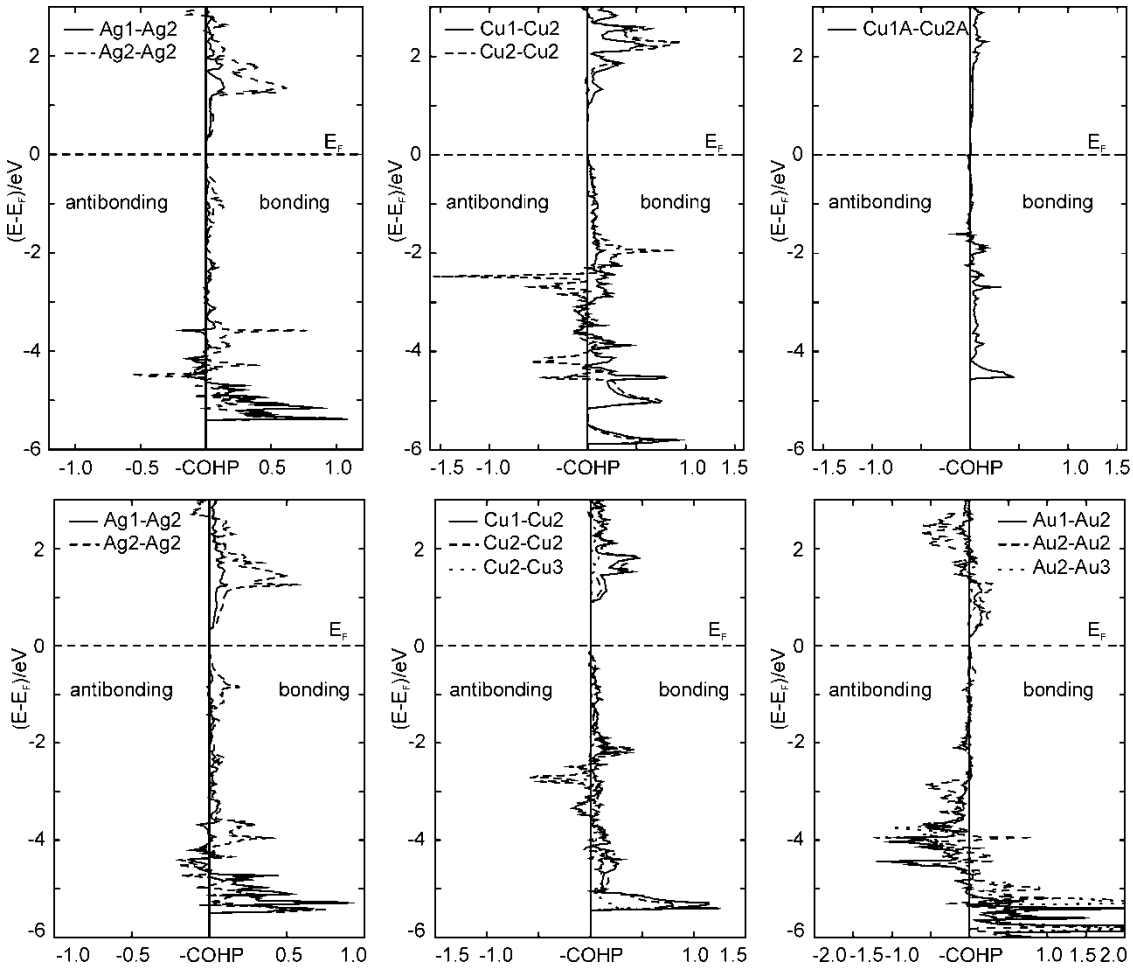

Figure 3.10. Metal–metal Crystal Orbital Hamilton Population curves. Top: $Ba_4Ag_4Ge_2Te_9$ (left), $Ba_4Cu_4Ge_2Te_9$ (center), and $Ba_4Cu_3Ge_2Te_9$ (right); bottom: $Ba_4Ag_4Si_2Te_9$ (left), $Ba_4Cu_4Si_2Te_9$ (center), and $Ba_4Au_4Ge_2Te_9$.

3.4 Physical properties

Cold pressed bars with the dimensions of 5×1×1 [in mm] for all five samples were used for physical transport measurements, since no single crystals of sufficient dimensions were available. Silver paint (Ted Pella) was used to create the electric contacts. The Seebeck coefficient, *S*, was determined by a commercial thermopower measurement apparatus (MMR Technologies) under dynamic vacuum in the temperature range from 300 K to 550 K. Constantan was used as an internal standard to determine the

temperature difference. The specific electrical conductivity, σ, was determined using a four-point-method: a homemade device was used to determine the voltage drops ΔV over distances (L) of approximately 1 mm at currents of 1 mA under dynamic vacuum from 320 K to 20 K. The achieved densities were between 85 % and 84 % of the theoretical maxima as determined via the single crystal structure studies. The resistances (R) were calculated from the voltage drops using Ohm's law, i.e. $R = \Delta V/I$, with I = current. We calculated $\sigma(T)$ after measuring the lengths between the contacts, L, according to $\sigma = L/(AR)$, with the area A = 1 mm × 1 mm.

The property measurements verified the semiconducting character. Almost exponential increases of the electrical conductivity with increasing temperature were observed for all tellurides (left part of Figure 3.11.), which is typical for semiconductors. That the temperature dependence is not exactly exponential, which reaffirms the observation that the materials exhibit Ag/Cu/Au deficiencies and thus extrinsic charge carriers (namely holes) in addition to the thermally activated carriers. The electrical conductivity is higher in case of the Au-Ge compound, which is consistent with the smaller calculated band gap.

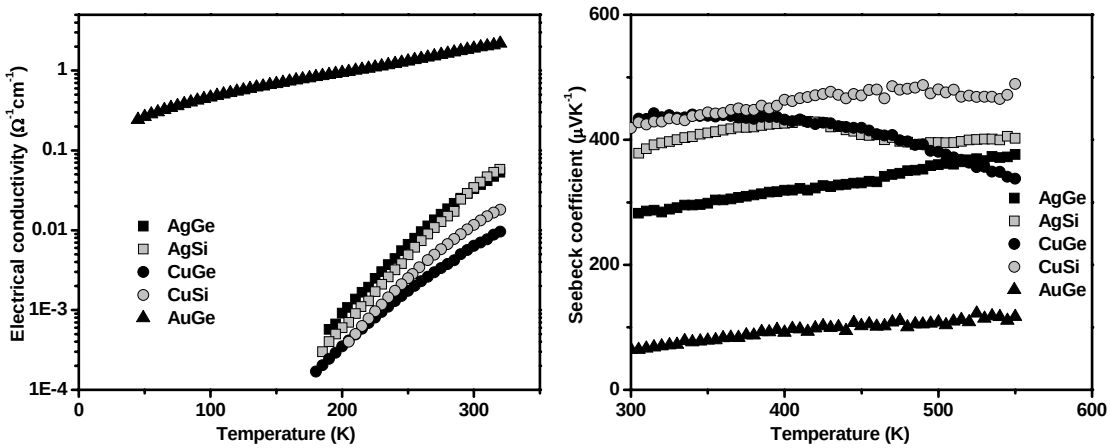

Figure 3.11. Electrical conductivity (left) and Seebeck coefficient (right) of $Ba_4Ag_4Ge_2Te_9$ (AgGe), $Ba_4Ag_4Si_2Te_9$ (AgSi), $Ba_4Cu_4Ge_2Te_9$ (CuGe), $Ba_4Cu_4Si_2Te_9$ (CuSi), and $Ba_4Au_4Ge_2Te_9$ (AuGe).

The positive values of the Seebeck coefficient reveal that *p*-type carriers are dominant in all compounds, which is in accord with the deficiencies of the coinage metals. For Ag-Ge telluride, the Seebeck coefficient increases with increasing temperature from 282 μV/K to 376 μV/K between 305 K and 550 K (right part of Figure 3.11.). For the Ag-Si telluride, Seebeck coefficient first increase with increasing temperature then decrease with a maximum being 408 μV/K at 450 K. Based on the equation $E_g = 2 \cdot e \cdot S_{max} \cdot T_{max}$,[138] the band gap, E_g, is estimated to be 0.37 eV. For Cu-Ge telluride, the Seebeck coefficient is relatively constant around 430 μV/K – 440 μV/K from 305 K to 340 K, and then decreases with increasing temperature down to 338 μV/K at 550 K. The band gap, E_g, is then estimated to be between 0.26 eV and 0.32 eV. The Cu-Si telluride exhibits the highest Seebeck coefficient of 488 μVK^{-1} at 490 K, which corresponds to an estimated band gap of 0.48 eV. While the Seebeck coefficient values of Au-Ge telluride increase slowly with increasing temperatures from 64 μVK^{-1} at 300 K to 117 μVK^{-1} at 550 K.

3.5 Conclusion

Five new tellurides, $Ba_4Ag_{3.95}Ge_2Te_9$, $Ba_4Ag_{3.97}Si_2Te_9$, $Ba_4Cu_{3.71}Ge_2Te_9$, $Ba_4Cu_{3.75}Si_2Te_9$, and $Ba_4Au_{3.69}Ge_2Te_9$, were prepared and characterized. They are composed of similar structure motifs, like the M_4 and A_2Te_6 units, but adopt different space groups, namely *Pbam* ($Ba_4Ag_{3.95}Ge_2Te_9$, $Ba_4Ag_{3.97}Si_2Te_9$, $Ba_4Cu_{3.71}Ge_2Te_9$) and *Pnma* ($Ba_4Cu_{3.75}Si_2Te_9$, $Ba_4Au_{3.69}Ge_2Te_9$). The latter is a super cell of the former, wherein the M_4 clusters are distorted yielding different M–M interactions and smaller M–Te coordination numbers. A phase transition observed in case of $Ba_4Au_{3.69}Ge_2Te_9$ at 690°C indicates that the super cell is likely the low temperature modification of the sub cell.

Physical property measurements showed that they are not suitable for thermoelectric application due to the rather low electrical conductivity though high Seebeck coefficient values were achieved.

Chapter 4 Thermoelectric Performance Optimization of *n*-type Doped Perovskite $SrTiO_3$

To date, thermoelectric materials, which are used for practical applications, include Bi_2Te_3[139] and Si-Ge.[140-142] Compared with these traditional thermoelectric materials, metal oxides may be more suitable for thermoelectric energy conversion at high temperatures due to their high thermal and chemical stability. Inspired by the striking thermoelectric performance of $NaCo_2O_4$,[21] most of the current studies are focused on cobalt-based *p*-type oxide semiconductors including $Na_xCo_2O_4$ or $Ca_2Co_2O_5$ [143, 144] and their derivatives.[145-147] On the other hand, *n*-type oxide semiconductors, which are indispensable as a partner of the *p*-type oxide semiconductors for thermoelectric device modules, have exhibited rather low *ZT* values. The present study targets the optimization of the thermoelectric performance of $SrTiO_3$. Heavily doped $SrTiO_3$ is a promising candidate for an *n*-type thermoelectric. Firstly, it exhibits rather large $|S|$ due to the large carrier effective mass.[148] Secondly, appropriate substitution doping can easily control the carrier concentration of $SrTiO_3$. The maximum *ZT* value for *n*-type thermoelectric materials has been reported to be 0.37 at 1000 K for an Nb-doped $SrTiO_3$ epitaxial film.[39] Ta-doped $SrTiO_3$ might also be a good or even better thermoelectric material, since Ta-doping compared with Nb-doping will result in the intensification of the phonon scattering and, correspondingly, the reduction of the lattice thermal conductivity.[149]

We have successfully doped Nb and Ta into $SrTiO_3$ samples, and a series of samples have been characterized by powder X-ray diffraction and EPMA.[150] After that, a double substitution was carried out; a series of La- and Nb/Ta-doped samples were characterized.[151] The physical properties, such as Seebeck coefficient, electrical conductivity, and thermal conductivity, were measured at high temperatures for all the samples.

4.1 Synthesis and analysis

4.1.1 Preparation of samples

Starting materials were $SrCO_3$ and binary oxides, i.e. La_2O_3, Nb_2O_5, Ta_2O_5, Ti_2O_3, and TiO_2. These materials were used as acquired, namely from Sigma Aldrich: $SrCO_3$, purity 99.9+ %, Ti_2O_3, purity 99.9 %, and from Alfa Aesar : La_2O_3, purity 99.9 %, TiO_2, purity 99.9 %, Nb_2O_5, purity 99.5 % and Ta_2O_5, purity 99.85 %. To avoid the formation of highly oxidized products, i.e. containing only Ti^{+4} and Nb/Ta^{+5}, the reactions (4-1 - 4-4) were carried out under dynamic high vacuum of the order of 10^{-6} mbar in aluminum boats.

$$\mathbf{SrCO_3 + (1-2x)TiO_2 + \frac{x}{2}Ti_2O_3 + \frac{x}{2}\,Ta_2O_5 \rightarrow SrTi_{1-x}Ta_xO_3 + CO_2} \quad \textbf{(4-1)}$$

$$\mathbf{SrCO_3 + (1-2x)TiO_2 + \frac{x}{2}\,Ti_2O_3 + \frac{x}{2}\,Nb_2O_5 \rightarrow SrTi_{1-x}Nb_xO_3 + CO_2} \quad \textbf{(4-2)}$$

$$\mathbf{(1-x)SrCO_3 + \frac{x}{2}\,La_2O_3 + (1-3x)TiO_2 + x\,Ti_2O_3 + \frac{x}{2}\,Ta_2O_5 \rightarrow Sr_{1-x}La_xTi_{1-x}Ta_xO_3 + (1-x)CO_2} \quad \textbf{(4-3)}$$

$$\mathbf{(1-x)SrCO_3 + \frac{x}{2}\,La_2O_3 + (1-3x)TiO_2 + x\,Ti_2O_3 + \frac{x}{2}\,Nb_2O_5 \rightarrow Sr_{1-x}La_xTi_{1-x}Nb_xO_3 + (1-x)CO_2} \quad \textbf{(4-4)}$$

The reactions (1) and (2) were attempted for x = 0, 0.01, 0.02 … 0.1, 0.14, 0.16 and 0.2; and reaction series (3) were carried out for x = 0.01, 0.05 and 0.10, reaction (4) was only carried out for x = 0.10 for comparison. In each case the mixtures were

thoroughly ground, and then calcined at 1200 °C over a period of 16 hours under dynamic high vacuum. Next, the products were cooled, ground again, and reheated at least once at 1500 °C for 16 hours, again under dynamic high vacuum.

4.1.2 **Phase analysis methods**

All products were routinely analyzed after each heating step via X-ray powder diffraction. Typically the X-ray powder patterns revealed that the samples were not homogeneous after the first heating cycle, requiring reheating two or more times. Rietveld refinements[152] were performed on all the phase-pure samples using the GSAS program[48, 49] via the graphical interface EXPGUI.[50]

Energy Dispersive X-ray Analysis (EDAX) was performed on selected crystals, using the electron microscope LEO 1530 with an additional EDAX device, EDAX Pegasus 1200. No heteroelements, such as Al from the crucibles, were detected in any case, and all samples appeared to be homogenous within the certainties of the EDAX method.

The Nb- and Ta-doped products were also analyzed by Electron Probe Micro Analysis (EPMA). All samples required an Au/Pd coating of 1 nm to diminish charging effects. The stoichiometry of the major phase of each sample was derived via X-ray fluorescence using $SrTiO_3$ as a standard. Atomic and weight percents for the major phases were determined by averaging the compositions of 16 randomly selected individual grains. Standard deviations accompanying atomic and weight percents were based on the variation of the composition between different grains in the sample and intrinsic X-ray counting statistics, and are therefore an implicit measurement of how homogenously the elements are distributed throughout the bulk.

4.1.3 **Rietveld refinements**

Regular powder X-ray diffraction (10 minute scans) data had shown that Nb/Ta-doped were pure phases with x up to 0.14, and La- together with Nb/Ta-double substituted samples with x up to 0.1. Then overnight measurements were carried out for all these samples, on which Rietveld refinement were performed. Some small additional peaks indicative of unidentified side products in the overnight measurement patterns led to a low quality refinement of sample $SrTi_{0.86}Ta_{0.14}O_3$ in agreement with the extra phases seen in the EPMA investigation. For the others, the Rietveld refinements generally confirmed the incorporation of the substituent elements into the perovskites, as shown in Table 4.1., with the absence of any additional reflections (examples shown in Figure 4.1.). Table 4.1. compares the lattice parameters, residual values, and *U* values of the Rietveld refinements.

Table 4.1. Rietveld refinements on pure and *n*-type doped $SrTiO_3$, space group *Pm*-3*m*. U_O was fixed to be 0.02 Å^2 in all cases.

Composition	*a*/Å	R_F^2/%	R_p/%	R_{wp}/%	U_{Sr}/Å^2	U_{Ti}/Å^2
$SrTiO_3$	3.9008(2)	2.81	4.19	6.31	0.0170(6)	0.0203(6)
$SrTi_{0.95}Ta_{0.05}O_3$	3.9099(1)	2.93	3.00	3.92	0.0157(4)	0.0199(4)
$SrTi_{0.90}Ta_{0.10}O_3$	3.9145(2)	3.00	3.52	4.16	0.0127(5)	0.0213(5)
$SrTi_{0.86}Nb_{0.14}O_3$	3.9187(1)	4.02	3.63	4.11	0.0134(5)	0.0169(5)
$Sr_{0.90}La_{0.10}Ti_{0.90}Nb_{0.10}O_3$	3.9132(2)	3.04	3.04	4.59	0.0181(5)	0.0159(5)
$Sr_{0.99}La_{0.01}Ti_{0.99}Ta_{0.01}O_3$	3.9051(1)	2.77	3.82	5.30	0.0177(5)	0.0193(5)
$Sr_{0.95}La_{0.05}Ti_{0.95}Ta_{0.05}O_3$	3.9111(2)	2.30	3.36	4.27	0.0166(5)	0.0189(6)
$Sr_{0.90}La_{0.10}Ti_{0.90}Ta_{0.10}O_3$	3.9150(2)	3.89	3.25	5.11	0.0209(7)	0.0181(6)

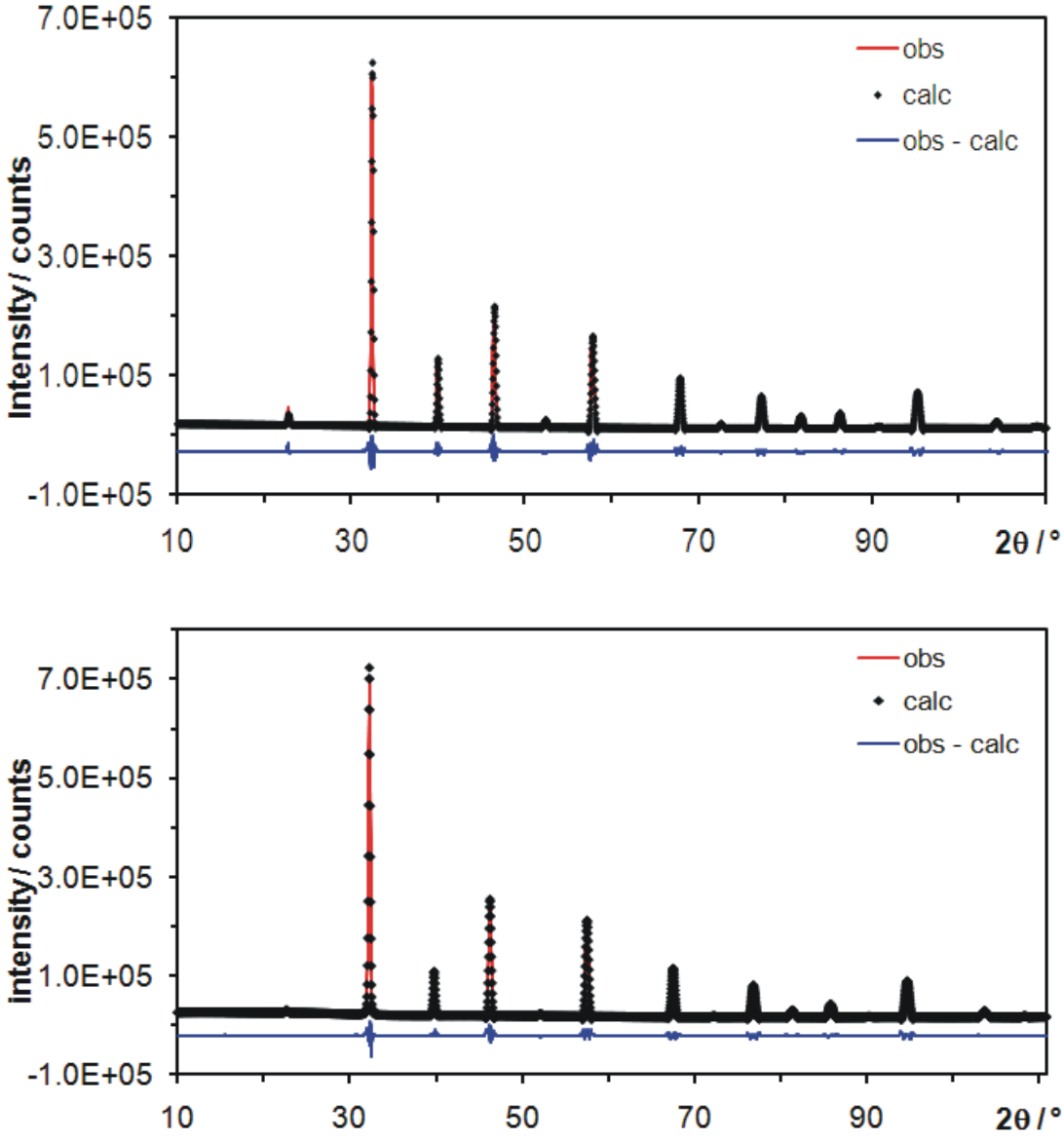

Figure 4.1. Rietveld refinements on $SrTiO_3$ (top) and $Sr_{0.9}La_{0.1}Ti_{0.9}Ta_{0.1}O_3$ (bottom).

All these doping experiments led to an increase in the unit cell size, e.g. from a = 3.901 Å for $SrTiO_3$ to 3.905 Å for $Sr_{0.99}La_{0.01}Ti_{0.99}Ta_{0.01}O_3$ and 3.919 Å for $SrTi_{0.86}Nb_{0.14}O_3$. However, we were mostly unable to reliably refine the occupancy of doped elements, and the isotropic thermal displacement parameters of oxygen (U_O). Therefore the occupancies were fixed to equal to the nominal (starting) composition, and

U_O fixed at 0.02 Å^2. The refined isotropic thermal displacement parameters may be used to justify this approach. All R_p values are below 5 %, indicating successful refinements and thus homogenous doping. The phase purity can further be testified by the comparable refinement results with $SrTi_{0.90}Ta_{0.10}O_3$, since the EPMA of $SrTi_{0.90}Ta_{0.10}O_3$, confirmed its homogeneity as well as the Ti/Ta ratio, with the analysis result being $Sr_{1.00(1)}Ti_{0.89(2)}Ta_{0.10(2)}O_{2.99(2)}$ (see details in next section).[150]

4.1.4 **EPMA analysis**

Rietveld refinements supported the postulation that all the doping elements were incorpoated in the perovskite structure. A series of apparently phase pure Ta doped perovskites $SrTi_{1-x}Ta_xO_3$ (x = 0.05, 0.10, and 0.14) and $SrTi_{0.86}Nb_{0.14}O_3$ were further characterized by EPMA, carried out by Dr. H. Wang at Oak Ridge.

Inspection of the elemental maps of this sample found a homogenous distribution of all constituent elements. A small volume fraction of NbO_x was detected, see maps below Figure 4.2. The back scattered electron (BSE) image in particular clearly shows NbO_x pockets and the generally homogenous nature of the sample. Standardized elemental analysis gives a stoichiometry of $Sr_{1.00(1)}Ti_{0.86(1)}Nb_{0.16(1)}O_{2.98(2)}$ in good agreement with the nominal composition.

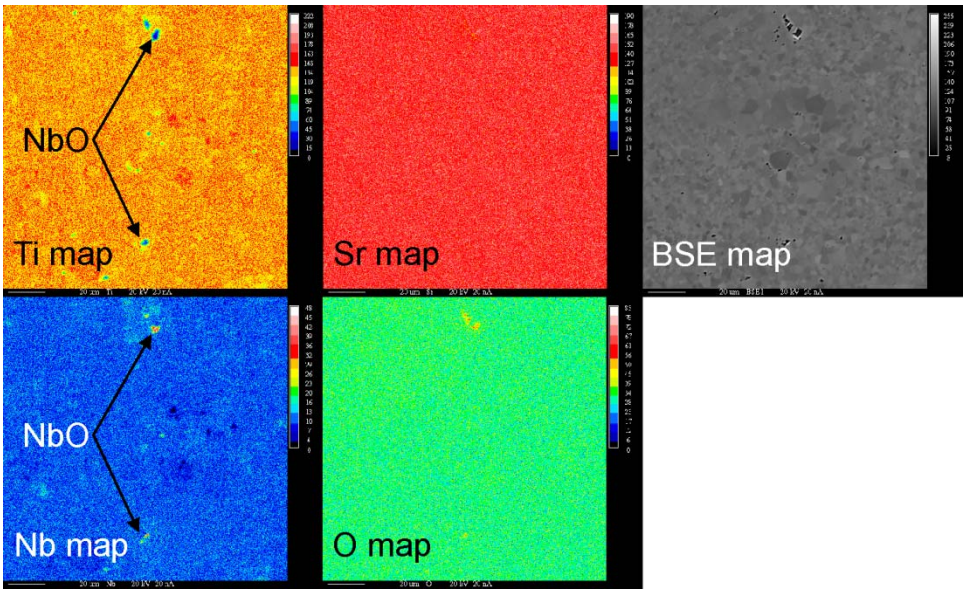

Figure 4.2. EPMA maps of $SrTi_{0.86}Nb_{0.14}O_3$.

Inspection of the elemental maps of $SrTi_{0.86}Ta_{0.14}O_3$ indicates a partly inhomogeneous distribution of the elements, as shown in Figure 4.3. Because the O map shows a more or less homogeneous elemental distribution, the Ta-rich areas seen as white and red regions in the Ta map are not TaO_x. Instead they correspond to quaternary phases that are poor in Ti and Sr as compared to the major phase. The inhomogeneity can be seen clearly in the BSE image as well. The white areas in the BSE image correspond to regions of high average atomic number (*Z*). The numerous black spots that appear in the BSE image indicate that the sample has relatively higher porosity, which may be caused by small variations in heating rates and sintering conditions used for the different samples.

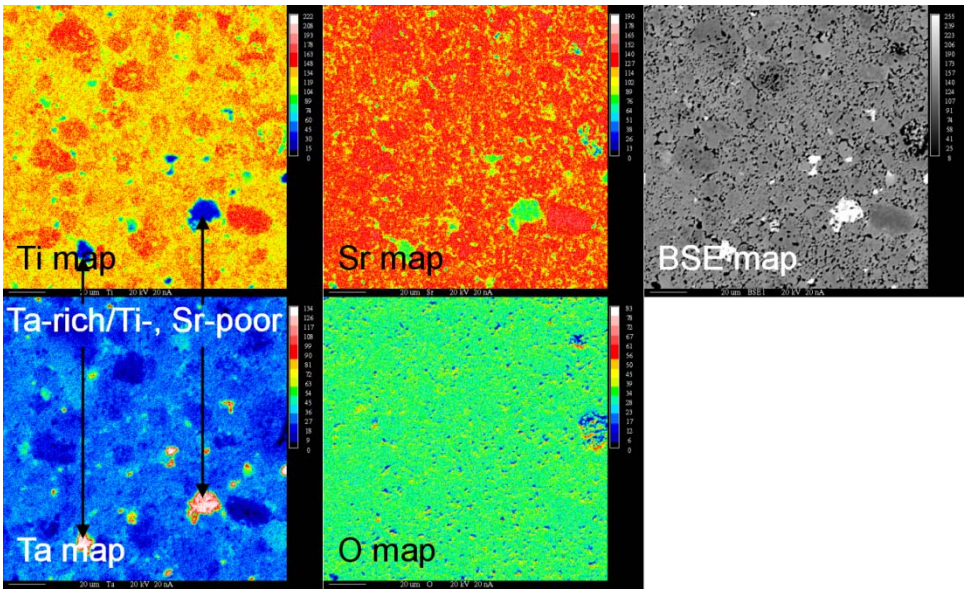

Figure 4.3. EPMA maps of $SrTi_{0.86}Ta_{0.14}O_3$.

Elemental analysis performed on the major phase (medium gray in BSE image) revealed the stoichiometry to be $Sr_{1.00(2)}Ti_{0.89(4)}Ta_{0.11(3)}O_{2.97(3)}$. The bright white region of the BSE image corresponds to $Sr_{5.8(2)}Ti_{1.0(3)}Ta_{5.4(5)}O_{20.5(1)}$. This indicates the solubility limit of Ta that can be substituted into $SrTiO_3$, hence a secondary quaternary phase forms when x = 0.11 is exceeded.

$SrTi_{0.90}Ta_{0.10}O_3$ is more homogeneous than $SrTi_{0.86}Ta_{0.14}O_3$ (Figure 4.4). The Ta-rich regions comprise a much smaller volume fraction, and no binary oxide pockets are found. However, there are regions in these maps where the content of all constituent elements is low, corresponding to voids. Again, these voids likely stem from small variations in the sintering conditions used for the different samples. The BSE image of this sample also shows very bright white regions (high average *Z*), but they are far fewer and smaller than those found in $SrTi_{0.86}Ta_{0.14}O_3$.

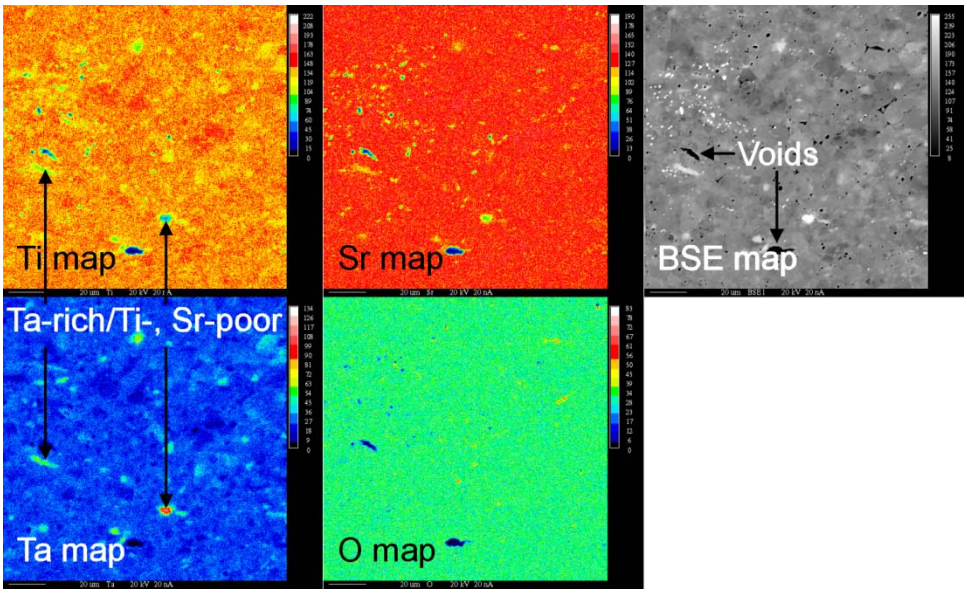

Figure 4.4. EPMA maps of $SrTi_{0.90}Ta_{0.10}O_3$.

Elemental analysis was again performed on the major phase (medium gray in the BSE image) and on the minor Ta rich phase (white regions in BSE image). The major phase was found to have the composition $Sr_{1.00(1)}Ti_{0.89(2)}Ta_{0.10(2)}O_{2.99(2)}$, which was in perfect agreement with the nominal composition within the error of the method. The standard deviations in this sample were smaller than in $SrTi_{0.86}Ta_{0.14}O_3$. This indicates a much more uniform elemental distribution amongst the grains. The composition of the minor phase was $Sr_{3.37(3)}Ti_{2.6(2)}Ta_{1.0(2)}O_{10.94(6)}$.

$SrTi_{0.95}Ta_{0.05}O_3$ was also found to have a slightly non-uniform distribution of Sr, Ta and Ti. The Figure 4.5 below shows that once again O was homogenous in the sample and there were no clear indications of any TiO_x or TaO_x regions. Based on the standard deviations of the atomic percentages determined from the major phase grains, it would appear that this sample was just as homogenous as $SrTi_{0.90}Ta_{0.10}O_3$ (see compositions listed below).

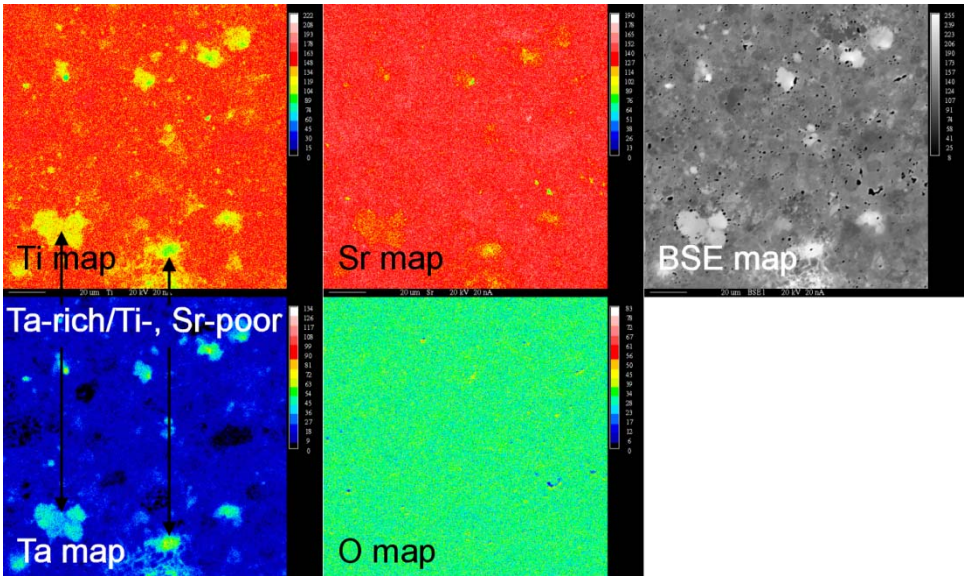

Figure 4.5. EPMA maps of $SrTi_{0.95}Ta_{0.05}O_3$.

Elemental analysis performed on the major phases, which were the light to medium grey grains in the BSE image above found the formula to be $Sr_{1.00(1)}Ti_{0.94(2)}Ta_{0.04(2)}O_{2.90(2)}$, which again agrees with the nominal composition within the error of the method, aside from the possibility of oxygen vacancies. The standard deviations in the chemical formula were nearly the same as that for $SrTi_{0.90}Ta_{0.10}O_3$, indicating a similar level of elemental distribution amongst the grains. The compositions of the lighter regions of BSE image were also determined and had the formula of $Sr_{14(1)}Ti_{1.0(2)}Ta_{8.0(8)}O_{35.1(4)}$.

Thus, it can be concluded that the substituent element Nb was homogenously doped into the target structure, but Ta was not as homogenously distributed, especially in the $SrTi_{0.86}Ta_{0.14}O_3$ sample. It may be because the solubility of Ta in $SrTiO_3$ is low causing secondary Ta-rich phases to form. These secondary phases make up a small volume fraction of the total sample, as is evident by the fact that the in-grain composition

of the major phase is quite close to the nominal composition for the x = 0.05 and 0.10 samples. Consequently, physical property measurements were carried out on these two samples and the Nb doped sample.

4.2 Electronic structure calculations

4.2.1 Calculation method

We utilized the self-consistent tight-binding *first principles* LMTO method (LMTO = linear muffin tin orbitals), with the atomic spheres approximation (ASA)[65, 66] for the electronic structure calculations. To model $SrTi_{1-x}M_xO_3$, a 2 × 2 × 2 supercell of the perovskites $SrTiO_3$ was created, wherein one of the eight Ti sites was replaced with an M atom (M = Nb, Ta). The space group $Pm\bar{3}m$ was retained, the resulting formula was $Sr_8Ti_7MO_{24}$, equivalent with $SrTi_{1-x}M_xO_3$ with x = 0.125. To model $Sr_{1-x}La_xTi_{1-x}M_xO_3$, a Sr site of that model was replaced with La, resulting in $Sr_7LaTi_7MO_{24}$, equivalent with $Sr_{1-x}La_xTi_{1-x}M_xO_3$ with x = 0.125, and a symmetry reduction to *R*3*m*. The integrations in *k* space were performed on grids of 165 independent *k* points of the first Brillouin zone for $Sr_8Ti_7MO_{24}$ (816 *k* points for $Sr_7LaTi_7MO_{24}$) via an improved tetrahedron method.[68] This ordering was only chosen to enable calculations of models of the right formula, not because such ordering was observed. In fact, the Rietveld data strongly suggest statistical mixtures of the doped elements.

4.2.2 Electronic structure calculation results

Electronic structure calculations were carried out for pure $SrTiO_3$, $SrTi_{0.875}M_{0.125}O_3$ and $Sr_{0.875}La_{0.125}Ti_{0.875}Ta_{0.125}O_3$. Since both Nb and Ta provide one more valence electron than Ti, a doping level of x = 0.125 formally corresponds to 2.1 ×

10^{21} electrons per cm^3, which is at the upper border of the ideal carrier concentration for thermoelectrics. Correspondingly, the nominal charge carrier concentration of $Sr_{0.875}La_{0.125}Ti_{0.875}Ta_{0.125}O_3$ is twice as high, because the Sr/La substitution yields an additional valence electron per incorporated La atom. Therefore, the samples investigated cover a larger (formal) carrier concentration range between 3.4×10^{20} ($Sr_{0.99}La_{0.01}Ti_{0.99}Ta_{0.01}O_3$) and 3.4×10^{21} ($Sr_{0.90}La_{0.10}Ti_{0.90}Ta_{0.10}O_3$) electrons per cm^3.

The rather large computed gap of $SrTiO_3$ of 1.30 eV (Figure 4.6.) indicates that the ideal operating temperature for thermoelectrics based on variants of this material will be high.[153] Its faint yellow color implies that the actual band gap is even larger, noting that the size of the gap is usually underestimated in DFT calculations. The band structures of *n*-type doped $SrTiO_3$ materials are also shown in Figure 4.6., with the omission of the Nb case, which is equivalent with the Ta case. The band structure of the model $SrTi_{0.875}Ta_{0.125}O_3$ and $Sr_{0.875}La_{0.125}Ti_{0.875}Ta_{0.125}O_3$ exhibits a gap of 1.27 eV and 1.40 eV respecitvely, but the Fermi level falls into a region of steep bands within the conduction band.

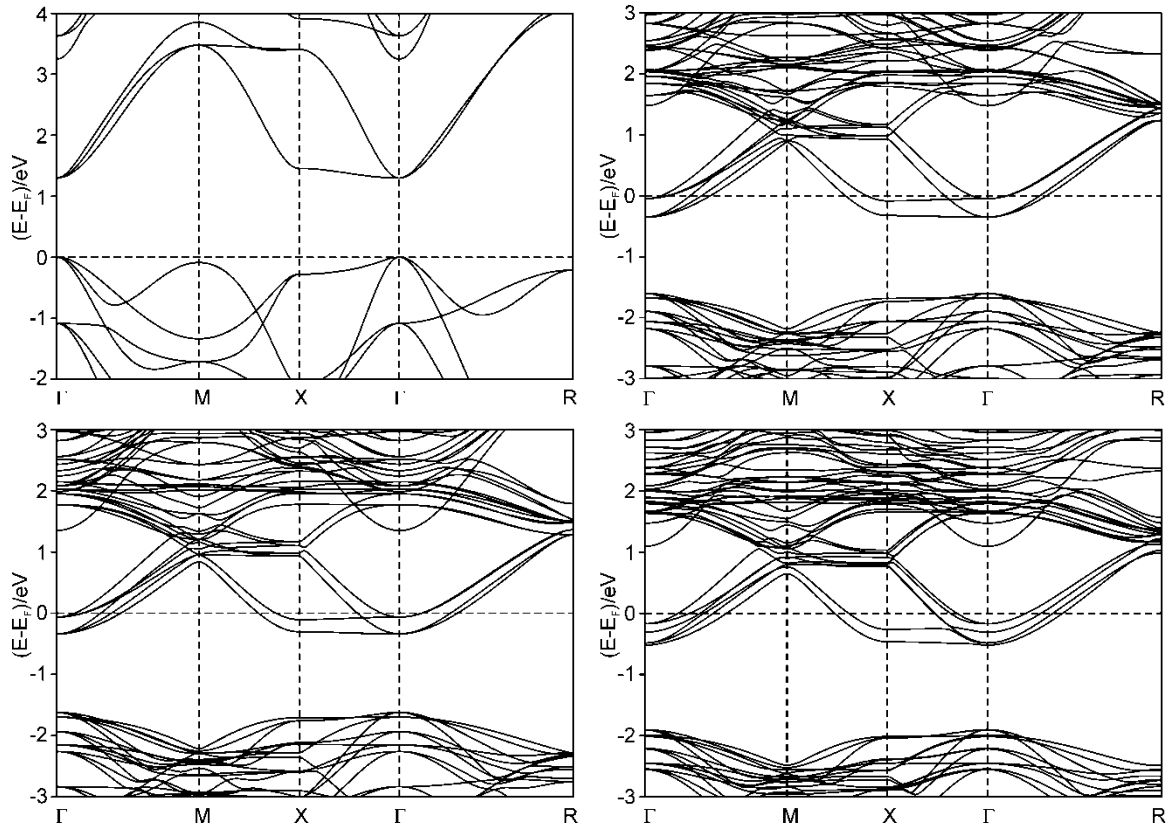

Figure 4.6. Band structures of $SrTiO_3$ (top left), $SrTi_{0.875}Nb_{0.125}O_3$ (top right), $SrTi_{0.875}Ta_{0.125}O_3$ (bottom left) and $Sr_{0.875}La_{0.125}Ti_{0.875}Ta_{0.125}O_3$ (bottom right).

A very flat band occurs directly above the gap of $SrTiO_3$, and runs almost horizontally along a^* ($\Gamma \rightarrow X$), indicative of a high effective mass, m^*, and thus a large Seebeck coefficient of appropriately *n*-doped $SrTiO_3$. The degeneracy at the Γ point also indicates a high Seebeck coefficient (equation (1-11)).[15] On the other hand, highly disperse bands run along $\Gamma \rightarrow M$ and $\Gamma \rightarrow R$, which points towards high mobility, μ, and thus high electrical conductivity (equation (1-9)).[64, 154, 155] The band structures of $SrTi_{0.875}Ta_{0.125}O_3$ and $Sr_{0.875}La_{0.125}Ti_{0.875}Ta_{0.125}O_3$ are very comparable, but the degeneracies are in part destroyed. Depending on the exact doping level, the Fermi level will be lower, possibly falling into the region with the flat bands just above the gap. Band structure calculations using various models indicate that doping has a profound

impact on the band gap size, the slope of the bands and therefore on the Seebeck coefficient as well as the conductivity values.

4.3 Physical properties

4.3.1 Measurement methods

Measurements were performed at four different institutions, namely at the University of Waterloo, Clemson University, General Motors Research & Development Center in Warren, and Oak Ridge National Laboratory.

Prior to the measurements, the microcrystalline samples were finely ground and then compacted via pressing. Three different pressing methods were applied: cold-pressing at Waterloo, isostatic hot-pressing at McMaster University in Hamilton by Rob at 1300 °C and 70 MPa, and spark plasma sintering (SPS) at Clemson by Dr. He (1400 °C and 80 MPa) and at Warren, General Motors R&D center by Dr. Salvador (1400 °C and 50 MPa).

At Waterloo, Seebeck measurements were performed under vacuum between 300 K and 550 K with the MMR SB100, and electrical conductivity measurements under vacuum between 10 K and 290 K with a homemade apparatus utilizing the classical four-point method. Thermal diffusivity, D, was measured with the Anter FL3000 under a flow of argon between 450 K and 1200 K. The thermal conductivity, κ, was computed via $\kappa = C_p \cdot D \cdot \rho$, with ρ being the density and C_p the specific heat, either obtained from the Dulong-Petit approximation or a DSC measurement at Warren. These measurements were performed on the samples $Sr_{1-x}La_xTi_{1-x}Ta_xO_3$ after hot-pressing in Hamilton.

Simultaneous high temperature Seebeck coefficient and electrical conductivity measurements were performed up to 1000 K under a helium atmosphere with an ULVAC ZEM-2 system either at Oak Ridge by Dr. Wang ($SrTi_{1-x}Nb_xO_3$ and $SrTi_{1-x}Ta_xO_3$) and or at Clemson by Dr. He (double substituted $Sr_{1-x}La_xTi_{1-x}M_xO_3$). The thermal diffusivity measurements of these samples were carried out with an Anter FL5000 (Oak Ridge) or a Netzsch LFA 457 (Clemson), both using the flash method.[150, 156-158]

4.3.2 **Properties of $SrTi_{1-x}M_xO_3$**

Three large phase pure samples of the nominal formulas $SrTi_{0.86}Nb_{0.14}O_3$, $SrTi_{0.95}Ta_{0.05}O_3$, and $SrTi_{0.90}Ta_{0.10}O_3$, were analyzed at the GM R&D center by Dr. J. Salvador and at Oak Ridge by Dr. H. Wang. The densities achieved were consistently 4.8 gcm^{-3}, i.e. about 90 % of the theoretical maximum. Figure 4.7. shows the temperature dependence of the Seebeck coefficient, electrical conductivity, thermal conductivity, and dimensionless figure of merit *ZT* values between 325 K and 750 K. The Seebeck coefficients of all three samples (Figure 4.7.a) are negative across the whole measured temperature range, proving the *n*-type conduction, as expected from doping with a more electron-rich metal. In all cases, the absolute *S* values increase smoothly with increasing temperature from room temperature values near -100 μVK^{-1}. For comparison, Muta *et al.* reported a Seebeck value of -82 μVK^{-1} at 300 K for $Sr_{0.9}La_{0.1}TiO_3$.[158]

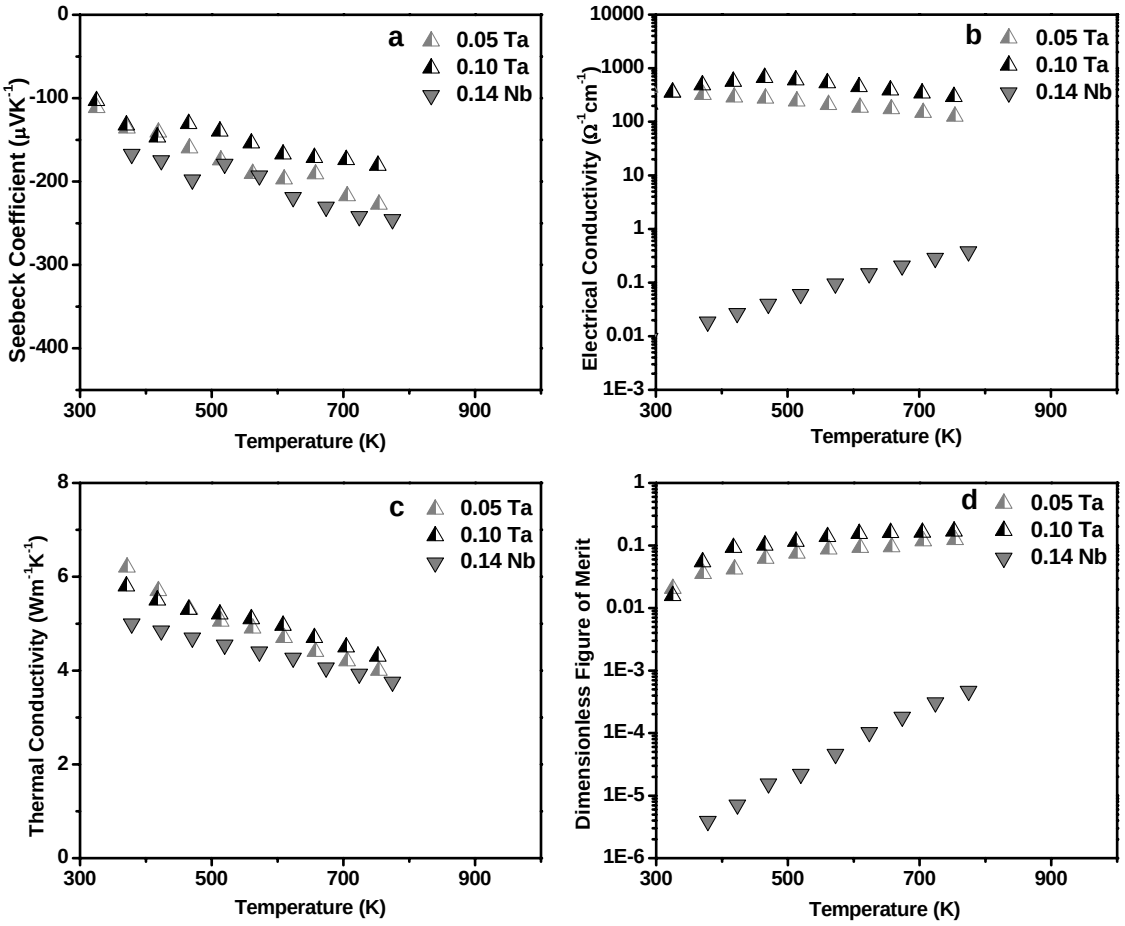

Figure 4.7. Thermoelectric properties of $SrTi_{1-x}Nb_xO_3$ and $SrTi_{1-x}Ta_xO_3$.

The Nb sample exhibits rather low σ values of 0.01 $\Omega^{-1}cm^{-1}$ compared to the Ta doped samples with values of 240 $\Omega^{-1}cm^{-1}$ and 420 $\Omega^{-1}cm^{-1}$ for $SrTi_{0.95}Ta_{0.05}O_3$ and $SrTi_{0.90}Ta_{0.10}O_3$ respectively, at room temperature (Figure 4.7.b). Moreover, the latter two samples show (at elevated temperatures) a negative temperature dependence of σ, likely owing to the high availability of the extrinsic charge carriers at lower temperatures. These electrical conductivity results are consistent with the results of Nb and Ta doped $CaMnO_3$ system.[159] The B site (here Ti site) doping not only changed the carrier concentration, but also introduced some scattering centers, which can cause the carrier to

localize, especially at high doping level.[159] The electrical conductivity of $SrTi_{0.86}Nb_{0.14}O_3$ increases with increasing temperature in all the measurement temperature range. The electrical conductivity of $SrTi_{0.90}Ta_{0.10}O_3$ increases with increasing temperature until 465 K, and then starts to decrease with increasing temperature. This indicates an onset of some additional electron scattering mechanism, the origin of which is unknown at this point. On the other hand, $SrTi_{0.95}Ta_{0.05}O_3$ exhibits the typical temperature dependence of a heavily doped (degenerate) semiconductor throughout the whole temperature range.

The (extrapolated) room-temperature thermal conductivity values are slightly above 6 $Wm^{-1}K^{-1}$ for all three samples, which agrees with the values from Muta *et al.* for $Sr_{0.9}La_{0.1}TiO_3$, with κ (300 K) = 6.8 $Wm^{-1}K^{-1}$. In the high temperature range from 325 K to 750 K, the κ values decrease with increasing temperature, reaching 3.76 $Wm^{-1}K^{-1}$at 774 K for $SrTi_{0.86}Nb_{0.14}O_3$, 4.3 $Wm^{-1}K^{-1}$ at 752 K for $SrTi_{0.90}Ta_{0.10}O_3$ and 4 $Wm^{-1}K^{-1}$ at 754 K for $SrTi_{0.95}Ta_{0.05}O_3$, as shown in Figure 4.7.c.[158]

From the results of these measurements, the thermoelectric figure-of-merit, *ZT*, was calculated via $ZT = S^2\sigma T/\kappa$. Nevertheless their *ZT* values increase steadily with increasing temperature (Figure 4.7.d), culminating in *ZT* = 0.17 for $SrTi_{0.90}Ta_{0.10}O_3$ at 752 K, which is rather high for an *n*-type thermoelectric oxide bulk material.[158-161] Since *ZT* continues to increase at that temperature, its maximum is likely higher, but we were unable to measure *ZT* beyond 752 K.

4.3.3 Properties of $Sr_{1-x}La_xTi_{1-x}M_xO_3$

The densities achieved were consistently 4.8 gcm^{-3}, i.e. about 90 % of the theoretical maximum. For double substituted samples, different samples were used for

property measurements at Waterloo and Clemson that underwent the same synthesis conditions. The hot-pressing consistently yielded consistent densities of 4.8 gcm^{-3} (thus between 93 % for x = 0.01 and 86 % for x = 0.10), whereas the SPS gave varying results, namely 5.1 gcm^{-3} for $Sr_{0.99}La_{0.01}Ti_{0.99}Ta_{0.01}O_3$ (99 %) and 4.8 gcm^{-3} both for $Sr_{0.95}La_{0.05}Ti_{0.95}Ta_{0.05}O_3$ (90 %) and $Sr_{0.90}La_{0.10}Ti_{0.90}Ta_{0.10}O_3$ (86 %). In addition, a sample of the nominal composition $Sr_{0.90}La_{0.10}Ti_{0.90}Nb_{0.10}O_3$ was compacted via SPS, giving a high density of 5.0 gcm^{-3}, thus 93 % of the theoretical maximum.

In all four samples compacted via SPS, the absolute Seebeck values increase smoothly with increasing temperature (Figure 4.8.a). For the La- and Ta-doped samples, the absolute Seebeck values decrease with increasing doping level (from -150 μVK^{-1} for x = 0.01 to -50 μVK^{-1} for x = 0.10 at 320 K), which is comparable to the results of Ta only doped samples.[150] The La- and Nb-doped sample has a higher absolute Seebeck value compared to the corresponding La- and Ta-doped sample, $Sr_{0.90}La_{0.10}Ti_{0.90}Ta_{0.10}O_3$ (-75 μVK^{-1} vs. -50 μVK^{-1} at 320 K). The hot-pressed samples follow the same trends, with consistently higher values that range from -270 μVK^{-1} to -75 μVK^{-1} at 320 K (Figure 4.9.a).

The electrical conductivity increases rapidly with increasing temperature for the samples with x = 0.05 and x = 0.10 over the whole temperature range measured, indicative for dominantly temperature activated conduction. The Nb material exhibits higher electrical conductivity, compared to the analogous Ta material, which may be due to its higher density. On the other hand, the electrical conductivity for the lowest La/Ta-doped sample (x = 0.01) is higher than for the highly doped samples in the measured

temperature range and is decreasing with increasing temperature, indicative of a significant number of extrinsic charge carriers.

The above is true for both SPS and hot-pressed samples with x = 0.01, with the hot-pressed sample having lower absolute values, e.g. at room temperature 65 $\Omega^{-1}cm^{-1}$, compared to 600 $\Omega^{-1}cm^{-1}$ for the SPS sample. The latter is likely in part a consequence of the higher density of the SPS sample of 5.1 gcm^{-3} vs. 4.8 gcm^{-3}, i.e. 99 % vs. 93 % of the theoretical maximum. This higher density is likely a consequence of the higher pressure and temperature involved as well as localized heating, occurring with smaller grain boundary effects. Small differences in the charge carrier concentration, however, cannot be excluded because different samples - albeit of the same nominal composition - were used.

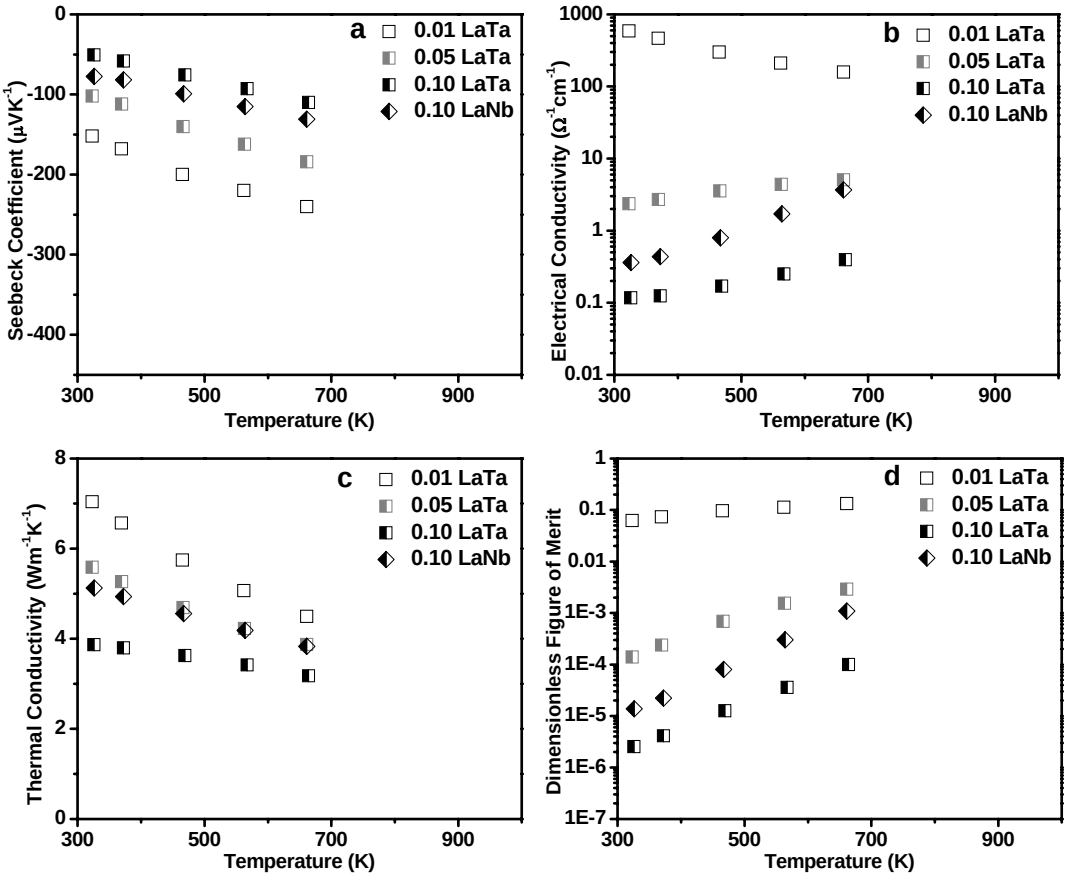

Figure 4.8. Thermoelectric properties of $Sr_{1-x}La_xTi_{1-x}Nb_xO_3$ and $Sr_{1-x}La_xTi_{1-x}Ta_xO_3$ (compacted via SPS).

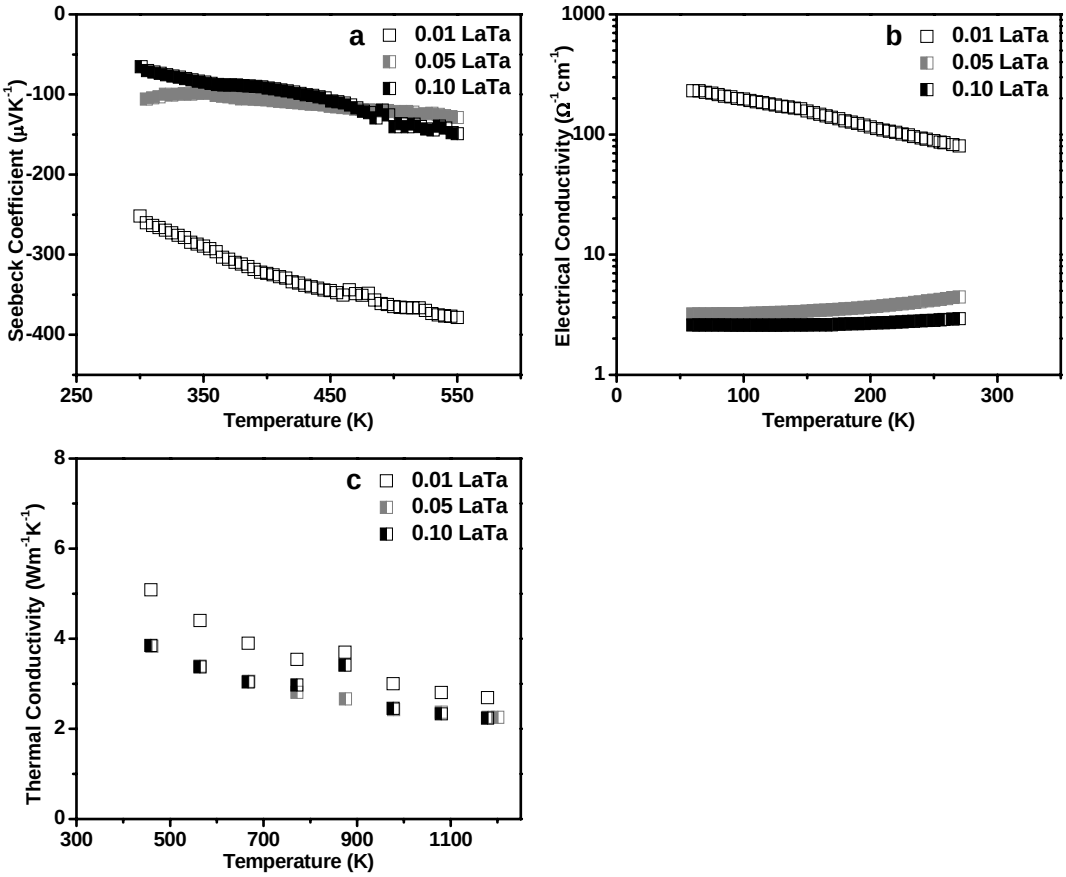

Figure 4.9. Thermoelectric properties of $Sr_{1-x}La_xTi_{1-x}Nb_xO_3$ and $Sr_{1-x}La_xTi_{1-x}Ta_xO_3$ (compacted via hot-pressing). *ZT* values could not be obtained because of the different temperature ranges.

The thermal conductivity, κ, decreases with the increase of x, and $Sr_{0.90}La_{0.10}Ti_{0.90}Nb_{0.10}O_3$ exhibits a higher thermal conductivity compared to $Sr_{0.90}La_{0.10}Ti_{0.90}Ta_{0.10}O_3$. The absolute values are lower than the numbers from Muta et al. for $Sr_{0.9}La_{0.1}TiO_3$ with κ (300 K) = 6.8 $Wm^{-1}K^{-1}$, except for $Sr_{0.99}La_{0.01}Ti_{0.99}Ta_{0.01}O_3$. The hot-pressed samples exhibit the same trends as the SPS samples, albeit with lower values, which supports the above-mentioned larger grain boundaries of the hot-pressed samples.

Like in the other cases of doped $SrTiO_3$, *ZT* increases with increasing temperature (Figure 4.8.d). For the hot-pressed samples, *ZT* values could not be obtained because of

the different temperature ranges of Seebeck, electrical conductivity and thermal conductivity measurements. The lowest doped sample, $Sr_{0.99}La_{0.01}Ti_{0.99}Ta_{0.01}O_3$, exhibits the largest *ZT*, e.g. 0.13 at 660 K, comparable with $SrTi_{0.95}Ta_{0.05}O_3$ (0.10 at 650 K),[150] while the *ZT* values of the other double substituted samples remain under 0.003. It is postulated that *ZT* will continue to increase at higher temperatures, and ongoing investigations are planned to reveal the extent of that expected increase. Moreover, as $Sr_{0.90}La_{0.10}Ti_{0.90}Nb_{0.10}O_3$ has higher *ZT* values than $Sr_{0.90}La_{0.10}Ti_{0.90}Ta_{0.10}O_3$ over the whole temperature range, an investigation of more, differently doped Nb materials appears to be promising.

4.4 Conclusion

In conclusion, we have successfully prepared and characterized two series of strontium titanates as *n*-type degenerate semiconductors as which led to significant improvements of the thermoelectric properties of the parent material $SrTiO_3$. The *ZT* values increase with increasing temperature in both cases, with a highest *ZT* value of 0.17 for $SrTi_{0.90}Ta_{0.10}O_3$ at 752 K. The rapid increases imply that higher *ZT* values are likely to occur at higher temperatures.

Chapter 5 Conclusion

The objective of this thesis is to investigate thermoelectric materials including two directions: one is to synthesize and characterize new materials with ideally good thermoelectric performances; the other one is to optimize the thermoelectric performance of known potential thermoelectric application candidates.

Two new tellurides, $Ba_7Au_2Te_{14}$ and $Ba_{6.76}Cu_{2.42}Te_{14}$, crystallizing in the $NaBa_6Cu_3Te_{14}$ structure type, were successfully synthesized and structurally characterized. Both materials are semiconductors, with calculated band gaps of 0.7 eV and 1.0 eV. Because these gaps are larger than ideal for the thermoelectric energy conversion, and the structures comprise molecular motifs, both materials exhibit low electrical conductivity.

Five more quaternary tellurides, $Ba_4M_{4-x}A_2Te_9$ (M = Cu, Ag, Au; A = Si, Ge), were successfully synthesized and characterized to form two different space group *Pbam* and *Pnma*, respectively. These materials are hole-doped semiconductors, originating from the Cu/Ag/Au deficiencies, with calculated gaps from 0.19 eV to 1.0 eV. The electrical conductivity is too low for thermoelectric applications, while high Seebeck coefficient values were achieved in all five cases. Attempts to synthesize "$Ba_4Au_4Si_2Te_9$" were not successful, but resulted in a new unknown phase with an approximate Ba : Au : Si : Te ratio of 4 : 1 : 2 : 9 and a new structure type, based on a tentative low quality single crystal structure study. Therefore, further investigations in this quaternary

system are still of great interest, as evidently new structures with hitherto unknown properties continue to be found.

Based on the strong performance of selected doped $SrTiO_3$ materials, $SrTiO_3$ served as the material of choice in this project. Two series of doping experiments, $SrTi_{1-x}Ta_xO_3$ and $Sr_{1-x}La_xTi_{1-x}Ta_xO_3$, were performed. In both series of doped $SrTiO_3$, *ZT* increases with increasing temperature. Best results were obtained by Ta-doped $SrTiO_3$, $SrTi_{0.90}Ta_{0.10}O_3$, with a *ZT* value of 0.17 for at 752 K, and the spark-plasma-sintered double substituted $Sr_{0.99}La_{0.01}Ti_{0.99}Ta_{0.01}O_3$ with a *ZT* of 0.13 at 660 K, respectively. Such *ZT* values are very competitive among *n*-type oxides. The rapid increases in the *ZT*-*T* curves in all the cases imply that higher *ZT* values are likely to occur at higher temperatures. The materials investigated comply with the initial criteria of low cost, low toxicity and high thermal stability. Further optimization is required to become competitive, for example with *p*-type Na_xCoO_2. In addition to these bulk materials investigations, attempts to form nanocomposites based on these perovskites are well worthwhile, because their high thermal conductivity is the main hindrance to better thermoelectric performance.

References

[1] T. J. Seebeck, *Magnetic Polarization of Metals and Minerals*, Abhand. Deut. Akad. Wiss, Berlin, **1822**.
[2] J. C. Peltier, *Ann. Chem.* **1834**, *LVI*, 371.
[3] W. Thomson, in *Proc. Roy. Soc.* , Edinburgh, **1851**, pp. 91.
[4] D. M. Rowe, *CRC Handbook of Thermoelectrics*, CRC Press, Boca Raton, FL, **1995**.
[5] A. F. Ioffe, *Semiconductor Thermoelements and Thermoelectric Cooling*, Infosearch, London, **1957**.
[6] http://www.globalte.com/index.php?pageId=2&sId=31.
[7] http://gizmodo.com/tag/space-cooler/.
[8] G. J. Snyder, E. S. Toberer, *Nature Mater.* **2008**, *7*, 105.
[9] D. Greig, *Electrons in Metals and Semiconductors*, McGraw-Hill, London, **1969**.
[10] T. K. Reynolds, J. G. Bales, R. F. Kelley, F. J. DiSalvo, in *Chemistry, Physics, and Materials Science of Thermoelectric Materials, Beyond Bismuth Telluride* (Eds.: M. G. Kanatzidis, S. D. Mahanti, T. P. Hogan), Kluwer Academic/Plenum Publishers, Traverse City, MI., **2002**.
[11] M. Cutler, J. F. Leavy, R. L. Fitzpatrick, *Phys. Rev. A* **1964**, *133*, 1143.
[12] T. K. Reynolds, J. G. Bales, R. F. Kelley, F. J. DiSalvo, in *Chemistry, Physics, and Materials Science of Thermoelectric Materials, Beyond Bismuth Telluride* (Eds.: M. G. Kanatzidis, S. D. Mahanti, T. P. Hogan), Kluwer Academic/Plenum Publishers, Traverse City, Michigan, **2002**, pp. 19.
[13] H. J. Goldsmid, *Thermoelectric Refrigeration*, Plenum Press, New York, NY, **1964**.
[14] D. A. Wright, *Nature* **1958**, *181*, 834.
[15] F. J. DiSalvo, *Science* **1999**, *285*, 703.
[16] C. M. Bhandari, in *CRC Handbook of Thermoelectrics* (Ed.: D. M. Rowe), Boca Raton, FL, **1995**, pp. 55.
[17] G. A. Slack, in *CRC Handbook of Thermoelectrics* (Ed.: D. M. Rowe), CRC Press, Boca Raton, FL, **1995**, pp. 407.
[18] C. Uher, *Semiconductors and Semimetals* **2001**, *69*, 139.
[19] K. A. Kovnir, A. V. Shevelkov, *Russ. Chem. Rev.* **2004**, *70*, 923.
[20] M. S. Dresselhaus, G. Chen, M. Y. Tang, R. Yang, H. Lee, D. Wang, Z. Ren, J.-P. Fleurial, P. Gogna, *Adv. Mater.* **2007**, *19*, 1043.
[21] I. Terasaki, Y. Sasago, K. Uchinokura, *Phys. Rev. B* **1997**, R12685.
[22] D.-Y. Chung, T. Hogan, P. Brazis, M. Rocci-Lane, C. Kannewurf, M. Bastea, C. Uher, M. G. Kanatzidis, *Science* **2000**, *287*, 1024.
[23] B. Wölfing, C. Kloc, J. Teubner, E. Bucher, *Phys. Rev. Lett.* **2001**, *86*, 4350.
[24] J. W. Sharp, B. C. Sales, D. G. Mandrus, B. C. Chakoumakos, *Appl. Phys. Lett.* **1999**, *74*, 3794.
[25] K. F. Hsu, S. Loo, F. Guo, W. Chen, J. S. Dyck, C. Uher, T. Hogan, E. K. Polychroniadis, M. G. Kanatzidis, *Science* **2004**, *303*, 818.

[26] J. S. Dyck, W. Chen, C. Uher, L. Chen, X. Tang, T. Hirai, *J. Appl. Phys.* **2002**, *91*, 3698.
[27] V. L. Kuznetsov, L. A. Kuznetsova, A. E. Kaliazin, D. M. Rowe, *J. Appl. Phys.* **2000**, *87*, 7871.
[28] T. F. Caillat, J. P.; Borshchevsky, A., *J. Phys. Chem. Solids* **1997**, *58*, 1119.
[29] Q. Shen, L. Chen, T. Goto, T. Hirai, J. Yang, G. P. Meisner, C. Uher, *Appl. Phys. Lett.* **2001**, *79*, 4165.
[30] G. S. Nolas, J. Poon, M. Kanatzidis, *Mater. Res. Soc. Bull.* **2006**, *31*, 199.
[31] T. M.Tritt, M. A. Subramanian, *Mater. Res. Soc. Bull.* **2006**, *31*, 188.
[32] E. Quarez, K.-F. Hsu, R. Pcionek, N. Frangis, E. K. Polychroniadis, M. G. Kanatzidis, *J. Am. Chem. Soc.* **2005**, *127*, 9177.
[33] T. C. Harman, P. J. Taylor, M. P. Walsh, B. E. LaForge, *Science* **2002**, *297*, 2229.
[34] G. Chen, *Phys. Rev. B* **1998**, *57*, 14958.
[35] R. Venkatasubramanian, E. Slivola, T. Colpitts, B. O'Quinn, *Nature* **2001**, *413*, 597.
[36] R. Funahashi, I. Matsubara, H. Ikuta, T.Takeuchi, U. Mizutani, S. Sodeoka, *Jpn. J. Appl. Phys. Pt. 2* **2000**, L1127.
[37] H. Leligny, D. Grebille, O. Pérez, A.-C. Masset, M. Hervieu, C. Michel, B. Raveau, *C.R. Acad. Sci. Paris t.2* **1999**, *Série IIc*, 409.
[38] T. Yamamoto, I. Tsukada, K. Uchinokura, M. Takagi, T. Tsubone, M. Ichihara, K. Kobayashi, *Jpn. J. Appl. Phys. Pt. 2* **2000**, *39*, L747.
[39] S. Ohta, T. Nomura, H. Ohta, K. Koumoto, *J. Appl. Phys.* **2005**, *97*, 034106/1.
[40] U. Schubert, N. Hüsing, *Synthesis of Inorganic Materials*, 2nd ed., Wiley-VCH, Weinheim, Germany, **2005**.
[41] W. L. Bragg, *Proc. Camb. Phil. Soc.* **1913**, *17*, 43.
[42] L. A. Aslanov, G. V. Fetisov, J. A. K. Howard, *Crystallographic Instrumentation*, Oxford University Press, New York, **1998**.
[43] L. E. Smart, E. A. Moore, *Solid State Chemistry: an Introduction*, 3rd ed., CRC Press, Boca Raton, FL, **2005**.
[44] http://www.matter.org.uk/diffraction/x-ray/powder_method.htm.
[45] H. M. Rietveld, *J. Appl. Crystallogr.* **1969**, *2*, 65.
[46] G. Malmros, J. O. Thomas, *J. Appl. Crystallogr.* **1977**, *10*, 7.
[47] R. A. Young, in *The Rietveld Method* (Ed.: R. A. Young), Oxford University Press, New York, **2002**, pp. 1.
[48] L. C. Larson, R. B. Von Dreele, LANSCE, MSH805, Los Alamos National Laboratory, NM 87545, **1995**.
[49] A. C. Larson, R. B. von Dreele, Los Alamos National Laboratory: Los Alamos, NM, **2000**.
[50] B. H. Toby, *J. Appl. Crystallogr.* **2001**, *34*, 210.
[51] SMART, 4 ed., Simens Analystical X-ray Instruments Inc., Madison, WI, **1995**.
[52] SAINT, 4 ed., Siemens Analytical X-ray Instruments Inc., Madison, WI., **1995**.
[53] W. Clegg, A. J. Blake, R. O. Gould, P. Main, *Crystal Structure Analysis: Principles and Practice*, Oxford University Press Inc., New York, **2001**.
[54] G. M. Sheldrick, *SHELXTL*, Version 5.12 ed., Siemens Analytical X-Ray Systems, Madison, WI., **1995**.

[55] J. Kohanoff, *Electronic Structure Calculations for Solids and Molecules: Theory and Computational Methods*, Cambridge University Press, New York, **2006**.
[56] R. Dronskowski, *Computational Chemistry of Solid State Materials*, WILEY-VCH, Weinheim, **2005**.
[57] R. Hoffmann, *Angew. Chem. Int. Ed. Engl.* **1987**, *26*, 846.
[58] J. K. Burdett, *Chemical Bondings in Solids*, Oxford University Press, Inc., New York, NY., **1995**.
[59] R. S. Mulliken, *J. Chem. Phys.* **1955**, *23*, 2343.
[60] T. Hughbanks, R. Hoffmann, *J. Am. Chem. Soc.* **1983**, *105*, 3528.
[61] R. Dronskowski, P. E. Blöchl, *J. Phys. Chem.* **1993**, *97*, 8617.
[62] G. A. Landrum, R. Dronskowski, *Angew. Chem. Int. Ed.* **2000**, *39*, 1560.
[63] G. S. Nolas, J. Sharp, H. J. Goldsmid, *Thermoelectrics, Basic principles and new materials developments*, Springer, New York, NY, **2001**.
[64] G. D. Mahan, J. O. Sofo, *Proc. Natl. Acad. Sci.* **1996**, *93*, 7436.
[65] O. K. Andersen, *Phys. Rev. B* **1975**, *12*, 3060.
[66] H. L. Skriver, *The LMTO Method*, Springer, Berlin, **1984**.
[67] L. Hedin, B. I. Lundqvist, *J. Phys. C* **1971**, *4*, 2064.
[68] P. E. Blöchl, O. Jepsen, O. K. Andersen, *Phys. Rev. B* **1994**, *49*, 16223.
[69] http://www.mmr.com/seebeck.html.
[70] W. J. Parker, W. J. Jenkins, C. P. Butler, G. L. Abbott, *J. Appl. Phys.* **1961**, *32*, 1679.
[71] D. M. Rowe, *Thermoelectrics Handbook, Macro to Nano*, CRC, Boca Raton, FL, **2006**.
[72] A. Tari, *The Specific Heat of Matter at Low Temperatures*, Imperial College Press, London, **2003**.
[73] J. Blumm, E. Kaisersberger, *J. Therm. Anal. Cal.* **2001**, 385.
[74] A. T. Petit, P. L. Dulong, *Annal. Chim. Phys.* **1819**, *10*, 395.
[75] B. C. Sales, D. Mandrus, R. K. Williams, *Science* **1996**, *272*, 1325.
[76] D.-Y. Chung, T. P. Hogan, M. Rocci-Lane, P. Brazis, J. R. Ireland, C. R. Kannewurf, M. Bastea, C. Uher, M. G. Kanatzidis, *J. Am. Chem. Soc.* **2004**, *126*, 6414.
[77] S. R. Brown, S. M. Kauzlarich, F. Gascoin, G. J. Snyder, *Chem. Mater.* **2006**, *18*, 1873.
[78] K. Sridhar, K. Chattopadhyay, *J. Alloys Compd.* **1998**, *264*, 293.
[79] M. Fujikane, K. Kurosaki, H. Muta, S. Yamanaka, *J. Alloys Compd.* **2005**, *393*, 299.
[80] Y. C. Wang, F. J. DiSalvo, *J. Solid State Chem.* **2001**, *156*, 44.
[81] A. Assoud, S. Thomas, B. Sutherland, H. Zhang, T. M. Tritt, H. Kleinke, *Chem. Mater.* **2006**, *18*, 3866.
[82] R. Patschke, X. Zhang, D. Singh, J. Schindler, C. R. Kannewurf, N. Lowhorn, T. Tritt, G. S. Nolas, M. G. Kanatzidis, *Chem. Mater.* **2001**, *13*, 613.
[83] A. Assoud, N. Soheilnia, H. Kleinke, *Chem. Mater.* **2005**, *17*, 2255.
[84] M. Fujikane, K. Kurosaki, H. Muta, S. Yamanaka, *J. Alloys Compd.* **2005**, *396*, 280.
[85] K. Kurosaki, H. Uneda, H. Muta, S. Yamanaka, *J. Alloys Compd.* **2005**, *395*, 304.
[86] E. Hagiwara, H. Matsushita, A. Katsui, *J. Adv. Science* **2000**, *12*, 40.

[87] H. Matsushita, E. Hagiwara, A. Katsui, *J. Mater. Sci.* **2004**, *39*, 6299.
[88] T. Sakakibara, T. Imoto, Y. Takigawa, K. Kurosawa, *J. Adv. Science* **2001**, *12*, 392.
[89] E. A. Skrabek, D. S. Trimmer, in *CRC Handbook of Thermoelectrics* (Ed.: D. M. Rowe), CRC Press, Boca Raton, FL, **1995**, pp. 267.
[90] L. E. Shelimova, P. P. Konstantinov, O. G. Karpinsky, E. S. Avilov, M. A. Kretova, J. P. Fleurial, *Intern. Conf. Thermoelectr.* **1999**, *18*, 536.
[91] J. Wang, X.-g. Lu, S. Bo, X. Su, *J. Alloys Compd.* **2006**, *407*, 106.
[92] D. P. Young, C. L. Brown, P. Khalifah, R. J. Cava, A. P. Ramirez, *J. Appl. Phys.* **2000**, *88*, 5221.
[93] Y. Park, M. G. Kanatzidis, *Inorg. Chem.* **2001**, *40*, 5913.
[94] Y. Cui, A. Assoud, J. Xu, H. Kleinke, *Inorg. Chem.* **2007**, *46*, 1215
[95] *SAINT*, Version 4 ed., Siemens Analytical X-ray Instruments Inc., Madison, WI., **1995**.
[96] X. Zhang, J. L. Schindler, T. Hogan, J. Albritton-Thomas, C. R. Kannewurf, M. G. Kanatzidis, *Angew. Chem. Int. Ed. Engl.* **1995**, *34*, 68.
[97] K. Volk, G. Cordier, R. Cook, H. Schäfer, *Z. Naturforsch. B* **1980**, *35*, 136.
[98] A. Assoud, S. Derakhshan, N. Soheilnia, H. Kleinke, *Chem. Mater.* **2004**, *16*, 4193.
[99] K. Spangenberg, *Naturwiss.* **1927**, *15*, 266.
[100] F. Pertlik, *Tscherm. Miner. Petrogr. Mitt.* **1984**, *33*, 203.
[101] T. K. Reynolds, M. A. McGuire, F. J. DiSalvo, *J. Solid State Chem.* **2004**, *177*, 2998.
[102] F. Q. Huang, P. Brazis, C. R. Kannewurf, J. A. Ibers, *J. Am. Chem. Soc.* **2000**, *122*, 80.
[103] F. Q. Huang, J. A. Ibers, *J. Solid State Chem.* **2001**, *159*, 186.
[104] K. D. Machado, J. C. de Lima, T. A. Grandi, C. E. M. Campos, C. E. Maurmann, A. A. M. Gasperin, S. M. Souza, A. F. Pimenta, *Acta Crystallogr. B* **2004**, *60*, 282.
[105] S. Strobel, T. Schleid, *J. Solid State Chem.* **2003**, *171*, 424.
[106] E. Makovicky, I. Sotofte, S. Karup-Moller, *Z. Kristallogr.* **2002**, *217*, 597.
[107] G. A. Papoian, R. Hoffmann, *Angew. Chem. Int. Ed.* **2000**, *39*, 2408.
[108] W. R. L. Lambrecht, O. K. Andersen, *Phys. Rev. B* **1986**, *34*, 2439.
[109] M. J. Frisch, G. W. Trucks, H. B. Schlegel, G. E. Scuseria, M. A. Robb, J. R. Cheeseman, V. G. Zakrzewski, J. J. A. Montgomery, R. E. Stratmann, J. C. Burant, S. Dapprich, J. M. Millam, A. D. Daniels, K. N. Kudin, M. C. Strain, O. Farkas, J. Tomasi, V. Barone, M. Cossi, R. Cammi, B. Mennucci, C. Pomelli, C. Adamo, S. Clifford, J. Ochterski, G. A. Petersson, P. Y. Ayala, Q. Cui, K. Morokuma, D. K. Malick, A. D. Rabuck, K. Raghavachari, J. B. Foresman, J. Cioslowski, J. V. Ortiz, A. G. Baboul, B. B. Stefanov, G. Liu, A. Liashenko, P. Piskorz, I. Komaromi, R. Gomperts, R. L. Martin, D. J. Fox, T. Keith, M. A. Al-Laham, C. Y. Peng, A. Nanayakkara, C. Gonzalez, M. Challacombe, P. M. W. Gill, B. Johnson, W. Chen, M. W. Wong, J. L. Andres, C. Gonzalez, M. Head-Gordon, E. S. Replogle, J. A. Pople, Gaussian 98, Revision A.7 ed., Gaussian, Inc., Pittsburgh, PA, USA, **1998**.

[110] W. J. Pietro, M. M. Francl, W. J. Hehre, D. J. DeFrees, J. A. Pople, J. S. Binkley, *J. Am. Chem. Soc.* **1982**, *104*, 5039.
[111] W. V. Glassey, R. Hoffmann, *J. Chem. Phys.* **2000**, *113*, 1698.
[112] C. Kittel, *Introduction to Solid State Physics*, 7th ed., John Wiley & Sons, Inc., New York City, NY, **1996**.
[113] L. M. Castro-Castro, L. Chen, J. D. Corbett, *J. Solid State Chem.* **2007**, *180*, 3172.
[114] M. A. McGuire, F. J. DiSalvo, *Chem. Mater.* **2007**, *19*, 4600.
[115] Y. Wu, W. Bensch, *J. Solid State Chem.* **2009**, *182*, 471.
[116] K. Ohgushi, Y. Okimoto, T. Ogasawara, S. Miyasaka, Y. Tokura, *J. Phys. Soc. Jpn.* **2008**, *77*, 034713/1.
[117] Y. Cui, A. Assoud, J. Xu, H. Kleinke, *Inorg. Chem.* **2007**, *46*, 1215
[118] A. Assoud, Y. Cui, S. Thomas, B. Sutherland, H. Kleinke, *J. Solid State Chem.* **2008**, *181*, 2024.
[119] Y. Cui, A. Assoud, H. Kleinke, *Inorg. Chem.* **2009**, *48*, 5313.
[120] C. L. Teske, *Z. Naturforsch. B* **1979**, *34*, 386.
[121] C. L. Teske, *Z. Naturforsch. B* **1979**, *34*, 544.
[122] M. Tampier, D. Johrendt, *Z. Naturforsch. B* **1998**, *53*, 1483.
[123] M. Tampier, D. Johrendt, *Z. Anorg. Allg. Chem.* **2001**, *627*, 312.
[124] Y. Cui, O. Mayasree, A. Assoud, H. Kleinke, *J. Alloys. Compd.* **2009**, *in press*.
[125] W. C. Hamilton, *Acta Crystallogr.* **1965**, *18*, 502.
[126] A. L. Spek, *J. Appl. Cryst.* **2003**, *36*, 7.
[127] B. Kuropatwa, Y. Cui, A. Assoud, H. Kleinke, *Chem. Mater.* **2009**, *21*, 88.
[128] G. Dittmar, *Z. Anorg. Allg. Chem.* **1979**, *453*, 68.
[129] B. Eisenmann, H. Schwerer, H. Schäfer, *Z. Naturforsch. B* **1981**, *36*, 1538.
[130] A. Assoud, N. Soheilnia, H. Kleinke, *J. Solid State Chem.* **2006**, *179*, 2707.
[131] B. Eisenmann, H. Schwerer, H. Schäfer, *Rev. Chim. Min.* **1983**, *20*, 78.
[132] A. Assoud, Y. Cui, S. Thomas, B. Sutherland, H. Kleinke, *J. Solid State Chem.* **2008**, *181*, 2024.
[133] A. Assoud, J. Xu, H. Kleinke, *Inorg. Chem.* **2007**, *46*, 9906.
[134] P. K. Mehrotra, R. Hoffmann, *Inorg. Chem.* **1978**, *17*, 2187.
[135] K. M. Merz Jr., R. Hoffmann, *Inorg. Chem.* **1988**, *27*, 2120.
[136] P. Pyykkö, *Chem. Rev.* **1997**, *97*, 597.
[137] L. Pauling, *The Nature of the Chemical Bond*, 3rd ed., Cornell University Press, Ithaca, NY, **1948**.
[138] H. J. Goldsmid, J. W. Sharp, *J. Electron. Mater.* **1999**, *28*, 869.
[139] D. M. Rowe, *Handbook of Thermoelectrics*, 1995 ed., CRC, Boca Raton, **1995**.
[140] H. J. Goldsmid, *Electronic Refrigeration*, Pion Limited, London, **1986**.
[141] C. W. Wood, *Rep. Prog. Phys.* **1988** *51*, 459.
[142] T. M. Tritt, M. Kanatzidis, G. Mahan, H. B. Lyon Jr., in *Thermoelectric Materials--New Approaches and Advances, Vol. 478*, Mater. Res. Soc. Proc., **1997**.
[143] A. C. Masset, C. Michel, A. Maignan, M. Hervieu, O. Toulemonde, F. Studer, B. Raveau, *Phys. Rev. B* **2000**, *62*, 166.
[144] I. Terasaki, *Physica B* **2003**, *328*, 63.
[145] J. Androulakis, P. Migiakis, J. Giapintzakis, *Appl. Phys. Lett.* **2004**, 1099.
[146] I. Terasaki, *Physica B* **2006**, *383*, 107.

[147] A. A. Taskin, A. N. Lavrov, Y. Ando, *Phys. Rev. B* **2006**, *73*, 121101.
[148] H. P. R. Frederikse, W. R. Thurber, W. R. Hosler, *Phys. Rev,* **1964**, *134*, A422.
[149] A. V. Shevelkov, *Russ. Chem. Rev.* **2008**, *77*, 1.
[150] Y. Cui, J. R. Salvador, J. Yang, H. Wang, G. Amow, H. Kleinke, *J. Electron. Mater* **2009**, *38*, 1002.
[151] Y. Cui, J. He, G. Amow, H. Kleinke, *Dalton Trans.* **2009**, *in press*.
[152] R. B. von Dreele, J. D. Jorgensen, C. G. Windsor, *J. Appl. Crystallogr.* **1982**, *15*, 581.
[153] J. O. Sofo, G. D. Mahan, *Phys. Rev. B* **1994**, *49*, 4565.
[154] N. F. Mott, H. Jones, *The Theory of the Properties of Metals and Alloys*, Dover Publications, New York, NY, **1958**.
[155] A. M. Rao, X. Ji, T. M. Tritt, *Mat. Res. Bull.* **2006**, *31*, 218.
[156] H. Zhang, J. He, B. Zhang, Z. Su, T. M. Tritt, N. Soheilnia, H. Kleinke, *J. Electron. Mater.* **2007**, *36*, 727.
[157] H. Xu, N. Soheilnia, T. M. Tritt, H. Kleinke, *Mat. Res. Soc. Symp. Proc.* **2008**, *1044*, 459.
[158] H. Muta, K. Kurosaki, S. Yamanaka, *J. Alloys Compd.* **2004**, *368*, 22.
[159] G. Xu, R. Funahashi, Q. Pu, B. Liu, R. Tao, G. Wang, Z. Ding, *Solid State Ionics* **2004**, *171*, 147.
[160] H. Muta, K. Kurosaki, S. Yamanaka, *J. Alloys Compd.* **2005**, *392*, 306.
[161] H. Muta, K. Kurosaki, S. Yamanaka, *Mater. Lett.* **2004**, *58*, 3868.

Appendices

Appendix A

Table A.2.1. Crystallographic data of $Ba_7Au_2Te_{14}$ (left) and $Ba_{6.76}Cu_{2.42}Te_{14}$ (right).

Refined formula	$Ba_7Au_{1.995(9)}Te_{14}$	$Ba_{6.76(1)}Cu_{2.42(7)}Te_{14}$
Formula weight [g/mol]	3141.71	2868.59
T of measurement [K]	298(2)	298(2)
Wavelength [Å]	0.71073	0.71073
Crystal system	Hexagonal	Hexagonal
Space group	$P6_3/mcm$	$P6_3/mcm$
a [Å]	14.2593(7)	14.1332(4)
c [Å]	9.2726(8)	9.2108(6)
V [Å^3]	1632.8(2)	1593.3(1)
Z	2	2
ρ_{calcd} [g/cm^3]	6.390	5.979
μ (mm^{-1})	29.492	22.344
Reflection collected/unique	11843/1314	16080/1307
R_{int}	0.0493	0.0315
$R1$ and $wR2$ (all data)[a]	0.0403, 0.0715	0.0378, 0.0803
$R1$ and $wR2$ ($I > 2\sigma(I)$)[a]	0.0369, 0.0702	0.0369, 0.0799

a) $R1 = \Sigma||F_o|-|F_c|| / \Sigma|F_o|$; $wR2 = [\ \Sigma[w(F_o^2 - F_c^2)^2] / \Sigma[w(F_o^2)^2]\ ]^{1/2}$

Table A.2.2. Atomic coordinates and equivalent displacement parameters of $Ba_7Au_2Te_{14}$ (top) and $Ba_{6.76}Cu_{2.42}Te_{14}$ (bottom).

Atom	site	*x*	*y*	*z*	U_{eq}/Å^2	Occ.
Ba1	12j	0.45267(3)	0.21083(3)	¼	0.01216(10)	1
Ba2	2b	0	0	½	0.0348(3)	1
Te1	6g	0.18356(5)	0	¼	0.02083(17)	1
Te2	12k	0.33229(4)	0.33229(4)	0.02535(6)	0.01525(12)	1
Te3	6g	0.47277(5)	0.47277(5)	¼	0.01393(14)	1
Te4	4d	2/3	1/3	0	0.01241(15)	1
Au1	6g	0.19410(5)	0.19410(5)	¼	0.0241(2)	0.665(3)
Ba1	12j	0.45096(4)	0.20789(4)	¼	0.0146(1)	1
Ba2	2b	0	0	½	0.066(1)	0.76(1)
Te1	6g	0.17585(6)	0	¼	0.0354(3)	1
Te2	12k	0.32582(4)	0.32582(4)	0.02718(6)	0.0216(1)	1
Te3	6g	0.46933(5)	0.46933(5)	¼	0.0175(2)	1
Te4	4d	2/3	1/3	0	0.0143(2)	1
Cu1	6g	0.1952(2)	0.1952(2)	¼	0.0232(7)	0.617(8)
Cu2	12k	0.155(1)	0.155(1)	0.089(2)	0.042(5)	0.095(7)

*U_{eq} is defined as one third of the trace of the orthogonalized U_{ij} tensor.

Table A.2.3. Selected interatomic distances [Å] of $Ba_7Au_2Te_{14}$ (left) and $Ba_{6.76}Cu_{2.42}Te_{14}$ (right).

		$Ba_7Au_2Te_{14}$	$Ba_{6.76}Cu_{2.42}Te_{14}$
Ba1–Te1		3.4967(7)	3.5110(7)
Ba1–Te2	2×	3.6412(5)	3.6147(5)
Ba1–Te2	2×	3.6528(5)	3.6170(5)
Ba1–Te3		3.6004(6)	3.5723(6)
Ba1–Te3		3.6557(7)	3.6348(7)
Ba1–Te4	2×	3.5222(4)	3.5121(3)
Ba2–Te1	6×	3.4964(6)	3.3881(7)
M1–Te1	2×	2.6957(5)	2.6329(15)
M1–Te2	2×	2.8674(7)	2.7602(18)
M2–Te1	2×		2.778(11)
M2–Te1			3.14(2)
M2–Te2			2.483(16)
Te2–Te3	2×	2.8900(7)	2.8855(8)
Te1–Te2	2×	3.319(1)	3.318(1)

Table A.3.1. Crystallographic data of $Ba_4Ag_{3.95}Ge_2Te_9$ (left), $Ba_4Ag_{3.97}Si_2Te_9$ (middle) and $Ba_4Cu_{3.71}Ge_2Te_9$ (right).

Refined formula	$Ba_4Ag_{3.946(4)}Ge_2Te_9$	$Ba_4Ag_{3.968(4)}Si_2Te_9$	$Ba_4Cu_{3.71(2)}Ge_2Te_9$
Formula weight [g/mol]	2268.49	2181.97	2078.93
T of measurement [K]	296(2)	296(2)	296(2)
Wavelength [Å]	0.71073	0.71073	0.71073
Crystal system	Orthorhombic	Orthorhombic	Orthorhombic
Space group	*Pbam*	*Pbam*	*Pbam*
a [Å]	8.6835(3)	8.6389(3)	8.6464(2)
b [Å]	13.6421(4)	13.5883(4)	13.5305(4)
c [Å]	10.2612(3)	10.2252(3)	10.0810(3)
V [Å^3]	1215.55(7)	1200.32(7)	1179.38(6)
Z	2	2	2
ρ_{calcd} [g/cm^3]	6.198	6.037	5.854
μ (mm^{-1})	22.472	20.419	23.239
Reflection collected/unique	16779/1869	13606/1932	10220/1827
R_{int}	0.0331	0.0305	0.0256
*R*1 and *wR*2 (all data)[a]	0.0160, 0.0329	0.0193, 0.0341	0.0236, 0.0475
*R*1 and *wR*2 ($I > 2\sigma(I)$)[a]	0.0154, 0.0327	0.0166, 0.0332	0.0218, 0.0466

a) $R1 = \Sigma||F_o|-|F_c|| / \Sigma|F_o|$; $wR2 = [\ \Sigma[w(F_o^2 - F_c^2)^2] / \Sigma[w(F_o^2)^2]\ ]^{1/2}$

Table A.3.2. Atomic coordinates and equivalent displacement parameters of $Ba_4Ag_{3.95}Ge_2Te_9$ (top), $Ba_4Ag_{3.97}Si_2Te_9$ (middle) and $Ba_4Cu_{3.71}Ge_2Te_9$ (bottom).

Atom	site	*x*	*y*	*z*	$U_{eq}/Å^2$	Occ.
Ba	8i	0.37968(2)	0.32391(1)	0.23993(2)	0.01521(6)	1
Te1	8i	0.25031(2)	0.06300(2)	0.29184(2)	0.01381(6)	1
Te2	4h	0.09896(3)	0.28005(2)	0.5	0.01462(7)	1
Te3	4g	0.08035(3)	0.31419(2)	0	0.01401(7)	1
Te4	2a	0	0	0	0.01510(9)	1
Ag1	4g	0.26150(5)	0.12478(3)	0	0.0275(2)	0.973(2)
Ag2	4f	0	0.5	0.14071(4)	0.0268(1)	1
Ge	4h	0.41797(5)	0.07233(3)	0.5	0.01200(9)	1
Ba	8i	0.38080(2)	0.32528(2)	0.24072(2)	0.01553(6)	1
Te1	8i	0.25449(2)	0.06324(2)	0.29912(2)	0.01360(6)	1
Te2	4h	0.09702(4)	0.28497(2)	0.5	0.01429(7)	1
Te3	4g	0.08043(4)	0.31438(2)	0	0.01404(7)	1
Te4	2a	0	0	0	0.01495(9)	1
Ag1	4g	0.26185(5)	0.12395(4)	0	0.0285(2)	0.984(2)
Ag2	4f	0	0.5	0.14128(4)	0.0261(1)	1
Si	4h	0.4219(2)	0.07006(9)	0.5	0.0110 (2)	1
Ba	8i	0.38575(3)	0.32114(2)	0.24098(3)	0.01849(7)	1
Te1	8i	0.26121(3)	0.06176(2)	0.28142(3)	0.01903(8)	1
Te2	4h	0.10616(4)	0.28046(3)	0.5	0.01569(9)	1
Te3	4g	0.07657(7)	0.32458(5)	0	0.0221(2)	0.870(2)
Te3A	4g	0.1149(5)	0.2800(4)	0	0.0221(2)	0.130
Te4	4g	0.0274(1)	0.0032(2)	0	0.0187(3)	0.5
Cu1	4g	0.2345(3)	0.4825(2)	0	0.0427(9)	0.447(5)
Cu1A	4g	0.2607(9)	0.1423(7)	0	0.057(2)	0.219(3)
Cu1B	4g	0.2874(8)	0.1010(6)	0	0.058(2)	0.247(4)
Cu2	4f	0	0.5	0.1371(1)	0.0424(4)	0.886(4)
Cu2A	2c	0	0.5	0	0.0424(4)	0.114

Ge	4h	0.41879(8)	0.07237(5)	0.5	0.0164(1)	1

*U_{eq} is defined as one third of the trace of the orthogonalized U_{ij} tensor.

Table A.3.3. Selected interatomic distances [Å] of $Ba_4Ag_{3.95}Ge_2Te_9$ (left), $Ba_4Ag_{3.97}Si_2Te_9$ (middle) and $Ba_4Cu_{3.71}Ge_2Te_9$ (right).*

		$Ba_4Ag_{3.95}Ge_2Te_9$	$Ba_4Ag_{3.97}Si_2Te_9$	$Ba_4Cu_{3.71}Ge_2Te_9$
Ba–Te1		3.4923(3)	3.4896(3)	3.6354(4)
Ba–Te1		3.6086(3)	3.6158(3)	3.5186(4)
Ba–Te1		3.7703(3)	3.7717(3)	3.6936(4)
Ba–Te2		3.5720(3)	3.5724(3)	3.6008(4)
Ba–Te2		3.6636(3)	3.6522(3)	3.5129(4)
Ba–Te3/Te3A		3.5563(3)	3.5545(3)	3.6125(5)/3.421(3)
Ba–Te3		3.5826(3)	3.5796(3)	3.5371(4)/3.420(3)
Ba–Te4/Te4		3.5949(2)	3.5715(2)	3.540(2)/3.613(2)
M1–M1A/M1B				{2.16(1)}/{1.615(8)}
M1–M2/M2A	2×	3.0449(4)	3.0260(5)	2.465(3)/{2.041(3)}
M1A–M1B				{0.604(9)}
M1A–M2/M2A				3.146(8)/2.83(1)
M1B–M2/M2A	2×			2.675(7)/{2.291(8)}
M2–M2/M2A		2.8877(8)	2.8891(8)	2.764(2)/{1.382(1)}
M1–Te1	2×	3.1125(3)	3.1686(3)	3.033(1)
M1–Te3/Te3A		2.8913(5)	2.8770(5)	2.536(3)/2.928(5)
M1–Te3/Te3A		3.0251(5)	3.0252(6)	4.231(6)/4.909(3)
M1–Te4/Te4		2.8379(4)	2.8203(4)	2.540(3)/{2.078(3)}
M1A–Te1	2×			3.039(4)
M1A–Te3/Te3A				2.94(1)/{2.25(1)}
M1A–Te3/Te3A				2.768(8)/3.238(9)
M1A–Te4/Te4				2.759(8)/3.175(9)

M1B–Te1	2×			2.895(2)
M1B–Te3/Te3A				2.695(7)/3.258(9)
M1B–Te3/Te3A				3.532(8)/2.844(9)
M1B–Te4/Te4				2.609(7)/3.07(7)
M2–Te1	2×	2.8008(3)	2.8003(3)	2.6606(7)
M2–Te3/Te3A	2×	2.9995(3)	2.9885(3)	2.8251(9)/3.429(5)
M2A–Te3/Te3A	2×			{2.4641(7)}/3.1385)
M2A–Te1	4×			3.607(4)
Ge–Ge		2.4341(9)	2.334(3)	2.410(1)
Ge–Te1	2×	2.5880(3)	2.5136(8)	2.5947(5)
Ge–Te2		2.5545(5)	2.484(1)	2.5670(7)

*: Unreasonable distances are in curly brackets. Two distances in one cell of Table 3.3, separated by the slash, indicate that only one of the two will be present at a given site in the crystal.

Table A.3.4. Crystallographic data of $Ba_4Cu_{3.75}Si_2Te_9$ (left) and $Ba_4Au_{3.69}Ge_2Te_9$ (right).

Refined formula	$Ba_4Cu_{3.75(2)}Si_2Te_9$	$Ba_4Au_{3.69(1)}Ge_2Te_9$
Formula weight [g/mol]	1992.21	2569.75
T of measurement [K]	296(2)	296(2)
Wavelength [Å]	0.71073	0.71073
Crystal system	Orthorhombic	Orthorhombic
Space group	*Pnma*	*Pnma*
a [Å]	13.4293(4)	13.5806(6)
b [Å]	20.0980(7)	20.7033(9)
c [Å]	8.5699(3)	8.6418(4)
V [$Å^3$]	2313.0(1)	2429.8(2)
Z	2	4
ρ_{calcd} [g/cm^3]	5.721	7.025
μ (mm^{-1})	21.285	41.565
Reflection collected/unique	16881/3454	17912/3632
R_{int}	2.69	0.0459
*R*1 and *wR*2 (all data)[a]	0.0343, 0.0609	0.0379, 0.0702
*R*1 and *wR*2 ($I > 2\sigma(I)$)[a]	0.0294, 0.0583	0.0294, 0.0673

a) $R1 = \Sigma||F_o|-|F_c|| / \Sigma|F_o|$; $wR2 = [\ \Sigma[w(F_o^2 - F_c^2)^2] / \Sigma[w(F_o^2)^2]\ ]^{1/2}$

Table A.3.5. Atomic coordinates and equivalent displacement parameters of $Ba_4Cu_{3.75}Si_2Te_9$ (top) and $Ba_4Au_{3.69}Ge_2Te_9$ (bottom).

Atom	site	*x*	*y*	*z*	U_{eq}/Å^2	Occ.
Ba1	8d	0.32175(3)	0.63044(2)	0.38473(4)	0.01560(9)	1
Ba2	8d	0.32237(3)	0.12859(2)	0.38470(4)	0.01495(8)	1
Te1	8d	0.06283(3)	0.60873(2)	0.26851(5)	0.01419(9)	1
Te2	8d	0.28448(3)	0.00000(2)	0.10306(4)	0.01360(9)	1
Te3	4c	0.31798(4)	0.25	0.08551(7)	0.0168(1)	1
Te4	4c	0.00067(4)	0.25	0.01735(7)	0.0159(1)	1
Te5	8d	0.06081(3)	0.10216(2)	0.25894(4)	0.01359(9)	1
Te6	4c	0.16996(4)	0.25	0.55998(7)	0.0163(1)	1
Cu1	4c	0.0106(1)	0.25	0.7253(2)	0.0331(5)	0.903(6)
Cu2	8d	0.49009(8)	0.18174(5)	0.0236(1)	0.0291(3)	0.968(4)
Cu3	4c	0.12663	0.25	0.2562(2)	0.0581(8)	0.912(7)
Si	4h	0.0703(1)	0.50174(8)	0.4224(2)	0.0123(3)	1
Ba1	8d	0.31977(4)	0.62906(2)	0.38012(6)	0.0208(1)	1
Ba2	8d	0.31953(3)	0.12708(2)	0.37244(6)	0.0200(1)	1
Te1	8d	0.06345(4)	0.60969(3)	0.26069(6)	0.0193(1)	1
Te2	8d	0.27942(4)	-0.00097(2)	0.09865(6)	0.0180(1)	1
Te3	4c	0.30463(6)	0.25	0.08517(9)	0.0224(2)	1
Te4	4c	-0.00780(6)	0.25	0.03305(9)	0.0235(2)	1
Te5	8d	0.06108(4)	0.10067(3)	0.25008(6)	0.0190(1)	1
Te6	4c	0.20296(6)	0.25	0.57681(9)	0.0237(2)	1
Au1	4c	0.03572(4)	0.25	0.73980(6)	0.0250(2)	0.863(2)
Au1A	4c	0.8835(9)	0.25	0.706(1)	0.0250(5)	0.038(1)
Au2	8d	0.48320(7)	0.17774(2)	0.02817(6)	0.0315 (2)	0.886(2)
Au2A	8d	0.5227(6)	0.1756(3)	0.9978(8)	0.0315(9)	0.085(2)
Au3	4c	0.12533(4)	0.25	0.28080(7)	0.0308(2)	0.887(3)
Ge	4h	0.07143(6)	0.50274(4)	0.4161(1)	0.0169(2)	1

*U_{eq} is defined as one third of the trace of the orthogonalized U_{ij} tensor.

Table A.3.6. Selected interatomic distances [Å] of $Ba_4Cu_{3.75}Si_2Te_9$ (left) and $Ba_4Au_{3.69}Ge_2Te_9$ (right).*

		$Ba_4Cu_{3.75(2)}Si_2Te_9$	$Ba_4Au_{3.69(1)}Ge_2Te_9$
Ba1–Te1		3.5209(5)	3.5487(7)
Ba1–Te1		3.6431(5)	3.6530(7)
Ba1–Te5		3.6187(5)	3.6311(7)
Ba1–Te2		3.5226(5)	3.5535(7)
Ba1–Te2		3.5986(5)	3.6400(7)
Ba1–Te3		3.5008(6)	3.5020(7)
Ba1–Te6		3.6786(6)	3.6381(8)
Ba1–Te4		3.5712(6)	3.8127(8)
Ba2–Te1		3.6544(5)	3.7300(7)
Ba2–Te5		3.4715(5)	3.4902(7)
Ba2–Te5		3.7124(5)	3.7063(7)
Ba2–Te2		3.4985(5)	3.5276(7)
Ba2–Te2		3.5727(5)	3.5947(7)
Ba2–Te3		3.5400(6)	3.5610(8)
Ba2–Te6		3.5213(5)	3.4788(7)
Ba2–Te4		3.5202(6)	3.5557(7)
M1–M1A			{2.09(1)}
M1–M2/M2A	2×	2.551(2)	2.8477(7)/{2.573(6)}
M1A–M2/M2A	2×		2.86(1)/3.01(1)
M2–M2/M2A		2.744(2)	2.992(1)/3.094(6)
M2–M3		2.967(2)	2.9477(8)
M2A–M2A			3.08(1)
M2A–M3			2.824(6)
M1/M1A–Te1	2×	3.0061(7)	3.2019(6) /3.007(3)
M1/M1A–Te3		3.713(2)	4.211(1) /2.74(1)
M1/M1A–Te6		2.567(2)	2.6725(9)/ 3.09(1)

M1/M1A–Te4		2.506(2)	2.602(1)/ 3.19(1)
M3–Te5	2×	3.1001(8)	3.2233(6)
M3–Te6		2.668(2)	2.767(1)
M3–Te3		2.957(3)	2.964(1)
M3–Te4		2.655(2)	2.802(1)
M2/M2A–Te1		2.727(1)	2.7802(7)/ 2.726(6)
M2/M2A–Te5		2.633(1)	2.7087(7)/ 2.725(6)
M2/M2A–Te3		2.740(1)	2.892(1)/ 3.422(8)
M2/M2A–Te6		2.869(1)	3.460(1)/ 2.963(8)
Si–Si		2.310(3)	2.425(2)
Si–Te1		2.525(2)	2.592(1)
Si–Te5		2.518(2)	2.581(1)
Si–Te2		2.490(2)	2.569(1)

*: Unreasonable distances are in curly brackets. Two distances in one cell of Table 3.6, separated by the slash, indicate that only one of the two will be present at a given site in the crystal.

Appendix B

Figure B.2.1. Electrical conductivity measurement (lnσ vs. 1/T diagram) of $Ba_7Au_2Te_{14}$ (top two) and $Ba_{6.76}Cu_{2.42}Te_{14}$ (bottom).

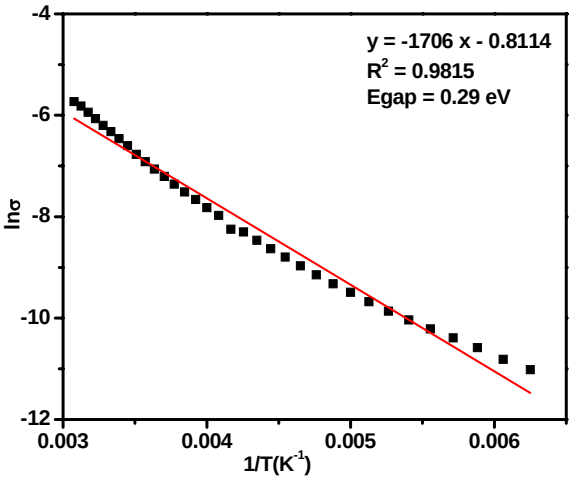

160-325K

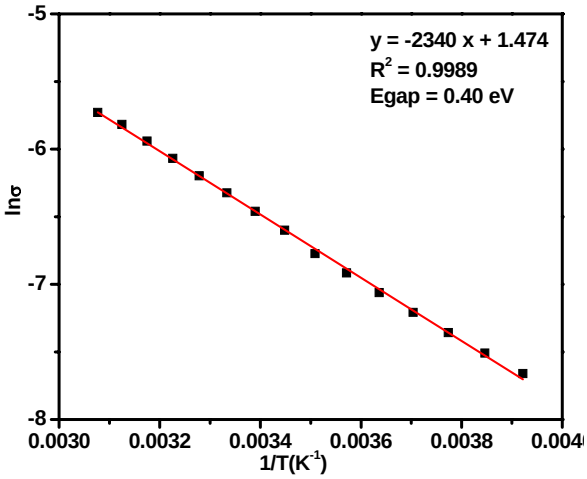

255-325K

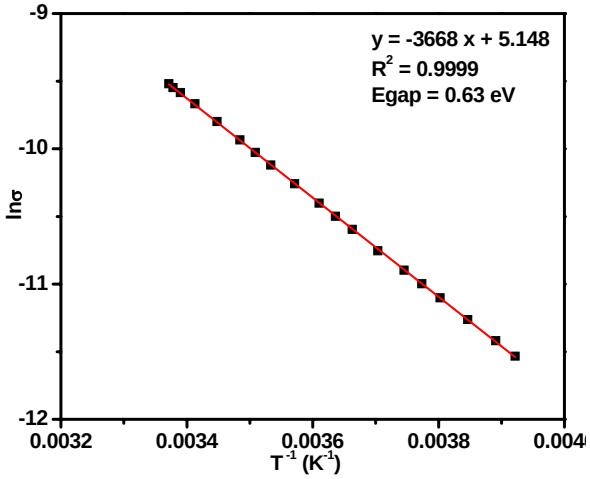

255-300K